2011

Control of Turbulent Flow Over an Articulating Turret for Reduction of Adverse Aero-Optic Effects

Ryan Wallace
Syracuse University

Abstract

Turbulent flows such as wakes and shear layers are highly detrimental to the intensity of any collimated light beams that pass through these regions. The work presented in this thesis utilized suction flow control to help mitigate the adverse affects of the wake and shear layer over a flat aperture on the hemisphere of a three dimensional turret. The hemisphere of the turret was capable of dynamically articulating in two degrees of freedom: pitch and azimuthal rotation. The experiments were performed in the Syracuse University wind tunnel at a Mach number of 0.1, giving a Reynolds number of 500,000. Steady suction at various amounts were initially implemented for both static and dynamic pitching cases. Abatement of the wake above the aperture of the turret was seen for open loop suction actuation in both cases, demonstrating that for our conditions the suction system has enough control authority to reduce the turbulence levels. Building upon this success, a simple proportional closed loop controller was constructed to improve the efficiency of the actuation system by reducing the amount of suction required to achieve the same level of turbulence abatement as with the open loop control. The overall objective of the controller was to drive the velocity fluctuations over the aperture of the turret to zero. The next set of experiments fixed the pitch angle and dynamically rotated the hemisphere in the azimuthal direction. Like the pitch tests, steady suction actuation applied over the top of the turret was able to diminish the size of the wake. A multiple-input-multiple output closed loop controller was then employed with the objective of reducing the velocity fluctuations over the aperture of the turret. By dividing the actuation into two separate zones, the MIMO controller was able to more efficiently decrease the turbulent levels over the aperture when compared to the open loop case. Additional suction control tests were performed over a stationary turret in the Air Force Research Laboratory wind tunnel at Wright-Patterson Air Force Base. Direct measurements of the aero-optic effects were taken via a Malley probe at a fixed pitch angle with and without suction control at a Mach number 0.3, and a corresponding Reynolds number of 2,000,000. Reduction of the aero-optic effects in this test demonstrated that suction control is a practical control input to reduce the near field wavefront abberations due to the turbulent flow over the aperture.

Control of turbulent flow over an articulating turret for reduction of adverse aero-optic effects

By
Ryan Wallace
B.S. University of California, Irvine, 2005
M.S. Syracuse University, 2007

SUBMITTED IN PARTIAL FULFILLMENT OF THE
REQUIREMENTS FOR THE DEGREE OF
DOCTOR OF PHILOSOPHY
AT
SYRACUSE UNIVERSITY
SYRACUSE, NEW YORK, U.S.A.

February 2011

SYRACUSE UNIVERSITY

Date: **February 2011**

Author: **Ryan D Wallace**

Title: **Control of turbulent flow over an articulating turret for reduction of adverse aero-optic effects**

Department: **Mechanical and Aerospace Engineering**

Degree: **Ph.D.** Convocation: **May** Year: **2011**

Contents

List of Figures

List of Tables

Nomenclature

Cartesian coordinates

x, y, z	=	chordwise, wall-normal and spanwise coordinates

Roman symbols

a	=	acceleration
a_n	=	time dependent POD expansion coefficient
A_{ni}	=	linear stochastic measurement expansion coefficient
A_p	=	area of the aperture
A_{slots}	=	cross-sectional area of the slots
A_{ref}	=	cross-sectional area of the wind tunnel test section
AR	=	aspect ratio
B	=	body forces
$C_(t, t')$	=	snapshot POD correlation tensor
C_μ	=	coefficient of momentum
C_{vol}	=	coefficient of volume
D	=	diameter of the turret
$\mathcal{D}$	=	spatial domain
DC	=	duty cycle
e	=	mean square error of the estimation
f_{sample}	=	sample rate
F	=	force
H	=	height of the turret
K	=	control gains
$\mathcal{L}$	=	Hilbert space
m	=	mass
M	=	Mach number
M_C	=	convective Mach number
N	=	number of modes utilized
N_{PIV}	=	number of PIV snapshots
n	=	mode number
n'	=	fluctuating index of reflection
p	=	fluctuating pressure
P	=	mean pressure
$\tilde{p}$	=	instantaneous pressure
Δp	=	pressure drop

q	=	flow rate
$R(t,t')$	=	classical POD correlation tensor
Re	=	Reynolds number
SG	=	specific gravity
t	=	time
T	=	total number of PIV snapshots used
$\mathcal{T}$	=	period of actuation signal
$\dot{u}$	=	control input
u_i	=	i^{th} component of the velocity
u	=	fluctuating velocity
U_C	=	convective velocity
u_{slot}	=	suction slot exit velocity
$\tilde{u}$	=	instantaneous velocity
U	=	mean velocity
U_∞	=	freestream velocity
W	=	refraction wavefront

Greek symbols

α	=	elevation angle
β	=	azimuthal angle
δ	=	boundary layer height
Δ	=	Malley probe lasers distance
ϵ	=	error
ε	=	optical displacement
γ	=	specific heat ratio
$\lambda^{(n)}$	=	POD eigenvalues of the n^{th} mode
$\phi^{(n)}$	=	POD eigenvector of the n^{th} mode
μ	=	dynamic viscosity
ν	=	kinematic viscosity
ρ'	=	fluctuating density
$\overline{\rho}$	=	mean density
θ	=	angle of the wave aberrations
τ	=	time scale

Mathematical operators

$(\ ,\ )$	=	inner product
$\vec{\ }$	=	vector
$\tilde{\ }$	=	instantaneous
$'$	=	fluctuation
$\bar{\ }$	=	averaged
$\hat{\ }$	=	fourier transform operator
$*$	=	complex conjugate
$\langle\ \rangle$	=	averaged over time, phase, or space
∞	=	freestream

Acronyms

$2-D$	=	two dimensional
$3-D$	=	three dimensional
$MIMO$	=	multiple input multiple output
OPL	=	optical path length
OPD	=	optical path difference
PIV	=	particle image velocimetry
PSD	=	position sensing device
SU	=	Syacuse Univeristy
$SARL$	=	Subsonic Aerodynamic Research Laboratory
$SISO$	=	single-input-single-output
rms	=	root mean square

Acknowledgements

I deeply appreciate all those who help me to get this point.

I would first like to thank my advisor Mark Glauser for all his guidance and support. Thank you for taking me to conferences and workshops and introducing me to other brilliant engineers in fluid community. I have learned so much. I also appreciate the tremendous help with witting this thesis. His critiques made the world of difference to help me become a better scientific writer.

I also would like to thank Hal Carlson and Vaithi for their help and as well as guidance during the project. Their insights and suggestions were key to the success of this project. I thank Ryan Schmit for all his help and the chance to run experiments at Wright-Patterson Air Force Base.

I appreciate the Syracuse University staff who aided me in the design and construction of the SU model. Without the help of John Banas, Dick Chave, and the guys in the physics machine shop, the model might have never worked as well as it did. I would also like to thank Patrick for the help throughout the project. I also appreciate the undergrads who work with me during the summer. The technicians at SARL were great and I would like to thank them for running the wind tunnel, helping troubleshoot, and making my experience at Wright-Patterson fun.

I would like to thank every member of my defense committee (in no particular order): Dr. Varshney, Dr. Lewalle, Dr. Dannenhoffer, Dr. Fardad, and Dr. Murthy. I deeply appreciate the time that you are taking out of your schedules to judge my scientific abilities.

Lastly, I would like to thank my family and friends. Without their support I would have not made it through this long process.

Thank you everyone.

Introduction

Motivation

The effectiveness of airborne laser based high energy weapon systems and communication devices are highly dependent upon the flow state of the medium through which it propagates. Airborne optical systems historically have been typically incased in a hemispheric turret with a cylindrical base protruding from the aircraft as noted by Gordeyev and Jumper [32]. The geometry of a three dimensional turret can be seen in Figure 1. Figure 1 shows both turret models used in the experiments presented in this thesis. The flat portion of the turret corresponds to the airborne optical system's aperture location.

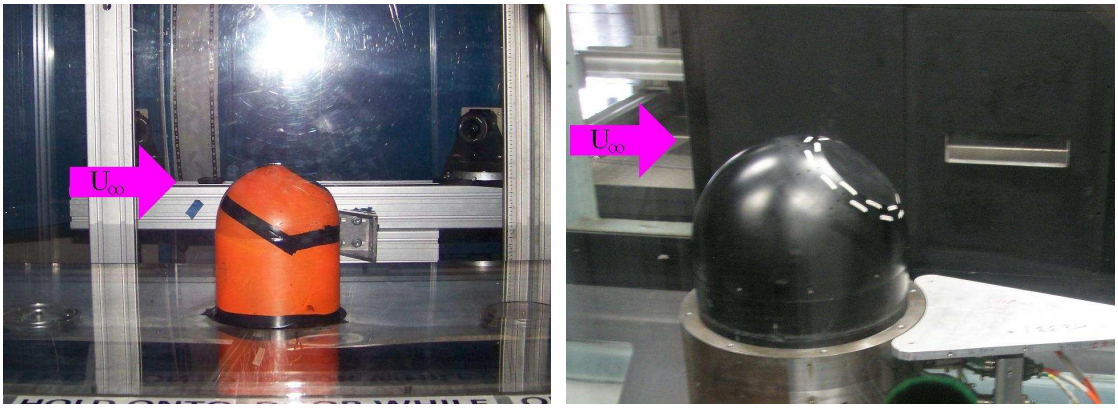

(a) Syracuse University Turret (b) Air Force Turret

Figure 1: Two examples of the laser housing.

In the 1970s and 1980s the first high powered laser systems mounted on aircraft had wavelengths on the order of 10 μm and were noted by Gilbert and Otten [26] to experience losses in the intensity of the light due to turret jitter, near-field aberrations, far-field aberrations, and shock effects. Gilbert and Otten [26] also defined the flow aberration, induced light intensity losses as "aero-optic effects". Advances in laser technology has allowed for more powerful laser systems, which have a lower operating wavelength, to be placed upon aircraft. In recent years Jumper [39] observed that modern lasers operating at lower wavelengths have been found to be much more sensitive to wavefront aberrations within the medium flow, leading to a more significant lost in light intensity. This project focuses on the reduction of the near field, wavefront aberrations above the optical lens of the laser system by suction flow control for a backward facing, articulating turret flying through air at subsonic speeds.

Aerodynamics over a Turret

A brief look at the aerodynamics around a non-articulating turret can help illuminate where the near-field, wave aberrations exist in the flow. A general representation of the flow around a three dimensional turret is seen in Figure 2.

The turret can be classified as a bluff body and the flow characteristic over the aperture is similar to a three dimensional backwards facing ramp. It has been seen both in computational studies by Morgan and Visbal [51] and surface visualization studies by Reid et al. [62] that a well-defined necklace or "horseshoe" vortex forms around the base of the turret. The amount of influence that the horseshoe vortex has upon the flow over the aperture is dependent upon the aspect ratio, ($AR = H/D$), where H is the height and D is the diameter of the turret. A horseshoe vortex around a small aspect ratio turret has greater amount of interaction with the flow

over aperture than turrets with larger aspect ratios according to Recktenwald et al. [61].

The flow around the turret is highly dependent on the Reynolds number of the freestream flow. The Reynolds number represents the ratio of dynamic forces to viscous forces and is defined in Equation 1,

$$Re = \frac{\rho u D}{\mu} \tag{1}$$

where u is the velocity, D is the characteristic length, ρ is the fluid density, and μ is the dynamic viscosity. For cylindrical and spherical bodies at low Reynolds numbers, the incoming flow is laminar and separation occurs near the midpoint of the body, as shown in Munson et al. [52]. On the other hand, when the Reynolds number is increased until the incoming flow becomes turbulent, the separation point moves aft of the midpoint. Separation at the side of the cylindrical portion of the turret was shown by Slunder et al. [67] to generally occur past the midpoint of the turret in a turbulent flow. Work done by Cress et al. [19] also showed that the location angle on the side of the turret where the flow separates is dependent upon the Reynolds number (Re) of the flow and height (H) of the turret. Over the top of the turret Trolinger [76] observed that the Reynolds number also has similar effects upon the location of the separation; when the flow transitions from laminar to turbulent the separation point is moved further aft of the midpoint of the turret. A laminar boundary layer can also be transitioned to turbulence over the top of the turret by tripping the boundary layer with roughness such as a wire as seen by Vukasinovic and Glezer [81]. The delay in the separation location ultimately reduces the size of the turret wake.

The separation point over the top of the turret is also affected by the elevation angle, α and azimuthal angle, β. The separation location's dependence of the aper-

ture's elevation angle was observed in an experimental study of a 2-D turret with a flat aperture by Gordeyev et al. [31]. The experiment showed that increasing the pitch angle generated an adverse pressure gradient, which moved the separation point forward.

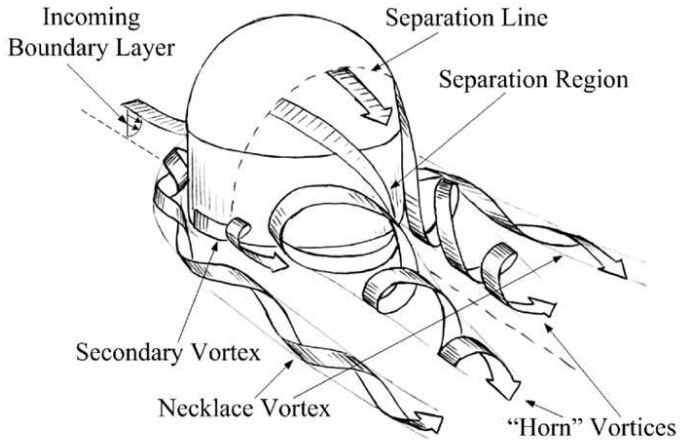

Figure 2: Flow around a turret. From [32]

The near-field wave aberrations above the aperture are generated within the highly turbulent regions of the shear layer and wake of the turret. Turbulent flow is defined in Munson et al. [52] as random, three dimensional vorticity. A general description of the wake and shear layer characteristics can be found in the references by Panton [56], Munson et al. [52], and Anderson [3]. A wake is defined as a highly turbulent region containing reversed flow as well as high velocity and pressure fluctuations. Contained also within the wake are flow structures of multiple length and time scales with corresponding convective velocities that are lower than the freestream velocity. The region of interaction between the wake and the freestream flow is called the shear layer. The shear layer characteristically has large scale structures and also contains high velocity and pressure fluctuations that convect at a lower velocity than the freestream. In a compressible flow case, the wake and shear layer also contain

high density fluctuations.

It has been observed by Smits and Dussauge [68] that there exists a high correlation between velocity and density fluctuations within a highly turbulent flow approximately equal to 0.8. Expanding on the relationship between velocity and density fluctuations, the Strong Reynolds Analogy can be rewritten for adiabatic turbulent flows as Equation 2,

$$\frac{\sqrt{\overline{\rho^2}}}{\overline{\rho}} = (\gamma - 1)M^2 \frac{\sqrt{\overline{u^2}}}{U} \tag{2}$$

where γ is the specific heat ratio for the fluid, $\overline{\rho}$ is mean density, and U is the mean velocity, ρ is the fluctuating density, and u is the fluctuating velocity. This relation shows the strong link between the fluctuating density and the fluctuating velocity. From the density\velocity relationship, a strategy for controlling the velocity fluctuations will be applicable for controlling the density fluctuations.

A unique aspect of the experimental test model shown in this thesis is that the hemispherical portion can rotate dynamically in two degrees of freedom: pitch and yaw directions. Although no previous work has been found to characterize a dynamically articulating turret, there has been extensive work done on oscillating airfoils. A flow characteristic of an airfoil oscillating at a high rate is dynamic stall as described by Carr et al. [15]. Dynamic stall is a phenomenon in which the static stall characteristic of the flow over the airfoil is altered. As an airfoil pitches up, the flow will remain attached beyond the static stall angle of attack. When stall does occur, the flow over the airfoil massively separates at the leading edge of the airfoil. At this point the airfoil experiences a large drop in lift and significant increase in drag. As the airfoil pitches down, the flow eventually reattaches to the airfoil. Ericsson and Reding [21] showed a lag in the aerodynamic forces is generated for a continuously oscillating airfoil as compared to a static airfoil at similar angles of attack. Further

studies performed by Ericsson and Reding [22] of an oscillating airfoil showed a lag in the surface pressure of the airfoil as well. Due to the dynamic pitching, an airfoil experiences a strong hysteresis which alters the angle of attack at which the flow stalls and recovers over the airfoil when compared to the static cases. Similar characteristics of dynamic stall were exhibited for dynamically pitching turrets exhibit within this work and will be further described in Section 3.3.

Aero-Optics

Relations between light and the flow state of a medium have been developed in an attempt to predict the path of a light beam through the medium. In the late 1800's, Gladstone [27] established that the index of refraction fluctuations (n') within the flow medium are directly proportional to the density fluctuations (ρ), as seen in Equation 3,

$$n' = K_{GD}\rho \tag{3}$$

where K_{GD} is the Gladstone constant.

Thus, the amount of density fluctuations within a flow medium can alter the path of the light by refraction. According to Welford [87] the optical path length (OPL), defined in Equation 4, is the integrated index of refraction (n) along the path of the light beam.

$$OPL(x, y, t) = \int_{z_1}^{z_2} n(x, y, z, t)dz \tag{4}$$

This relationship establishes a direct link between the flow state of the medium to the optical path length (OPL) of a collimated light beam. The relative change in the OPL over the area of the aperture is defined as the optical path difference (OPD) in

Equation 5,

$$OPD(x, y, t) = OPL(x, y, t) - \overline{OPL(t)} \tag{5}$$

where the $\overline{OPL(t)}$ is the mean OPL. The OPD is a direct measurement of the aero-optic effects on the collimated light beam propagating through the fluid medium. Figure 3 gives a visual representation of the OPL as it travel through a turbulent region.

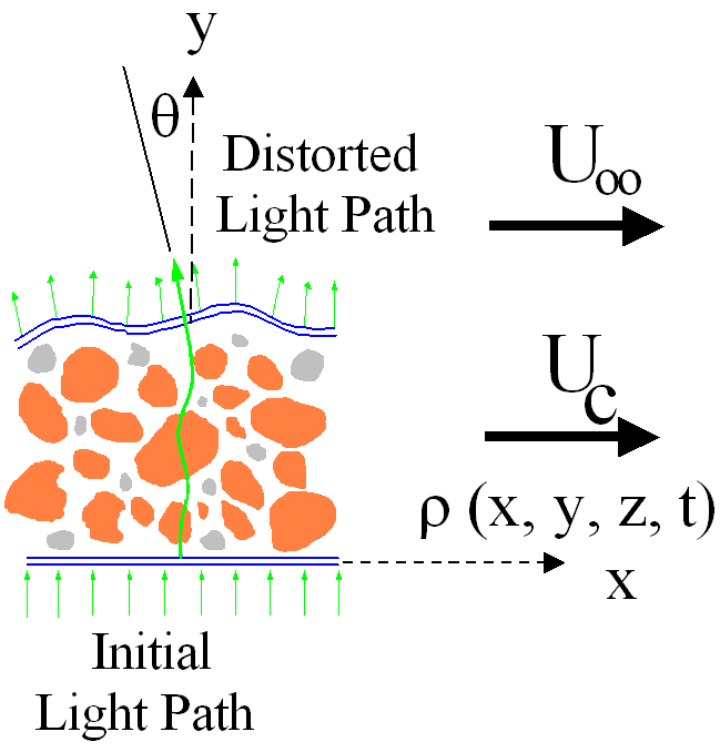

Figure 3: Optical path length through a turbulent region

To date, significant work has been done to determine the effects that wakes and shear layers have upon the optical path length of an emerging collimated light beam. Of particular interest is the aero-optic problem caused by near field wave aberrations within the turbulent wake and shear layer regions of both two and three-dimensional

turrets. Examination of this problem has lead to various aero-optic and turbulent flow relationships being established. Within the shear layer and wake, the large structures have been shown by Fitzgerald and Jumper [23] to be the main generator of light distortion in the flow. These abberations were shown by Gordeyev et al. [34] exists in frequencies above $1,000Hz$. Studies of separated flows over the aperture of a turret by Jumper and Fitzgerald [40] found that the root mean squared (rms) of the OPD (OPD_{rms}), is proportional to square of the convective Mach number, M_C, and the angle of the wave aberrations, θ. Observed by Rose [63], for elevations angles in which the flow is still attached to the wall, the OPD_{rms} is dependent on the height of the boundary layer at that location, δ. The OPD_{rms} was found by Cress et al. [19] to be highly dependent on the convection velocity and thickness of the wake and shear layer. As well as delaying separation, Rose [63] also showed that an incoming turbulent boundary layer promotes small scale structures which have been shown to have less of an effect upon the wave aberrations. High Reynolds number or non-viscous flows do not promote as many aberrations as lower Reynolds number flows. Altering the elevation angles, α, of the aperture of a two dimensional turret has been shown by Gordeyerv et al. [31] to affect the OPD_{rms} by effectively varying the distance that the light must travel through the turbulent region. Gordeyev et al. [32] summarized the OPD_{rms} as a function of: the convective velocity (U_C), freestream velocity (U_∞), incoming boundary layer thickness (δ/H), angle of the wave aberrations (θ), aspect ratio of the turret (AR), area of the aperture (A_p), the elevation angle of aperture relative to the flow (α), and the azimuthal angle of the aperture (β).

OPD Measurement Devices

Multiple optical sensing devices have been developed to measure the OPD of an aberrated wavefront.

A Shack-Hartmann sensor captures the OPD of an emerging aberrated wavefront. The Shack-Hartmann sensor is described by Malacara [46] as an optical based sensor that consists of lenslets and a CCD light detector which measures the 'tilt' of the light due to the wavefront aberrations over the sensor area. The maximum sample rate for a Shack-Hartmann sensor is $2.5kHz$. Although this sensor is spatially resolved, the sample rates are insufficient to obtain a time resolved measurement of the wavefront aberrations. In an attempt to increase the sample rate of the Shack-Hartmann sensor, Neal et al. [53] developed a one dimensional sensor using the same principles as the Shack-Hartmann sensor. This device sacrifices spatial resolution to reach a maximum sample rate of $10kHz$.

Making the assumption that the aberration wavefront convects with the structures within a turbulent region, Malley et al. [45] developed an optical measuring device termed a Malley probe. The Malley probe obtains a more direct measurement of the OPD than the Shack-Hartmann by directly measuring the optical phase variance, according to Klein et al. [42]. At a single point, the Malley probe can sample the wavefront aberrations at $200kHz$. To improve the spatial resolution of the Malley probe, Jumper and Hugo [41] developed the small-aperture beam technique (SABT) sensor. The SABT sensor uses an array of collimated laser beams and position devices to measure the optical phase variance at multiple points.

Within this study, experiments performed at a compressible freestream velocity of Mach 0.3 in the Subsonic Aerodynamic Research Laboratory wind tunnel collected OPD data at the center of the turret's aperture with a Malley probe. The operation

of the Malley probe is explained in Section 2.5.4, while the results of the OPD_{rms} measurements are described in Chapter 5.

Flow Control

Since the early 1990s, several studies have explored the reduction of aero-optic effects over 2-D and 3-D turrets using both passive and active control systems.

A promising method to improve the propagation of the laser light through the turbulent medium is to adapt the laser optics to the incoming flow. Tyson [78] successfully implemented this method for far-field aberrations such as atmospheric turbulence. Nightingale et al. [54] applied the adaptive optic approach to the near-field aberrations. A phase-lock, closed-loop control system was implemented to reshape a morphing lens in a real-time system to match the flow conditions. Although slight improvement of the laser intensity was recorded, this technique shows much promise, especially if combined with flow control.

An alternate method of reducing the refraction of laser light is to mitigate the density fluctuation within the flow over the aperture by either passive or active flow control. A passive flow control test conducted by Gordeyev et al. [31] utilized vortex generators upstream of a two-dimensional turret and found a reduction in the OPD_{rms} due to the reduction of the large scale structures up to an angle of attack of 110°. Passive flow control studies by Woszidlo et al. [88] mounted vortex generators upstream of a three dimension hump. They demonstrated that altering the incoming boundary layer can alter the wake of the hump. Within this study, asymmetric passive flow control was also explored using the vortex generators ahead of the hump. The asymmetric incoming flow resulted in asymmetric flow over the hump.

Active flow control studies by Vukasinovic and Glezer [81] examined open loop

pulsing of synthetic jet actuators at the center of a three-dimensional turret. They were able to delay separation of the flow over the top of a three dimensional turret. This work demonstrated the dependence of the separation delay effectiveness on the amount of control input, defined as the coefficient of momentum (C_μ). Additional open loop flow control studies done by Vukasinovic et al. [82] utilized distributed synthetic jets in front of a flat aperture. They observed an additional improvement in separation delay compared to the center place synthetic jet actuators. In a parallel test, Gordeyev et al. [33] measured the OPD at the aperture of the turret and found an approximate decrease of 22% in the OPD_{rms}. In a low Reynolds number test using synthetic jet actuators as the control input for a three-dimensional turret, Andino et al. [4] showed an effective decrease in the u_{rms} by 15%.

In a follow on active flow control experiment to Andino et al. [4], Andino et al. [5] employed synthetic jet actuators over a three-dimensional turret at Mach 0.3 and a high Reynolds number flow. They explored open-loop controllers and various low dimensional based, proportional closed-loop controllers to alter the flow over the aperture of the turret. By feeding back the pressure based time dependent proper orthogonal decomposition coefficients, Andino et al. [5] obtained a reduction in the surface pressure rms and a homogenization of the flow structures within the wake over the turret.

A steady suction experiment over an airfoil at high angles of attack was shown by Schlichting and Pechau [64] to increase the lift. This work demonstrated that optimally placed suction velocities of one percent of the freestream velocity can reduce the separated flow over the airfoil. Suction has been found to reduce separation in experimental studies by Gregory [25] and numerical studies by Arwatz et al. [7] and Messing and Kloker [49] by bleeding air from incoming boundary layer. These studies showed that suction affects the flow near the surface of the body.

In an early flow control study over a three dimensional turret, Craig [18] showed that suction control around the base delayed separation and reduced the size of the wake. The effect of uniform suction over a three dimensional turret has also been demonstrated to significantly alter the wake area and reduce drag in an early numerical study done by Purohit et al. [59]. A numerical study done by Visbal and Morgan [50] further demonstrated the advantages of employing various active flow control systems over a three-dimensional turret. This work found that steady suction is an effective control input to help delay separation and reduced the size of the wake over the top of the turret.

Thesis Outline

Chapter 1 first reviews the Navier-Stokes Equations and the Continuity Equation. This chapter also presents the Proper Orthogonal Decomposition and Linear Stochastic Measurement techniques that describe the flow in low dimensional terms and estimations, respectively. These techniques have been employed to build Reduced Order Models and implemented in closed loop flow control systems.

Both Syracuse University (SU) and Wright-Patterson Air Force Base (WPAFB) test facilities are described in Chapter 2. The SU and Air Force turret test models, measurement equipment, and operational principals of the equipment are also explained in Chapter 2.

Results from both static and dynamic pitching of the turret's hemisphere are presented in Chapter 3. Open-loop suction control tests to reduce the separated flow over the aperture were performed for both the static and dynamic pitching configurations. For the dynamically pitching turret, closed-loop control tests were explored to improve upon the success of the open loop control at reducing the wake over the

turret.

The next set of tests examined the flow over a dynamically yawing hemisphere. The results of these tests are described detail in Chapter 4. In an attempt to reduce the fluctuating velocity caused by the motion of the turret, active flow control was applied over the hemisphere. Both open loop and closed loop flow control were employed to achieve a reduction in the separation levels over the aperture of the turret. The closed loop control system employed a multiple-input-multiple-output proportional controller to improve the efficiency of the actuation system.

Chapter 5 shows the results of aero-optic measurements taken in the Subsonic Aerodynamic Research Laboratory at Wright-Patterson Air Force base at Mach 0.3 and a Reynolds number of two million. OPD_{rms} measurements were taken at the center of the aperture for a fixed turret. Open loop suction control was implemented over the turret.

Finally, Chapter 6 lists the conclusions, future work, and general comments about this work.

Shown in Figure 4 is a 'road map' of experiment data taken and analyzed for the entire study. The road map provides a quick list of the experiments and where the results can be found.

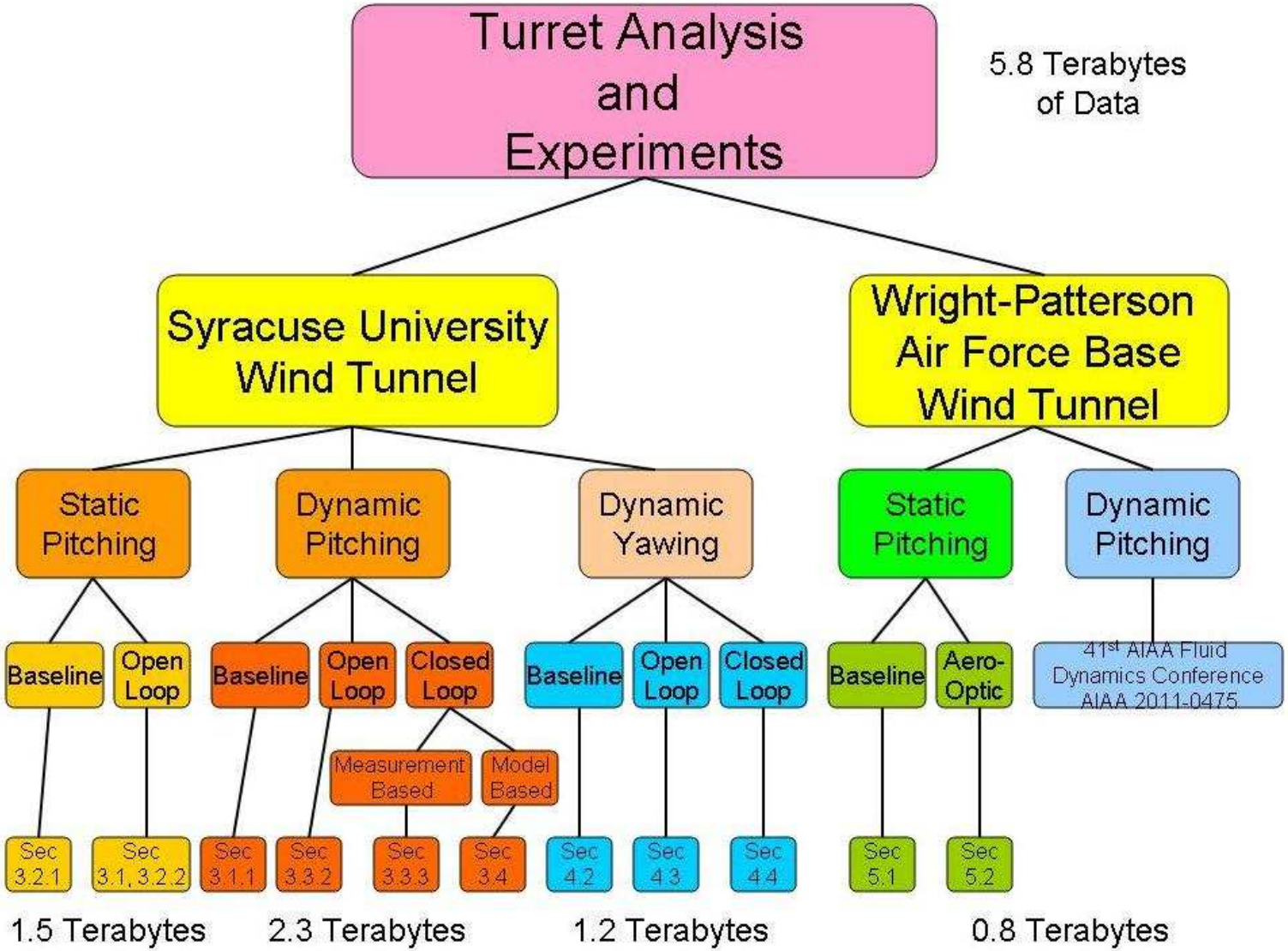

Figure 4: RoadMap

Chapter 1

Governing Equations and Low Dimensional Analysis

1.1 The Governing Equations

1.1.1 Navier-Stokes Equations

The flow over the turret that generates the aero-effects can be completely described at any instant by a set of equations known as the Navier-Stokes equations, defined in Equations 1.1. The Navier-Stokes Equations represent the rate of change in momentum and the sum of forces acting on a defined volume of fluid according to Batchelor [9]. As with all equations in this thesis, Equations 1.1 are written in a cartesian coordinate system using the index notation. The velocity field measurements over the turret were taken in Cartesian coordinates, therefore all equations are written in a Cartesian coordinate system.

$$\frac{\partial \rho \tilde{u}_i}{\partial t} + \frac{\partial \rho \tilde{u}_i \tilde{u}_j}{\partial x_j} = -\frac{\partial \tilde{p}}{\partial x_i} + \frac{\partial}{\partial x_j}\left(\mu\left[\frac{\partial u_i}{\partial x_j} + \frac{\partial u_j}{\partial x_i}\right]\right) - \frac{\partial}{\partial x_i}\left(\frac{2}{3}\mu\frac{\partial u_k}{\partial x_k}\right) + B \qquad (1.1)$$

The instantaneous velocity, pressure, and density are represented as $\tilde{u}_i$, $\tilde{p}$, and ρ respectively, μ is the dynamic viscosity, and B are the body forces acting on the fluid

such as gravity. The streamwise velocity is represented as u_1 in the x direction, while the cross-stream velocities are u_2 and u_3 in the y and z direction respectively. The index notation defines the components of direction as: $i = 1, 2, 3$ and $j = 1, 2, 3$.

The Syracuse University portion of the suction flow control experiments were taken at approximately Mach 0.1, thus the flow can be regarded as incompressible.

With the incompressibility assumption, ρ becomes constant and the compressible Navier Stokes equations can be rewritten as Equations 1.2.

$$\frac{\partial \tilde{u}_i}{\partial t} + \tilde{u}_j \frac{\partial \tilde{u}_i}{\partial x_j} = -\frac{1}{\rho}\frac{\partial \tilde{p}}{\partial x_i} + \nu \frac{\partial^2 \tilde{u}_i}{\partial x_j \partial x_j} + B \tag{1.2}$$

Since the ultimate goal of the flow control tests is to mitigate the density fluctuations that generate the aero-optic effects over the top of the turret, a question of the validity of the low speed experiments arises. As mentioned in the Introduction, Smits and Dussauge [68] observed that for an adiabatic flow there exists a strong correlation and a direct relationship derived from the Strong Reynolds Analogy between the density and velocity root mean square. Therefore, controlling the velocity fluctuations will control the density fluctuations. This justifies a flow control objective to reduce the fluctuating velocity at either low or high speeds, over the top of the turret.

1.1.2 Reynolds Decomposition

A key development in the study of turbulence is the Reynolds decomposition. Described in Tennekes and Lumley [75], Reynolds proposed that the instantaneous qualities can be "decomposed" into mean and fluctuating components. For example the instantaneous velocity, $\tilde{u}_i$, can be broken into a mean velocity, U_i, and a fluctuating

velocity, u_i, as seen in Equation 1.3.

$$\tilde{u}_i = U_i + u_i \tag{1.3}$$

A key feature of the Reynolds decomposition is that the average of the fluctuating component leads to $\langle u_i \rangle = 0$ and the average of the mean component is equal to itself, $\langle U_i \rangle = U_i$, by definition of U_i.

1.1.3 Continuity Equation

The flow of mass through the system must be conserved. This conservation of mass can be expressed as the continuity equation, as defined by Equation 1.4.

$$\frac{\partial \rho}{\partial t} + \frac{\partial \rho \tilde{u}_i}{\partial x_i} = 0 \tag{1.4}$$

Assuming the flow incompressible, $\frac{\partial \rho}{\partial t} = 0$ and using the Reynolds decomposition the continuity equation becomes,

$$\frac{\partial (U_i + u_i)}{\partial x_j} = 0. \tag{1.5}$$

Averaging Equation 1.5 and using the fact that the average of the fluctuating component is zero leads to Equation 1.6.

$$\frac{\partial U_i}{\partial x_j} = 0. \tag{1.6}$$

Therefore to satisfy the continuity equation,

$$\frac{\partial u_i}{\partial x_j} = 0. \tag{1.7}$$

1.1.4 Mean Momentum Equations

Applying the Reynolds decomposition to Navier Stokes equations and taking the average yields the mean momentum equation, defined as Equation 1.8.

$$U_j \frac{\partial U_i}{\partial x_j} = -\frac{1}{\rho}\frac{\partial P}{\partial x_i} + \nu \frac{\partial^2 U_i}{\partial x_j \partial x_j} - \frac{\partial \langle u_i u_j \rangle}{\partial x_j} \tag{1.8}$$

Explained by Tennekes and Lumley [75] and Hinze [35], within the mean momentum equation, the term $-\langle u_i u_j \rangle$ is a second order term which denotes the so called Reynolds "stress." The $-\langle u_i u_j \rangle$ represents the transfer of momentum between the mean flow and the turbulence by velocity fluctuations within the flow. A characteristic of the Reynolds stress term is that it is a symmetric matrix, $-\langle u_i u_j \rangle = -\langle u_j u_i \rangle$. In examination of the Reynolds stress, $-\langle u_i u_j \rangle$ can be separated into two parts: the off diagonal components and the on diagonal components. The diagonal components of the Reynolds stress term are the normal stresses and are represented as $\langle u_i^2 \rangle$. In many flows the normal stress contributes little to the mean momentum transfer. The square root of the normal stress becomes the root mean square of the fluctuating velocity or u_{rms}. The off diagonal components are considered to be the shear stress terms of the Reynolds stress. The shear stress is the dominant contributor to transfer of fluctuating flow to the mean flow. Both diagonal and off diagonal components of the Reynolds stress are useful terms to evaluate the level of fluctuating velocity within a flow.

It can be concluded from the high correlation between velocity and density fluctuations and Gladstone's relationship between the index of refraction and density fluctuations that the level of velocity fluctuations is indicative of the level of the index of refraction fluctuations. In either a compressible or incompressible flow, a control objective can be devised to drive the normal Reynolds stresses (see last term

on right hand side of Equation 1.8) to zero.

1.2 Proper Orthogonal Decomposition

To investigate the "big eddies" within turbulent flows, Lumley [43] proposed a statistical technique called Proper Orthogonal Decomposition, POD, to describe these coherent structures. The POD is an analysis which essentially decomposes the flow into ordered fluctuating energy modes according to Holmes et al. [36]. The development of the POD is based on the statistical technique of the Karhunen-Loève decomposition. The Karhunen-Loève decomposition has also been used to develop techniques to analyze random variables, image processing, signal analysis, data compression, oceanography, and chemical processes as described by Berkooz et al. [10]. A detail description of the development and utilization of POD can be found in Berkooz et al. [10] and Holmes et al. [37].

Axisymmetric jet work, done by Glauser et al. [29] was able to identify "ring-like" coherent structures and their evolution downstream within the flow by utilizing the POD. This work demonstrated experimentally the POD's ability to identify the coherent structures within a flow. The POD's ability to low dimensionally describe the flow was demonstrated by Glauser and George [30]. The velocity field was nearly reconstructed by using just the first three POD modes, at three diameters downstream of an axisymmetric jet exit. The first POD mode was also shown in this work to contain a significant percentage of the flow information. This work effectively demonstrated experimentally that the POD can be utilized for low dimensional analysis of the flow. Experimental implementation of the POD has been shown to be a powerful tool to identify coherent structures and low dimensional analysis the flow which can be used as feedback signal to closed loop control system.

Over the years, the classical POD that Lumley developed has evolved into various forms to analyze the flow. Introduced by Sirovich [66], the 'snapshot' POD solves the eigenvalue problem by using statistically time independent velocity maps or 'snapshots'. This method has been found to reduce the computation time to solve for the POD modes as compared to the classical POD technique. The 'snapshot' POD is a better fit for non-time-resolved data. Section 1.2.2 gives a more detail description of the 'snapshot' POD. The 'Global' POD shown by Glauser et al. [28] draws various sets of ensemble averaged flow cases together to give a more enriched description of the flow. The Split POD developed by Camphouse et al. [13] is a balanced truncation technique that separates the baseline energy flow from the other energies within the flow . This method is well suited to separate out the baseline flow energy from the actuation input energies in the flow.

The POD has been demonstrated successfully to be a powerful tool for modeling the flow. These models can be utilized for closed loop controller plants. The flow has been closely modeled by using a Galerkin projection of the Navier-Stokes onto the POD basis as shown by Ukeiley et al. [79]. Reduced Order Model (ROM) based on Galerkin projections of the Navier-Stokes onto the POD modes have been applied in various numerical flow control studies. Noack and Eckelmann [55] successfully applied a ROM, in a numerical study, to control the three dimensional wake of a cylinder in laminar flow. In another numerical study, Siegel et al. [65] employed a ROM, constructed from the first POD mode, in a proportional controller to reduce the amount of drag produced by a cylinder.

A general description of the Classical and Snapshot POD development is described below while a more specific derivation of the POD which encompasses the motion of the turret for the dynamic yaw case can be found in Section 4.4.1.

1.2.1 Classical POD

To find the modes of the flow, the velocity field is decomposed into a finite set of time-independent eigenfunctions (ϕ_j^n). An optimization equation, Equation 1.9, is constructed from the normalized mean square projection of the eigenfunctions on the velocity:

$$max \frac{\langle (u, \phi)^2 \rangle}{(\phi, \phi^*)}. \tag{1.9}$$

Projection onto the velocity occurs in the Hilbert space $\mathcal{L}^2$ of square-integrable functions, where (,) represents the inner product on $\mathcal{L}^2$.

The optimization of Equation 1.9 becomes the Fredholm integral eigenvalue problem, Equation 1.10. Employing Equation 1.10 over the spatial domain $\mathcal{D}$ calculates the eigenfunction solutions, where n is the mode number.

$$\int_{\mathcal{D}} R_{ij}(\vec{x}, \vec{x}') \phi_j^n(\vec{x}') d\vec{x}' = \lambda^n \phi_i^n(\vec{x}). \tag{1.10}$$

The ensemble averaged two point spatial correlation tensor is represented as R_{ij} and is derived from the sampled velocity, or other measurement, at t_0 as seen in Equation 1.11. The spatial correlation tensor is wide sense stationary meaning that the first and second moments do not vary with time.

$$R_{ij}(\vec{x}, \vec{x}') = \langle u_i(\vec{x}, t_0) u_j(\vec{x}', t_0) \rangle. \tag{1.11}$$

The eigenfunction solutions ultimately construct a normalized, orthonormal basis.

From the projection of the velocity onto the eigenfunction basis, a set of time dependent POD expansion coefficients ($a_n(t)$) are formulated, as seen in Equation

1.12.

$$a_n(t_0) = \int_D u_i(\vec{x}, t_0)\phi_i^n(\vec{x})d\vec{x} \tag{1.12}$$

These coefficients are uncorrelated,

$$\langle a_j a_k \rangle = \delta_{jk}\lambda^k, \tag{1.13}$$

where δ_{jk} is the Kronecker's delta function.

Kinetic energy contained within a particular mode (a_n) can be represented in the corresponding eigenvalue (λ^n). These eigenvalues are all positive and real values due to the real, symmetric, and positive definite matrix of the correlation tensor, R_{ij}. The sum of all of the eigenvalues is the total kinetic energy of the velocity field as seen in Equation 1.14, where N_m is the total possible number of modes.

$$\begin{aligned} E &= \frac{1}{2}\int_D \langle \vec{u}(\vec{x}, t_0)^2 \rangle d\vec{x} \\ &= \sum_{n=1}^{N_m} \lambda^n \end{aligned} \tag{1.14}$$

The percentage of the energy (ϵ) can be determined in Equation 1.15, where N is the number of modes utilized.

$$\epsilon(N) = \frac{\sum_{i=1}^{N} \lambda^i}{\sum_{j=1}^{N_m} \lambda^j} \cdot 100 \tag{1.15}$$

Full or partial reconstruction of the velocity field can be obtained by summing the product of the time-dependent POD coefficients ($a^n(t)$) and the POD eigenfunctions, as seen in Equation 1.16.

$$\vec{u_i}(\vec{x}, t) = \sum_{n=1}^{N} a_n(t)\vec{\phi_i^n}(\vec{x}). \tag{1.16}$$

Full construction of the velocity field can be obtained when $N = N_m$ and partial

reconstruction when $N < N_m$. For the classical POD, the number of modes (N_m) used is proportional to the number of velocity components (n_c) and to the spatial resolution (N_{gp}).

$$N_m = n_c N_{gp} \tag{1.17}$$

For a given number of modes, the percentage of the energy can be found in Equation 1.15.

1.2.2 Snapshot POD

First developed by Sirovich [66] in 1987, the snapshot POD is an alternate form of the classical POD. The snapshot POD is better suited for a database which is resolved in space instead of time, such as particle image velocimetry data. This method has been shown to be less computationally expensive than the classical POD. The possible number of snapshot POD modes is determined by number of temporal snapshots, T.

$$N_m = T \tag{1.18}$$

The Fredholm integral eigenvalue problem, Equation 1.10, is discretized by replacing $\phi_i^n(\vec{x})$ and $R_{ij}(\vec{x}, \vec{x}')$ with Equations 1.19 and 1.20 respectively.

$$\phi_i^n(\vec{x}) = \sum_{k=1}^{T} a_n(t_k) u_i(\vec{x}, t_k) \tag{1.19}$$

$$R_{ij}(\vec{x}, \vec{x}') = \frac{1}{T} \sum_{m=1}^{T} u_i(\vec{x}, t_m) u_j(\vec{x}', t_m) \tag{1.20}$$

Like the classical POD, the Fredholm integral eigenvalue problem is used to determine

the eigenfunctions, Equation 1.21.

$$\sum_{k=1}^{T} \frac{1}{T}[\int_D u_j(\vec{x}', t_m) u_j(\vec{x}', t_k) d\vec{x}'] a_n(t_k) = \lambda^n a_n(t_m) \tag{1.21}$$

From the eigenfunction solution, the two-point temporal correlation tensor is defined in Equation 1.22.

$$C(t, t') = \frac{1}{T} \int_D u_i(\vec{x}, t) u_i(\vec{x}, t') d\vec{x} \tag{1.22}$$

The spatial functions ($\phi^n(\vec{x})$) now can be defined in Equation 1.23 as the integration of projection of the POD expansion coefficients upon the velocity normalized by the eigenvalues (λ^n) and the sample size (T).

$$\phi_i^n(\vec{x}) = \frac{1}{T\lambda^n} \int_\tau a_n(t) u_i(\vec{x}, t) dt \tag{1.23}$$

Equation 1.24 verifies that the POD expansion coefficients are uncorrelated in time while the Equation 1.25 verifies that the eigenfunctions are orthonormal.

$$\langle a_m a_n \rangle = \lambda^m \delta_{mn} \tag{1.24}$$

$$\int_D \phi_i^p(\vec{x}) \phi_i^q(\vec{x}) d\vec{x} = \delta_{pq} \tag{1.25}$$

The velocity field now can be reconstructed with Equation 1.16.

1.3 Linear Stochastic Measurement (Estimation)

It was shown by Adrian [1] that a flow field can be estimated by employing the statistical information contained in a two-point velocity correlation tensor and instantaneous velocity measurements. This flow reduction method is termed the Linear

Stochastic Estimation (LSE), later called the Linear Stochastic Measurement (LSM) to better represent the technique. Utilizing the LSM, Cole et al. [17] successfully demonstrated that a spatially under sampled flow can still be accurately estimated.

The stochastically estimated term such as an estimated velocity field ($\widetilde{u}_i(\vec{x}', t)$) can be used in a conditional averaging scheme as the conditioned event as described in Equation 1.26,

$$\widetilde{u}_i(\vec{x}', t) = \langle u_i(\vec{x}', t) | u_i(\vec{x}, t) \rangle \tag{1.26}$$

where $\langle \mid \rangle$ represents the conditional averaging. The estimate can be expanded using the Taylor series expansion and rewritten in the form of Equation 1.27.

$$\widetilde{u}_i(\vec{x}', t) = A_{ij} u_j(\vec{x}, t) + B_{ijk} u_j(\vec{x}, t) u_k(\vec{x}, t) + \ldots \tag{1.27}$$

$$\widetilde{u}_i(\vec{x}', t) = \sum_{j=1}^{N} A_{ij} u_j(\vec{x}, t) \tag{1.28}$$

Higher order terms within the Taylor series expansion are truncated to reduce the dimensionality of the measurement. The Linear Stochastic Estimation (LSE) truncates the second order terms and higher, as seen in Equation 1.28, while the Quadratic Stochastic Measurement (QSM) truncates the third order terms and higher. Comparison of both the LSM and QSM by Tung and Adrian [77] found little improvement to estimate of the velocity with the QSM. Work done by Ausseur [8] also showed that although a form of the QSM, called the $mQSM$, improved the estimate of the flow field, the improvement was not significantly greater than the estimate from the $mLSM$. The LSM is a single-time, multi-point estimation problem.

The unknown estimation coefficients (A_{ij}) are determined by minimizing the mean square error (e_i) between the estimate and sampled measurement, as seen in Equation 1.29. Minimization of the mean square error is obtained by setting the derivative of

the error with respect to the estimation coefficient equal to zero.

$$\frac{\partial e_i}{\partial A_{ij}} = \frac{\partial \langle [\widetilde{u}_i(\vec{x}', t) - \widetilde{u}_i(\vec{x}', t)]^2 \rangle}{\partial A_{ij}} = 0 \tag{1.29}$$

The mean square error of the measurement estimation is defined in Equation 1.30.

$$e_i = \langle [\widetilde{u}_i(\vec{x}', t) - \widetilde{u}_i(\vec{x}', t)]^2 \rangle \tag{1.30}$$

A set of equations, Equation 1.31 arise from the minimization of the error in which the estimation coefficient can be solved by a simple matrix inversion.

$$\langle u_k(\vec{x}, t) u_j(\vec{x}, t) \rangle A_{ij} = \langle u_k(\vec{x}, t) u_i(\vec{x}, t) \rangle \tag{1.31}$$

1.3.1 Modified Linear Stochastic Measurement (Estimation)

Work done by Taylor and Glauser [74] further expanded the LSM to estimate the velocity flow field by utilizing the surface pressure field. This alteration to the LSM is known as the modified linear stochastic measurement $mLSM$. Built upon the fact that a strong correlation between velocity and surface pressure exist, the $mLSM$ engages a similar procedure as the LSM for finding the state of flow using pressure measurements.

The pressure is conditioned with the time dependent, velocity based POD expansion coefficients.

$$\widetilde{a}_n(t) = \langle a_n(t_s) | p_j(t) \rangle \tag{1.32}$$

Estimated expansion POD coefficients are expanded using the Taylor's series expan-

sion in Equation 1.33 and the higher order terms are truncated in Equation 1.34.

$$\widetilde{a}_n(t) = A_{nj}p_j(t) + B_{njk}p_j(t)p_k(t) + \dots \tag{1.33}$$

$$\widetilde{a}_n(t) = \sum_{j=1}^{N} A_{nj}p_j(t) \tag{1.34}$$

The mean squared error between the estimated POD coefficients and the fluctuating pressure is minimized in Equation 1.35 to form a series of linear equations as seen in Equation 1.36.

$$\begin{aligned} \frac{\partial e_{\widetilde{a}_n}}{\partial A_{nk}} &= \frac{\partial \langle [\widetilde{a}_n(t) - a_n(t)]^2 \rangle}{\partial A_{nk}} \\ &= \frac{\partial \langle [A_{ni}p_i(t) - a_n(t)]^2 \rangle}{\partial A_{nk}} \\ &= 0 \end{aligned} \tag{1.35}$$

$$\langle p_j(t_s)p_j(t_s)\rangle A_{nj} = \langle a_n(t_s)p_j(t_s)\rangle \tag{1.36}$$

1.4 Complementary Technique

By combining the POD with the LSM technique, Bonnet el al. [12] were able to estimate the flow more accurately with just the first mode than POD alone. The complementary technique utilizes the strengths of both POD and LSE methods to accurately estimate the structures with the flow, even if the flow is spatially under sampled, as seen in the work done by Cole et al. [17]. Thus, allowing for less need for a large number of resources to sample the flow. The modification of the complementary technique by Taylor and Glauser [74] showed the benefit of using fluctuating pressure instead of time resolved velocity. They demonstrated a more practical measurement that can be used to estimate the flow field using the modified

complementary technique.

Work done by Glauser et al. [28] showed that the estimated flow over a NACA 4412 airfoil from the complementary technique had sufficient flow information that it can be used as a feedback signal. A closed-loop flow control experiment performed by Pinier et al. [58] successfully showed a delay in the onset of stall over a NACA 4412 airfoil using a measurement-based estimator feedback control system. Outfitted with synthetic jets near the leading edge, a simple proportional controller fed back a velocity\pressure based low dimensional signal to the actuators. This experiment demonstrated the strength of the complementary technique to reduce the complexities of a turbulent flow into modes that accurately describe the flow in real time. Thus, a practical closed loop control can be implemented using non-time resolved velocity data and spatial under sampled, fluctuating pressure data.

In addition to the work presented in this thesis, a supplemental flow control experiment was performed in conjunction with Clear Science Corp. Using both numerical and experimental data, Thirunavukkarasu et al. [80] constructed a measurement and dynamical estimator for a proportional-integral (PI) closed loop controller. The complementary technique was employed to build a measurement estimator from the velocity and surface pressure data from the dynamical pitching, simple proportional control case. A Reduced Order Model was constructed for the dynamical estimator by projecting the Navier-Stokes equations onto the POD modes of the dynamical pitching, simple proportional control case from Section 3.3.1. To improve the performance of the dynamical estimator, a Kalman filter was included within the design of the closed-loop controller to help predict the incoming feedback signal. Using the measurement and dynamical estimators along with the Kalman filter, the PI controller was developed and tested for the dynamically pitching turret in the Syracuse University wind tunnel. Instead of trial and error to find the gains for the controller,

the gains were calculated using a Linear Quadratic Regulator. The feedback controller was found by Wallace et al. [84] to be more efficient at reducing the velocity fluctuations than the simple proportional controller in Section 3.3.3. A more detailed description of the model-based controller can be found in Section 3.4.

To reduce the turbulence levels in the highly three dimensional flow over the aperture of a dynamically yawing turret, a measurement estimator was developed for a multiple input multiple output, proportional feedback controller, seen in Section 4.4. The measurement estimator was constructed by determining the complementary expansion coefficients of the baseline dynamically yawing case in Section 4.1. The development and construction of the measurement estimator based controller can be found in Section 4.4.1.

Chapter 2

Facilities and Equipment

2.1 Syracuse Facility and Flow Conditions

The first set of tests was conducted in the Syracuse University (SU) wind tunnel. The wind tunnel is a closed circuit, Gottingen type wind tunnel capable of reaching speeds up to $65 m/s$. The test section of the wind tunnel is 0.61 by 0.61 by 2.43 meters with plexi-glass walls, allowing for optical measurements such as Particle Image Velocimetry (PIV). Air temperature within the wind tunnel was maintained at a constant temperature of 29.4° Celsius by means of an internal heat exchanger. The average atmospheric pressure was $99.8 kPa$, average air density was $1.21 kg/m^3$, and dynamic viscosity was $1.97 \times 10^{-6} kg/m \cdot s$.

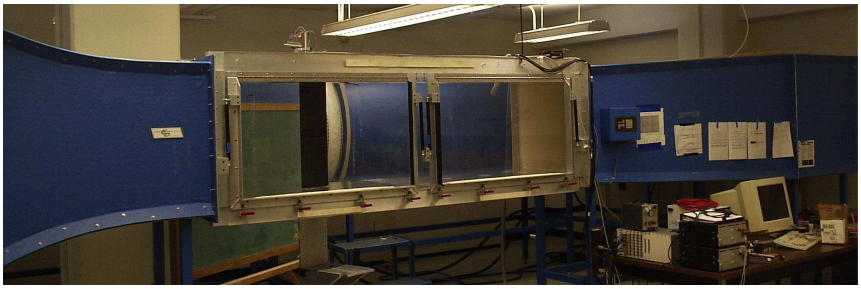

Figure 2.1: Syracuse University Wind Tunnel.

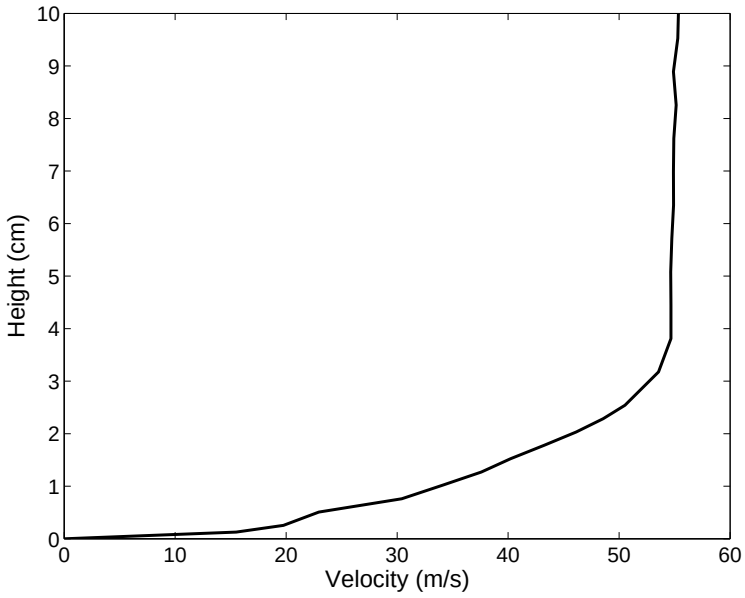

Figure 2.2: Boundary layer velocity profile above the wind tunnel floor and ahead of the turret.

Freestream velocity of the wind tunnel was set to $53m/s$ for all of the SU tests. At this set freestream velocity, the velocity profile of the boundary layer ahead of the turret is seen in Figure 2.2. The velocity was measured with a hot wire anemometry system, which is described in further detail in Section 2.5. The velocity was sampled at $10kHz$ for 10 seconds at 29 locations above the floor and $5.0cm$ forward of the test model. The thickness of the boundary layer is approximately $\delta = 3.46cm$, based on the distance from the floor to where the velocity becomes 99% of the freestream velocity. Non-dimensionalizing the boundary layer thickness by the height of the turret, H, leads to $\delta/H = 0.183$.

Figure 2.3: SARL Wind Tunnel.

2.2 Subsonic Aerodynamic Research Laboratory

Additional testing was performed at the Subsonic Aerodynamic Research Laboratory (SARL) wind tunnel at the Wright-Patterson Air Force. SARL is a suck-down, open-circuit wind tunnel that has the capacity to generate freestream velocities from Mach 0.1 to 0.5. The air temperature, atmospheric pressure, and air density are set by outside environment conditions and operation is subject to weather conditions.

The cross sectional area of the test section is 2.13 by 3.05 meters and is constructed with glass windows on all four sides, allowing for optical measurements access such as a Malley probe and a PIV system. A view of the SARL wind tunnel is pictured in Figure 2.3.

2.3 Syracuse University Test Model

The Syracuse University test article is a three dimensional turret which consist of a hemisphere top mounted on top of a cylinder, see in Figure 1(a). The diameter of

the turret (D) is 15.2cm and with a height (H) of 19.1cm, giving an aspect ratio (AR) of 1.25. Using Equation 1 the Reynolds number (Re) is approximately $500,000$ based on free stream velocity and the diameter of the turret. The shell of the turret is constructed out of Somos 11120 low viscosity liquid photopolymer through the rapid prototyping process of stereolithography. A flat aperture of 7.11 centimeters is located on top of the hemisphere portion. The aperture was set to face downstream in each test at a given elevation angle, α, relative to the floor of the wind tunnel. The interface between the hemisphere and cylindrical portions are tight enough to prevent air through while loose enough not to impede rotation of the hemisphere. Around the aperture is an array of twenty slots arranged in two rows. A single slot has a cross-sectional exit area of 0.116cm^2. These slots were used to bleed air from the surface around the aperture in a pulse-width manner. It has been shown by Lundell [44] that pulse-width actuation can produce accurate control input and is suitable for flow control. Manifolds and vacuum lines connect the slots to a set of solenoid valves that control the flow through the suction system. The suction is generated by a set of continuous pull vacuum pumps.

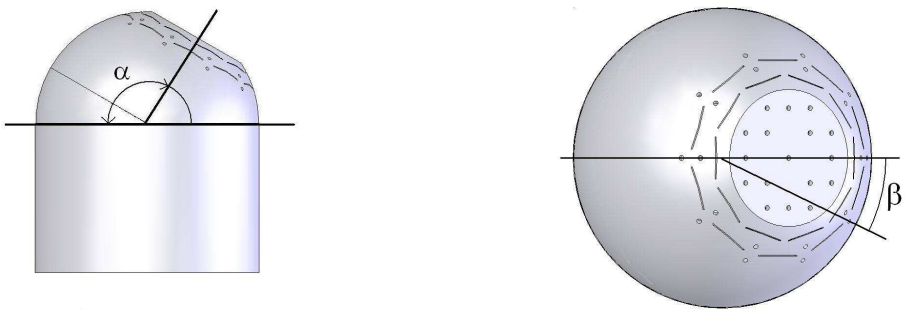

(a) Pitch (Elevation) Angle (b) Azimuthal (Yaw) Angle

Figure 2.4: Two examples of the laser housing.

The vacuum system consists of vacuums pumps, vacuum reservoir tanks, mani-

folds, and valves. Two Welch 1405 vacuum pumps draw down two vacuum reservoir tanks to a pressure of $6,205$ Pascals at a rate of $91 L/min$. The reservoir tanks ensure steady suction through the vacuum lines up to the valves. For flow modulation, two solenoid valves are imbedded into the vacuum lines. These valves are Parker Hannifin solenoid valves, which have a maximum time response of 2.0 milliseconds and a coefficient of volume (C_{vol}) of 0.59. The coefficient of volume is defined as flow through (q) the valve over the pressure drop (Δp), as seen in Equation 2.1.

$$C_{vol} = q\frac{SG}{\Delta p} \tag{2.1}$$

The specific gravity of the fluid is represented as SG. As a result of the valve operational time response, the maximum operational frequency with a full duty cycle range is $25 Hz$. The operation frequency has a non-dimensional frequency of $f^+ = 0.335$ based on Equation 2.2.

$$f^+ = \frac{fL}{U_\infty} \tag{2.2}$$

The f^+ is a function of frequency (f), a characteristic length L (the aperture diameter), and freestream velocity U_∞. The duty cycle, DC, is defined as the ratio between time on to the period of the output signal, $\mathcal{T}$. Any higher operational frequency will decrease the duty cycle range. Valve position is limited to fully open and fully closed with the valve normally closed. Given this valve characteristic, flow modulation is obtained through duty cycle modulation. Seen in Cattafesta and Sheplak [16], the performance of an actuator which has a momentum flux such as the suction system is quantified as the coefficient of momentum, defined in Equation 2.3,

$$C_\mu = \frac{\rho_{slot} U_{slot} A_{slot}}{\rho_\infty U_\infty A_{ref}} \tag{2.3}$$

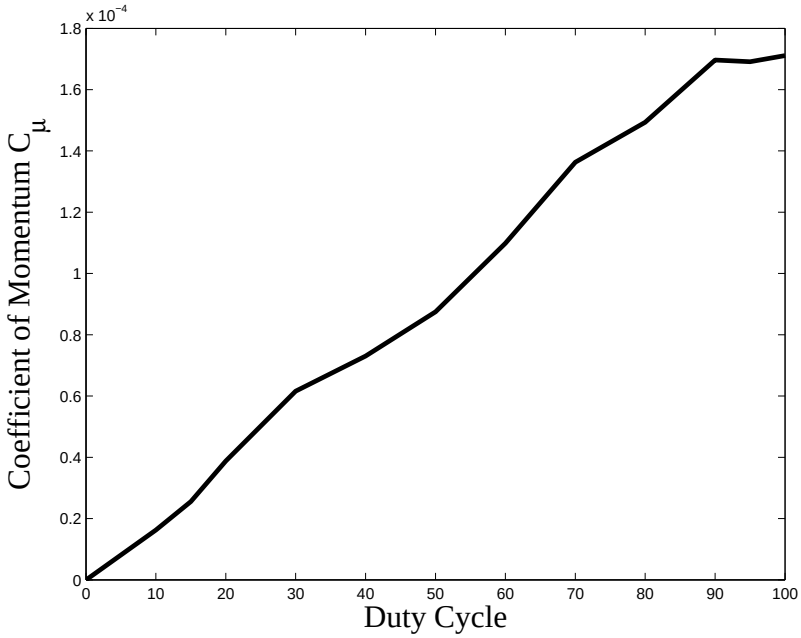

Figure 2.5: The relation between duty cycle and slot suction velocity in terms of coefficient of momentum.

where U_{slot} is the suction velocity, U_∞ is the freestream velocity, A_{slot} is the suction slot cross-sectional area, and A_{ref} is the wind tunnel cross sectional area. The suction flow at the slot exit, ρ_{slot}, is assumed to be equal to the freestream density, ρ_∞.

The hemisphere component of the turret is able to rotate in two directions: pitch and yaw. Rotation is controlled by two stepper motors that are attached to the hemisphere through a series of gears and linkages. The stepper motors are high torque LIN ENGINEERING motors capable of $2.08N-m$ of torque, an angle step of 0.45° per step, a maximum rotation rate of $10deg/sec$. Rotation control is maintained by a RMS Technologies $R208$ Microstepping Driver. A digital signal sent to the driver controls rotation position, rate, and direction of the motor.

2.4 Air Force Test Model

The Air Force test model consist of a three dimensional turret mounted in the center of the test section on a 0.61 by 0.91 meter splitter plate with a rounded front. The Air Force turret is scaled up from SU turret, thus both models have similar features. The test model is pictured in Figure 1(b). The diameter of the turret is $30.48cm$ and the height is $22.86cm$, giving an aspect ratio of $AR = 0.75$. The flat aperture on the hemisphere is $12.7cm$ in diameter. Located in the center of the aperture is a $5.08cm$ diameter optically flat mirror. Twenty suction slots arranged in two rows are located around the aperture. The cross sectional area of a single slot is $0.387cm^2$.

The majority of the turret's shell is machined from 6064 aircraft grade aluminum. The suction slots consist of four manifold inserts made of Somos 11120 low viscosity liquid photopolymer and constructed by the rapid prototyping process of stereolithography.

Each manifold contains five suction slots and are connected by vacuum tubes to an ASCO solenoid valve. The valves have a time response of 0.5 milliseconds and a C_{vol} of 0.59. Suction control is obtained through duty cycle modulation. The valves are run at a frequency of 25 Hz. A single vacuum reservoir tank ensures steady suction up to the solenoid valves. Suction is generated by a SV630 B Cerlikon vacuum pump capable of pulling $640m^3/h$ and reaching a vacuum pressure of $100Pa$.

Like the SU test model, the hemisphere is capable of rotating in two degrees of freedom: pitch and yaw. Rotation in both directions is controlled by two high torque AC motors with speed controllers. Maximum rotation rate of the hemisphere is $3deg/sec$ and position is controlled by employing an encoder for tracking.

Construction of the SARL turret and assembly of the rotation mechanism was completed by ATK Engineering.

2.5 Data Acquisition

2.5.1 Pressure Transducers

Located on the surface of the hemisphere of the SU turret are 30 pressure transducers which measure the fluctuating, static surface pressure. Figure 2.6(a) shows the location of the sensors on the SU turret: 16 transducers on the aperture and 14 around the aperture in two rows. The SARL turret has 28 pressure sensors distributed on and around the aperture: 20 sensors around the aperture and 8 on the aperture. The pressure arrangement of the SARL model is seen in Figure 2.6(b).

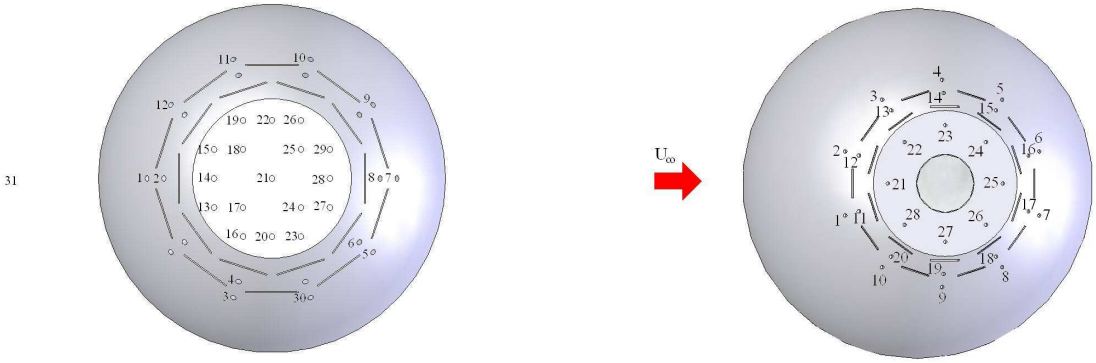

(a) SU Model (b) SARL Model

Figure 2.6: Pressure Transducer Locations.

The pressure transducers are PCB Piezotronic 103B Acoustic ICP sensors with built in solid state electronics and acceleration compensation. The pressure range of the sensors is $23,000Pa$ with a resolution of $78dB$, and a frequency bandwidth of $5Hz$ to $13kHz$. Measurement of the fluctuating pressure is achieved by deflection of an internal diaphragm. The amount of deflection is directly proportional to the pressure which also corresponds to a proportional change in voltage. Equation 2.4 is

employed to relate voltage to pressure, either in metric or standard units.

$$P = \frac{Volts}{sensitivity(\frac{V}{Pa})} \tag{2.4}$$

The sensitivities for the pressure sensors are provided by the manufacture and are listed in Appendix 6.2 for both the SU and SARL tests. The sensors have a circular measurement area of $1.61\pi\ mm^2$. Key components of transducers, such as the diaphragm, are constructed out of Invar and the sensing element is made of a ceramic material.

For both SU and SARL, the pressure sample rate was set to $10kHz$ with a low pass filter of $4.5kHz$ to prevent aliasing of the signal. This sample rate was set to ensure time resolved pressure measurements and to acquire high frequency, pressure structures within the flow.

2.5.2 Hot Wire

Velocity measurements of the flow through the suction slots and boundary layer measurements of the SU wind tunnel were taken with a Dantec Constant Thermal Anemometry hot wire system. The constant anemometry system, described by Tavolaris [73], uses convective heat transfer over a hot wire probe at a constant temperature to measure the velocity in the flow. A hot wire probe is a $5\mu m$ diameter tungsten wire soldered to a two prong probe holder. As the fluid passes over the wire, heat from the wire is convected into the flow which results in a change in resistance of the wire. A constant temperature is maintained by applying an electrical current to the wire. To maintain the constant temperature of the wire in an unsteady flow, a feedback system is employed to adjust the current to heat the wire.

The feedback system senses the change in resistance due to the flow of the wire

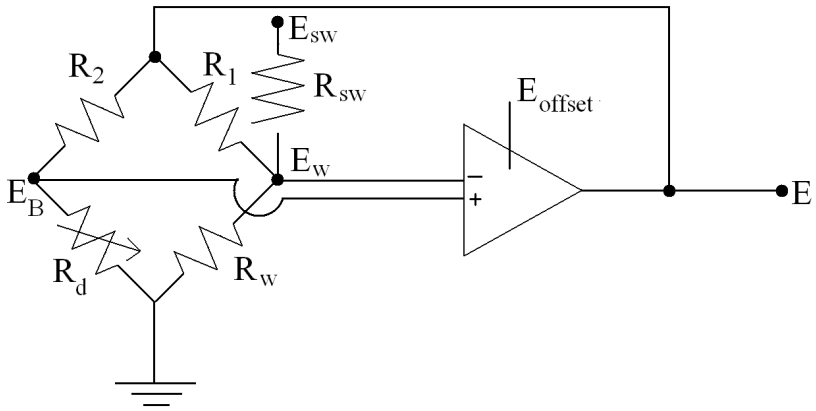

Figure 2.7: The Wheatstone bridge circuitry.

through a Wheatstone bridge circuitry. The circuitry of the hot wire anemometry system can be seen in Figure 2.7, where the R_W is the hot wire resistance and R_d is an adjustable decade resistor. When the R_W changes the bridge is put out of balance, the amplifier responds by outputting a voltage to the bridge. This voltage alters the current sent to the hot wire, generating Joule heating within the wire. When the temperature of the wire reaches its original setting the bridge is again in balance. The DC voltage required to heat the wire is recorded. The relationship of the velocity to the balance voltage is nonlinear. Voltage (v) is calibrated to velocity by fitting a fourth order power function to several known velocities versus the output voltage data, Equation 2.5.

$$u(t) = Av(t)^4 + Bv(t)^3 + Cv(t)^2 + Dv(t) + E \tag{2.5}$$

The calibration coefficients are then applied to the measured hot wire data to output the velocity.

The hot wire system is described in more detail in Perry [57].

A single hot wire probe was used at a sample rate of $10kHz$ and analog filtered at $5kHz$, giving a time resolved measurement of the velocity.

2.5.3 Particle Image Velocimetry

The velocity field over the turret was sampled with a *Dantec Dynamics* Particle Image Velocimetry system (PIV). A PIV system is an optical based measurement system that non-intrusively captures a two-dimensional plane of velocity as explained by Raffel et al. [60]. The PIV system is seen in Figure 2.8.

The flow within the closed circuit wind tunnel is seeded with atomized olive oil. The olive oil is atomized using a Laskin nozzle, producing an average particle size ranging between 1 to 5 μm which are estimated to follow the flow beyond the frequencies of interest. Injected upstream of the blades, the seed is evenly mixed to generate a homogenous distribution of olive oil in the test section. Atomized olive oil is shown by Melling [48] to follow the flow well and has high illumination for 200 mJ Nd:Yag laser light.

Seed within the flow over the turret is illuminated by a dual pulsing laser system with laser sheet generator optics. The laser system is a New Wave Research 200mJ Nd:YAG with dual pulsing lasers, capable of pulsing at a rate of 15 Hz each. Two lasers are utilized to be able to obtain consecutive pulses microseconds apart.

While the flow is illuminated by the lasers, the particle position is captured by a set of high speed cameras. Two HiSense, 8-bit CCD cameras with a pixel size of 1280×1024, are used to obtain two windows of the flow. Each camera records a pair of images microseconds apart corresponding to two laser pulses. The cameras are capable of recording at maximum rate of 4 Hz, thus setting the maximum velocity sample rate to 4 Hz. Due to the slow sampling rate the velocity obtain through the

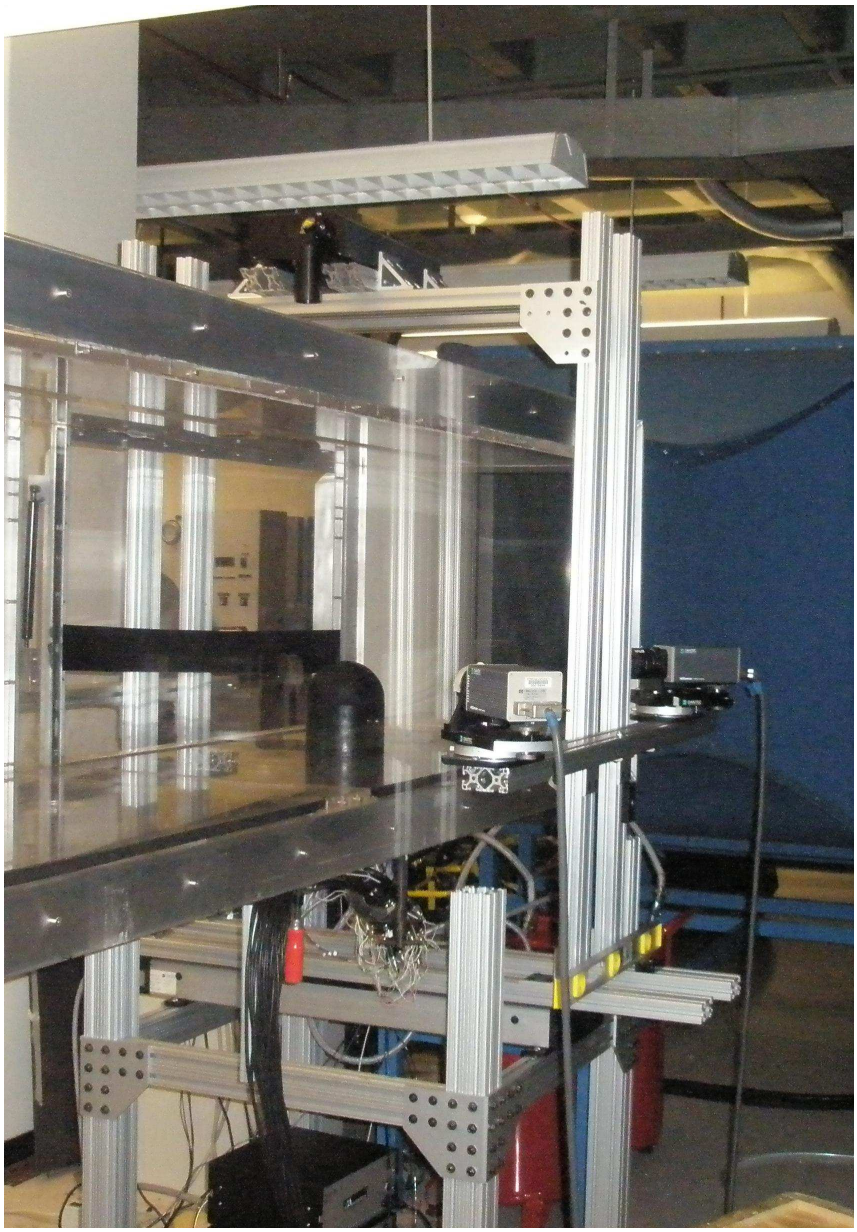

Figure 2.8: PIV setup to take two component measurements.

PIV is not time resolved but is spatially resolved.

The velocity field is calculated using the *Dantec Dynamics* Flow Manager software. This software tracks the movement of particles between the image pairs. The full field-of-view window is broken up into smaller iteration windows of 32×32 pixels with an overlap of 50%. Timing between the image pairs is set to allow a particle in the freestream to move a fourth of the iteration window, giving a fire timing of $20\mu s$. Flow Manger employs an adaptive correlation scheme between the image pair to determine the distance the particles move within an iteration window. The velocity of the particles is then calculated with this distance and the time between image pairs.

Calibration is required to relate the field-of-view distance to the pixel number and the perspective of the due to the angle between the camera and laser. A target plate is used to calibrate the angle position and the distance of the laser to the cameras. During imaging processing of the velocity, the perspective of the camera is adjusted by the calibration.

For the static and dynamic pitching experiments, the PIV is setup to capture two components of the velocity field at the centerline of the turret. The two cameras are utilized to expand the overall sample velocity field size by looking at different areas except for a small overlapping area to ensure correct frame of reference for each window. After calibrating the field of view and merging the two windows from both cameras, the overall window size is 310 mm×125 mm. The iteration area of 32×32 pixels is 1.7mm×1.7mm.

The PIV is setup to acquire three components of the velocity field at the centerline for the dynamic yaw. This requires the two cameras to look at the same field of view. Calibration of the camera windows gives a field of view of 283 mm×202 mm and an iteration area of 4.3 mm×4.3 mm.

It is important to note that although the flow over the turret is highly three dimensional, only the center plane of the turret is shown as an indicator of the state of the flow.

A more extensive description of the theory and operation of a PIV system can be found in Raffel et al. [60].

2.5.4 Malley Probe

Aero-optic measurements were collected in the SARL wind tunnel using a Malley probe manufactured by Innovative Technology Applications Company. The Malley probe is a single point measurement system that directly obtains the optical phase variance due to the wavefront aberrations in a turbulent region. The operation of the Malley probe assumes that the optical aberrations convect through the optical aperture as shown by Malley et al. [45]. Explained in further detail Gordeyev et al. [34], the OPD_{rms} is calculated by assuming frozen flow and convection through the optical aperture. A schematic of the basic set of the Malley probe can be seen in Figure 2.9.

Operation of a Malley probe is dependent on the assumption of the Huygens' Principle, which states that light will emerge from a variable index of refraction wavefront, W, perpendicularly, defined in Welford [87]. Thus, a collimated light beam propagating through a fluctuating density region will emerge at an aberration angle (θ), described in Equation 2.6,

$$\theta(x, y, t) = -\arctan(\frac{\varepsilon}{d}), \tag{2.6}$$

where ε is the displacement of the original beam angle to the new angle and d is the distance from the aberrated wavefront to the probe. Utilizing the Huygens' Principle,

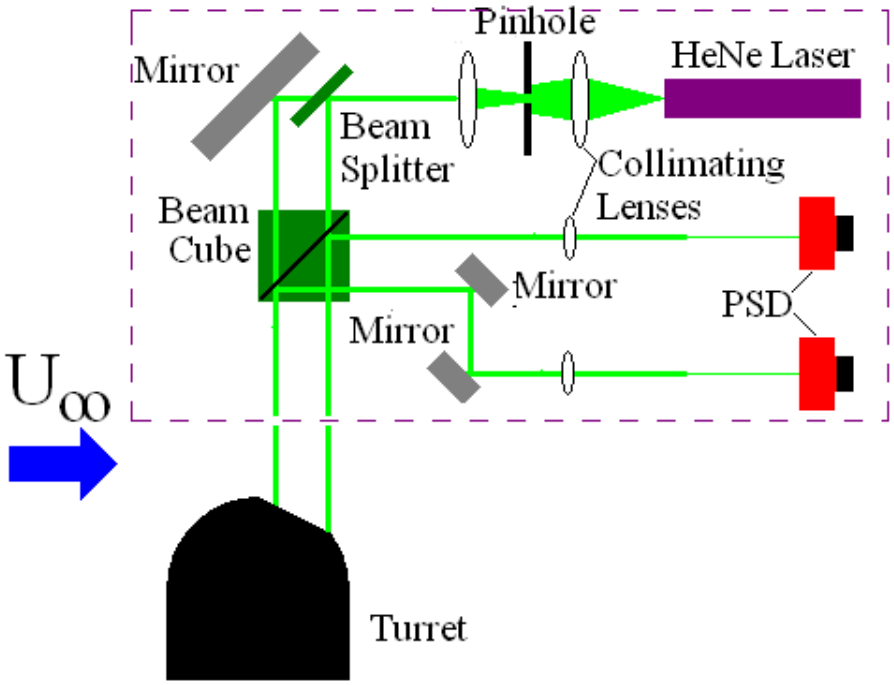

Figure 2.9: Drawing of Malley Probe Setup.

the slope of the aberrated wavefront is related to the emerging light beam angle (θ), as defined in Equation 2.7.

$$\frac{d}{dx}W(x,y,t) = \theta(x,y,t) = -\arctan(\frac{\varepsilon}{d}), \tag{2.7}$$

Using the relationship between the aberrated wavefront (W) and the aberration angle (θ), Hugo and Jumper [38] showed that the OPD can be determined from the defection as shown in Equation 2.8,

$$OPD(x,y,t) = -U_C \int_0^t \theta(x,y,t)dt, \tag{2.8}$$

where U_C is the convective velocity of the density fluctuations.

The Malley probe utilizes a continuous Helium-Neon laser, with a wavelength of $\lambda = 633nm$, to produce an optical test beam. This beam is collimated through a series of lenses. Next, the collimated beam is then split into two separate beams at a distance of $4cm$ through a beam splitter. This sets the Malley probe lasers distance to be $\Delta = 4cm$. The two beams are refocused after it passes through a beam cube. The split laser beams are adjusted to be aligned to the freestream flow and are propagated towards the $5.08cm$ diameter, flat optical mirror in the center of the turret aperture in the wind tunnel. After passing through the turbulent flow, the distorted light is reflected back to the optical system by the flat mirror along the same path that they were propagated. The distorted beams are directed by the beam cube to a set of position-sensing devices (PSDs) per beam. The PSDs are placed one focal length from the beam cube to ensure that the focus of the incoming beams are independent of the angle of incidence. This setup is represented in Figure 2.10.

The position-sensing device (PSDs), seen in Figure 2.11(a), records the relative

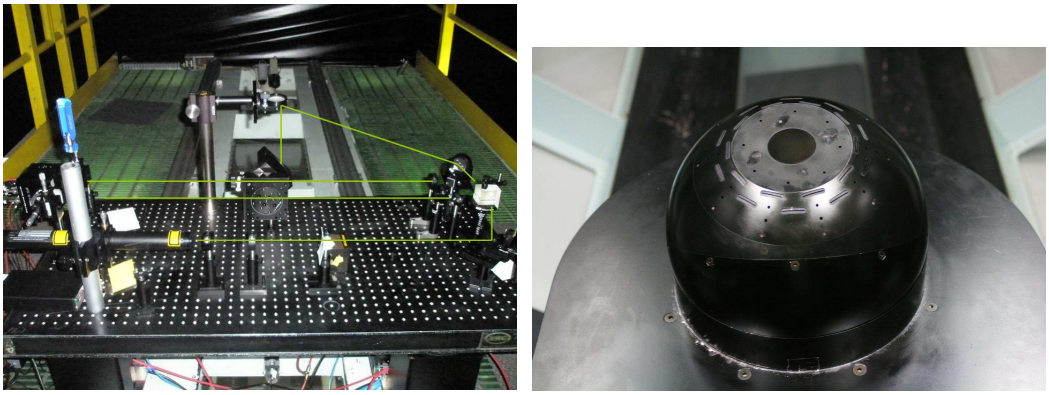

(a) Malley Probe (b) Optical mirror

Figure 2.10: Malley Probe set up.

displacement from the center of the senor of the distorted light beams. A corresponding voltage is generated for a given displacement from the center of the sensor. Figure 2.11(b) shows the tetra-lateral sensor grid, position delectability. The tetra-lateral grid has a nonlinear relationship between voltage and displacement. A calibration of distance versus voltage is required to obtain this relationship.

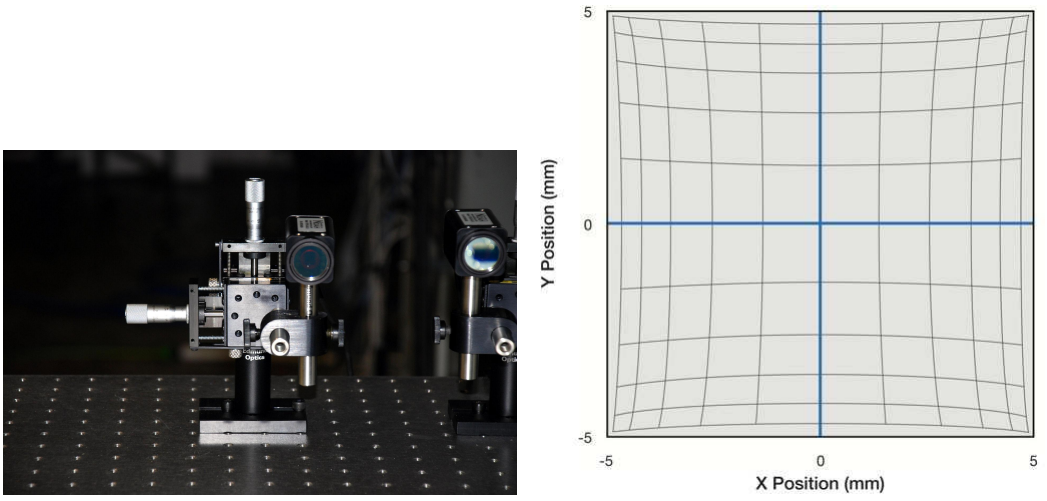

(a) PSD (b) Sensor Grid

Figure 2.11: Position Sensor Device and the sensor grid.

The Malley probe data was sampled at $100kHz$ and digitally filtered at $50kHz$, in order to capture the high frequency, convective structures responsible for the optical aberrations. At this sampling rate the measurements are time resolved.

2.5.5 Acquisition Hardware

Both SU and SARL tests utilized the same data acquisition system, a National Instruments (NI) PXI system. The acquisition system simultaneously took measurements, outputted control signals, and controlled the turret rotation.

The data acquisition system is a combination $PXI\backslash SCXI1052$ Chassis with Integrated Signal Conditioning. It houses analog input and analog/digital output modules including a PXI $81962.0GHz$ Pentium M 760 and Embedded Controller. The controller is a target-host, real time system to ensure real time measurements. A dedicated NI PXI\SCXI computer (target computer) is controlled by a laptop computer (host computer) through a network. All data acquisition programs are run on the host computer, which sends the program through the network to the target computer. The use of a dedicated NI PXI\SCXI computer ensures that the data collection and signal generation is not delayed by an operating system such as Windows.

Both analog and digital output signals are sent with a PXI 6733 Analog/Digital Output Module. The module contains eight analog and 10 digital output signal ports. Although the system is capable of sending a signal at $20kHz$ per channel, the output signals for each device in both test facilities were set at $1000Hz$ to reduce computation demand. Position and speed of the SU turret is control by outputting a digital signal from the PXI 6733 Analog/Digital Output Module to the stepper motor, while rotation of the SARL turret is executed with an analog signal. Both the solenoid valves in the SU and SARL turret are controlled with a square wave analog

signal.

The pressure transducers are plugged directly into a National Instrument SCXI 1531 Eight Channel, Accelerometer Input Module which is capable of simultaneously sample and hold and a resolution of 24 bits. The module is an analog to digital converter with a programmable low pass Bessel filter which supplies a constant excitation current of $4mA$ to the pressure transducers. Also recorded by a SCXI 1531 module channel is the PIV trigger, thus linking velocity and pressure in time. The peak of the trigger represents a PIV recording. Four SCXI 1531 modules are required to record all of pressure sensor and PIV trigger signals simultaneously.

Both Malley probe data and hot wire measurements are recorded with a PXI 4472 24-Bit Eight Channel Dynamic Signal Acquisition module. The module has a built in analog filter to prevent aliasing.

Chapter 3

Flow Control of a Pitching, Three Dimensional Turret

A series of suction flow control experiments were conducted in the Syracuse University wind tunnel over a three dimensional turret. The freestream of the wind was maintained at a constant Mach number of about 0.1, which gives a Reynolds number of approximately 500,000 based on the freestream velocity and diameter of the turret. The hemisphere of the turret was both statically and dynamically pitched within this set of experiments.

3.1 Suction Actuation at Various Slot Locations

The first set of experiments investigated steady suction actuation at various locations while the pitch angle was set at $\alpha = 120^{\circ}$ and a Reynolds number of $500,000$. Each panel of Figure 3.2 shows normalized mean velocity magnitude ($\langle\sqrt{\tilde{u}_1^2 + \tilde{u}_2^2}\rangle/U_\infty$) contour plots for each actuation case, averaged over 1000 instantaneous velocity snapshots. As mentioned in Section 2.5.3, only the center plane of the turret is shown to provide an indicator of the state of the flow throughout this chapter. All velocity measurements for the static elevation angles were averaged over 1000 snapshots. This provided enough samples for the statistics to converge.

At $\alpha = 120°$ the flow over the aperture was fully separated from the aperture as seen in the average velocity contour plot of Figure 3.2(a). Velocity measurements obtained at the exit of activated suction slots found that the suction velocity was on average 15.2 m/s per slot. At this suction velocity the coefficient of momentum, defined in Equation 2.3, is $C_\mu = 2.04 \times 10^{-4}$ per slot. Five different slot arrangements, shown in Figure 3.1, were examined: back nine slots on (Slots 7 - 10, & 16 - 20), front five slots on (Slots 11 - 15), front 11 slots on (Slots 1 - 6, & 11 - 15), and all slots on (Slots 1 - 20). Table 3.1 shows the corresponding coefficient of momentum for each suction case.

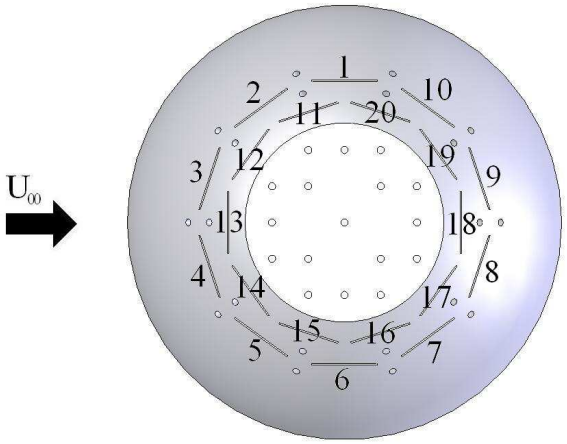

Figure 3.1: Slot arrangement of the SU turret model.

Suction case	C_μ
Back Nine Slots On	18.4×10^{-4}
Front Five Slots On	10.2×10^{-4}
Front Eleven Slots On	22.4×10^{-4}
All Slots On	40.8×10^{-4}

Table 3.1: Coefficient of momentum for the various slot arrangements.

Comparing the no actuation case in Figure 3.2(a) to the full suction case in Figure

3.2(e), it is clearly demonstrated that suction has enough control authority to reduce the size of the wake above the aperture. The flow went from being fully separated to attach. As mentioned in Section , the suction flow is bleeding air from the boundary layer, which prevents the flow from separating. To a lesser extent, Figures 3.2(b), 3.2(c), and 3.2(d), correspond to back nines slot on, front five slots on, and front eleven slots on respectively, show levels of flow separation reduction as well.

Figures 3.2(c), 3.2(d), and 3.2(e) indicate that the flow is attached to the aperture due to suction.

This set of experiments also exhibits the varying spatial receptivity of the flow to the control input. Only a slight decrease in the wake size behind the turret was seen in the case where the back nine slots were activated (Figure 3.2(b)). On the other hand, a significant decrease in the wake behind the turret was observed in the case where the front five slots were activated (Figure 3.2(c)). With similar coefficients of momentum, the actuators forward of the aperture exhibit a greater amount of control authority due to their location. This indicates that the flow is more receptive to the forward actuators than the aft actuators at this pitch angle. Although the back slots have little effect at 120°, they still could be aiding by keeping the flow attached to the aperture at shallower angles.

3.2 Multiple Static Elevation Angles

Measurements were taken with no suction actuation at a range of static elevation angles at an azimuthal angle of zero: 110°, 114°, 115°, 116°, 120°, 125°, and 130°. The wind tunnel was off when setting the fixed elevation angle of the aperture. At the elevation angles in which the flow was separated over the aperture, various open loop control modulations were explored.

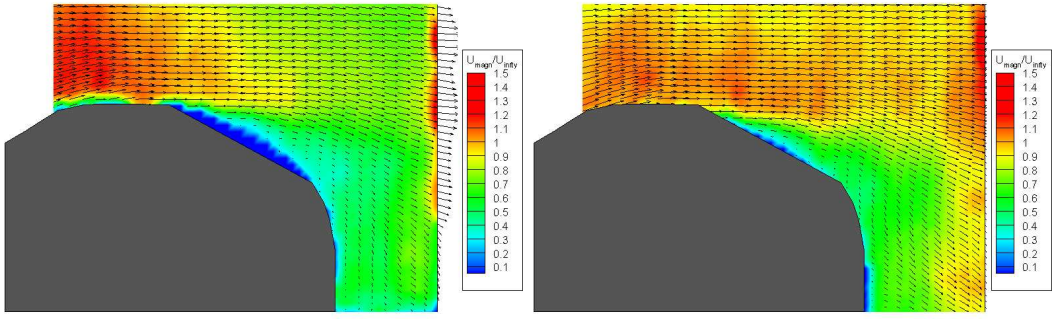

(a) No Suction

(b) Back Nine Slots On

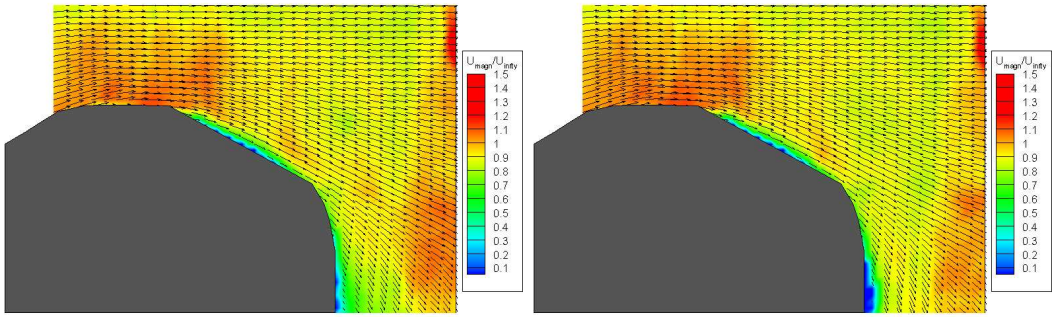

(c) Front Five Slots On

(d) Front Eleven Slots On

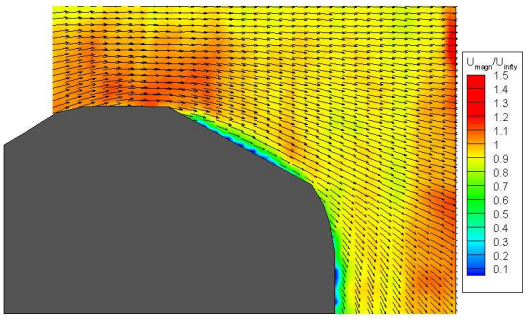

(e) All Slots On

Figure 3.2: Normalized mean velocity magnitude ($\langle\sqrt{\tilde{u}_1^2 + \tilde{u}_2^2}\rangle/U_\infty$) contours and mean velocity vectors of the flow field over the turret at a static angle of attack of 120° with various suction slot arrangements: no suction, back nine slots on, front five slots on, front 11 slots on, and all slots on.

For the rest of the static and dynamic pitching tests, solenoid valves were used to modulate the suction in an unsteady fashion. During the static and dynamic pitching flow control tests, all suctions slots were activated and ran simultaneously with the same control input, therefore producing unison actuation.

3.2.1 Various Static Elevation Angles with No Suction

In order to establish a dynamic pitch range, a series of measurements were taken at various static elevation angles at a zero azimuthal angle, without suction actuation. The change of the state of the flow over the turret as the elevation angle is increased can be seen in Figure 3.3. The normalized mean velocity magnitude ($\langle\sqrt{\tilde{u}_1^2 + \tilde{u}_2^2}\rangle/U_\infty$) for the range of pitch angles from 110° to 125° are shown in Figure 3.3. Each mean velocity panel was ensemble averaged over 1,000 instantaneous snapshots. At the shallow elevation angle of 110°, seen in Figure 3.3(a), the flow was fully attached to the aperture of the hemisphere. The flow remained attached to the aperture as the pitch angle was increased to 114° but when the angle was adjusted to 115° the flow reached its incipient point. The incipient point is defined by Anderson [3] as the point in which the flow state oscillates between attached and separated. At $\alpha = 115°$, both attached and separated flow states were seen over the aperture in the velocity measurements. Setting the elevation angle to a steeper setting of 116°, the flow above the aperture was fully separated and highly turbulent at all times. The presence of separation indicates an adverse pressure gradient developed over the aperture. As one would expect for the higher static pitch angles, 120°, 125°, and 130°, the flow was also completely separated over the aperture.

The second order moments such as the root mean square of the velocity, u_{rms}, and the Reynolds shear stress, $-\langle u_1 u_2\rangle$, give a more in-depth look into the flow. Figure

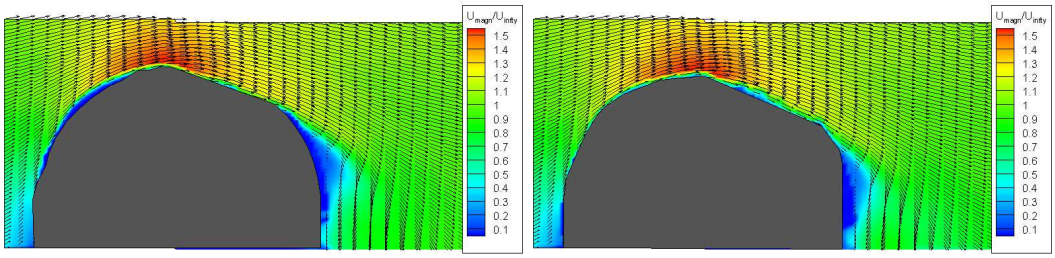

(a) 110° (b) 114°

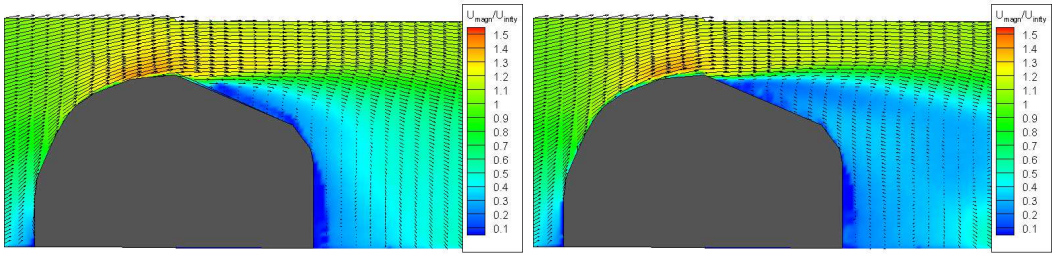

(c) 115° (d) 116°

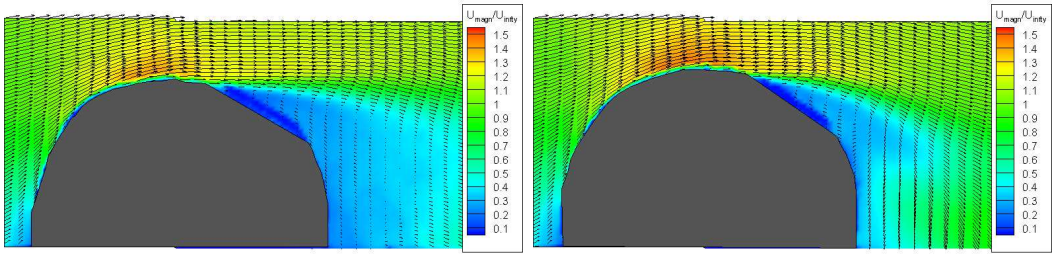

(e) 120° (f) 125°

Figure 3.3: Normalized mean velocity magnitude ($\langle\sqrt{\tilde{u}_1^2 + \tilde{u}_2^2}\rangle/U_\infty$) contours and mean velocity vectors of the flow field over the turret at various angles of attack with no suction.

3.4 shows the u_{rms} normalized by the freestream velocity U_∞, above the turret at $\alpha = 110°$ through $\alpha = 125°$ and is ensemble averaged over 1000 snapshots. The u_{rms} is defined in Equation 3.1,

$$u_{rms}(\vec{x}_i) = \sqrt{\frac{1}{N_{PIV}-1}(\sum_{i=1}^{N_{PIV}} \{[u_1(\vec{x}_i,t_0)]^2 + [u_2(\vec{x}_i,t_0)]^2\})} \quad i = 1,2 \tag{3.1}$$

N_{PIV} is the number of PIV snapshots, u_1 is the streamwise fluctuation velocity in the x direction, and u_2 is the cross-stream fluctuation velocity in the y direction. The u_{rms} represents the amount of deviation from the mean velocity, $U(\vec{x}_i)$. For the attached cases, the u_{rms} was low above the aperture but when the flow separated, the u_{rms} significantly increased. As the elevation angle increased, the area of high u_{rms} moved forward. For elevation angles from $\alpha = 110°$ through $\alpha = 125°$, the Reynolds shear stress, $-\langle u_1 u_2 \rangle$, normalized by the square of the freestream velocity, U_∞^2, is shown in Figure 3.5. The data presented in Figure 3.5 is ensemble averaged over 1000 snapshots. The $\frac{-\langle u_1 u_2 \rangle}{U_\infty^2}$ indicates the location of the transfer of momentum by the turbulence within the flow according to Tennekes and Lumley [75]. As the elevation was increased no discernable high shear stress area is seen until the flow separated. When the flow did separate, a high area of $\frac{-\langle u_1 u_2 \rangle}{U_\infty^2}$ first emerged behind the turret and moved forward as the angle was increased. At the separated pitch angles the $\frac{-\langle u_1 u_2 \rangle}{U_\infty^2}$ was intense throughout the wake. The peak level does seem to decrease as the angle is increased beyond $\alpha = 115°$, as seen in Figures 3.4(c) through 3.4(f). This suggests that the three dimensional effects may be stronger at the larger α and hence the wake appears to be more diffused at the higher elevation angles.

The spectrum of the pressure sensor at the center of the aperture (Sensor No. 21) also shows the influence of the elevation angle increase. Although the flow is highly three dimensional, Sensor No. 21 was chosen as an indicator of the state of the flow

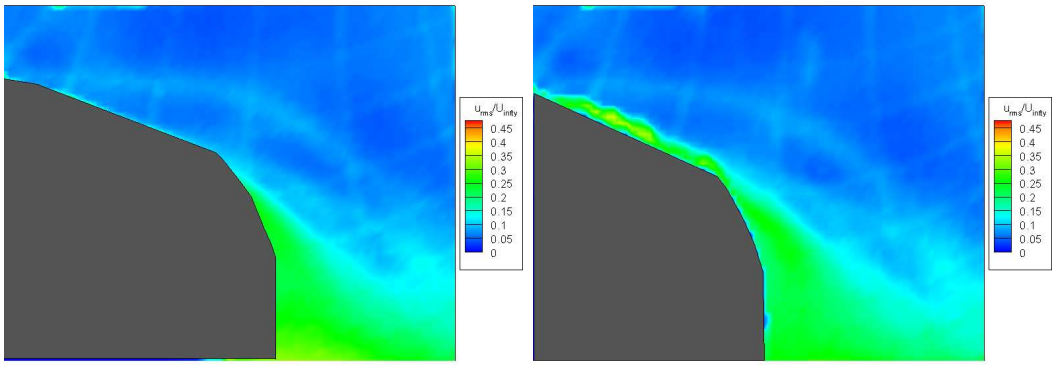

(a) 110°

(b) 114°

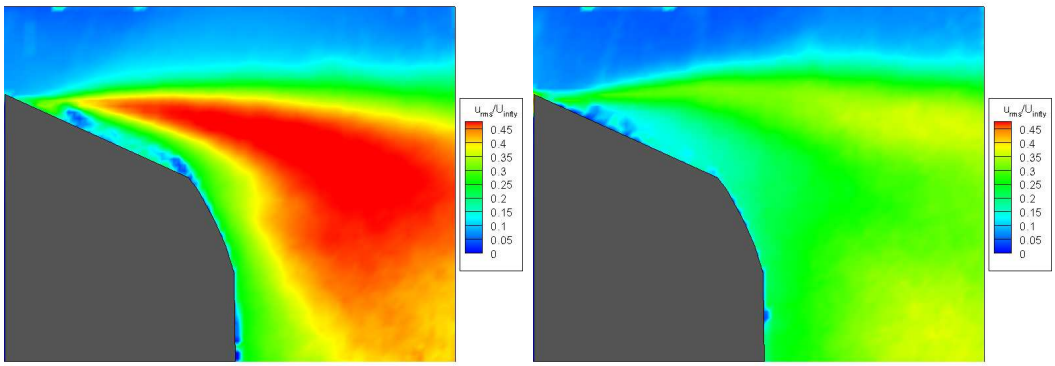

(c) 115°

(d) 116°

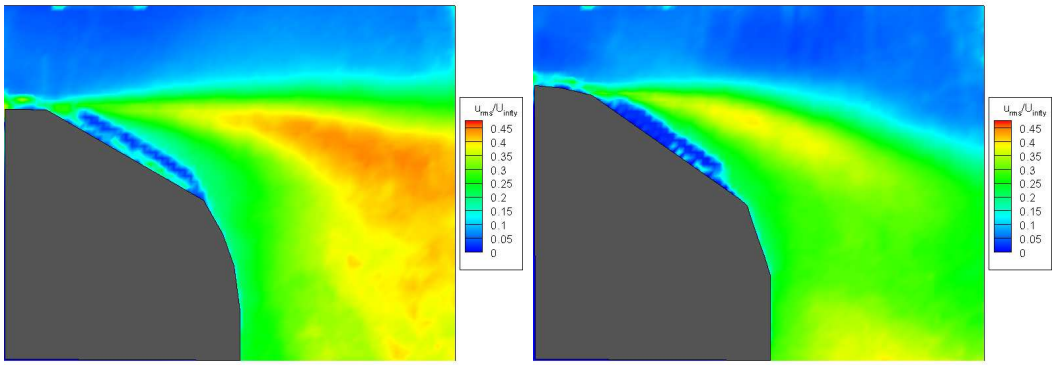

(e) 120°

(f) 125°

Figure 3.4: u_{rms}/U_∞ contours of the flow field over the turret at various angles of attack with no suction.

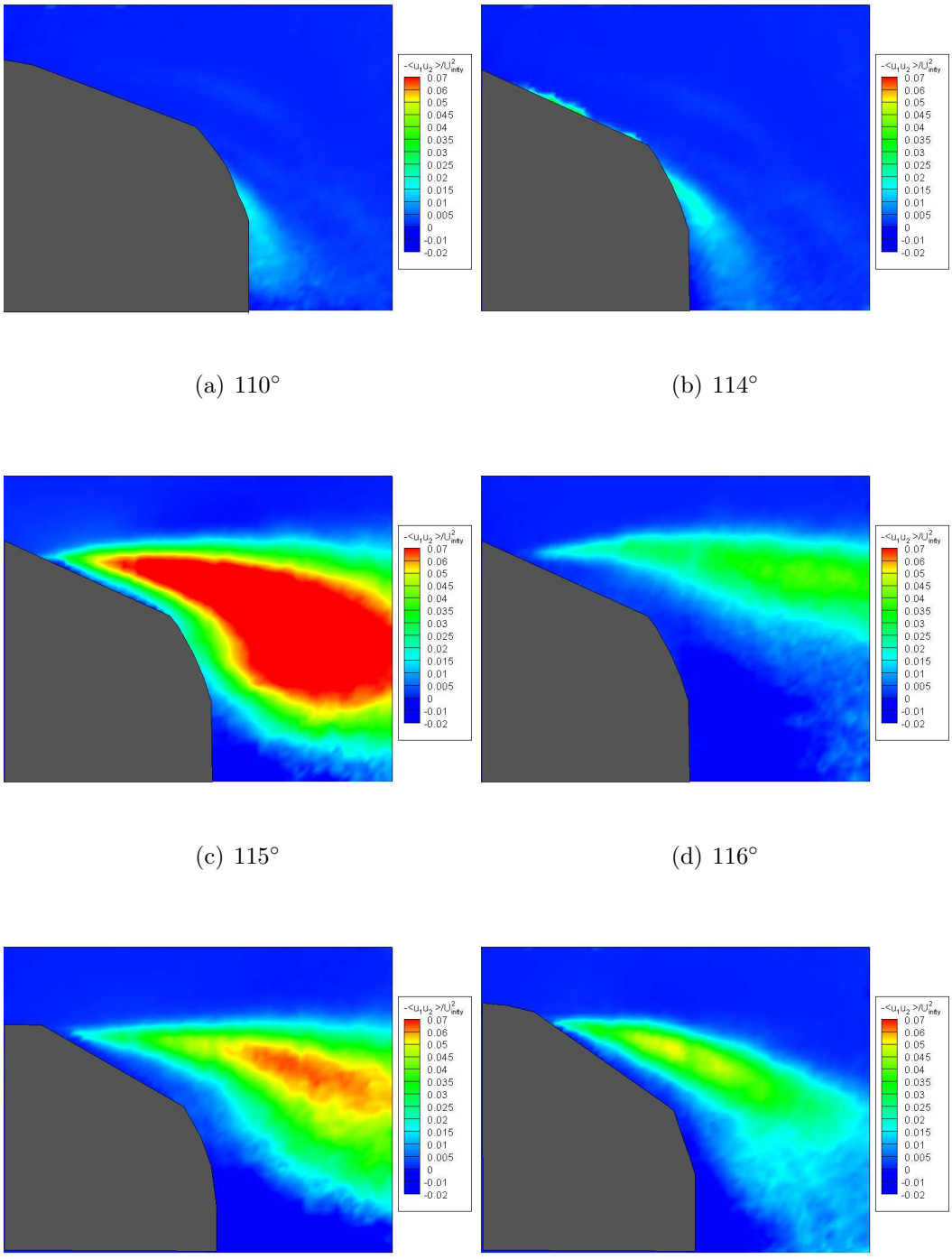

(a) 110°

(b) 114°

(c) 115°

(d) 116°

(e) 120°

(f) 125°

Figure 3.5: $-\langle u_1 u_2 \rangle / U_\infty^2$ contours of the flow field over the turret at various angles of attack with no suction.

over the aperture. The spectra for each angle in Figure 3.6(b) was averaged over 500

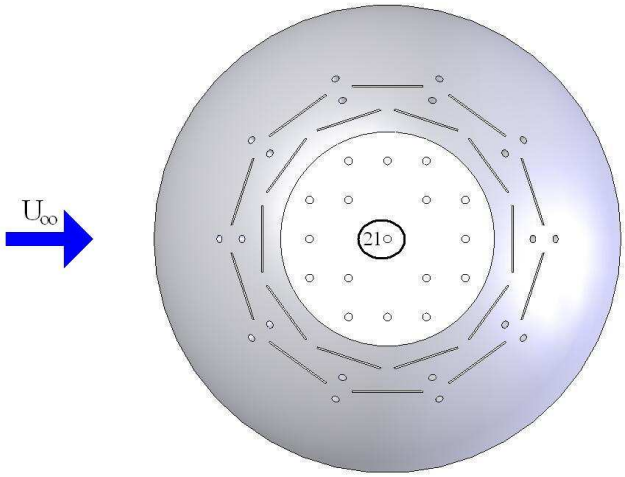

(a) Sensor Location

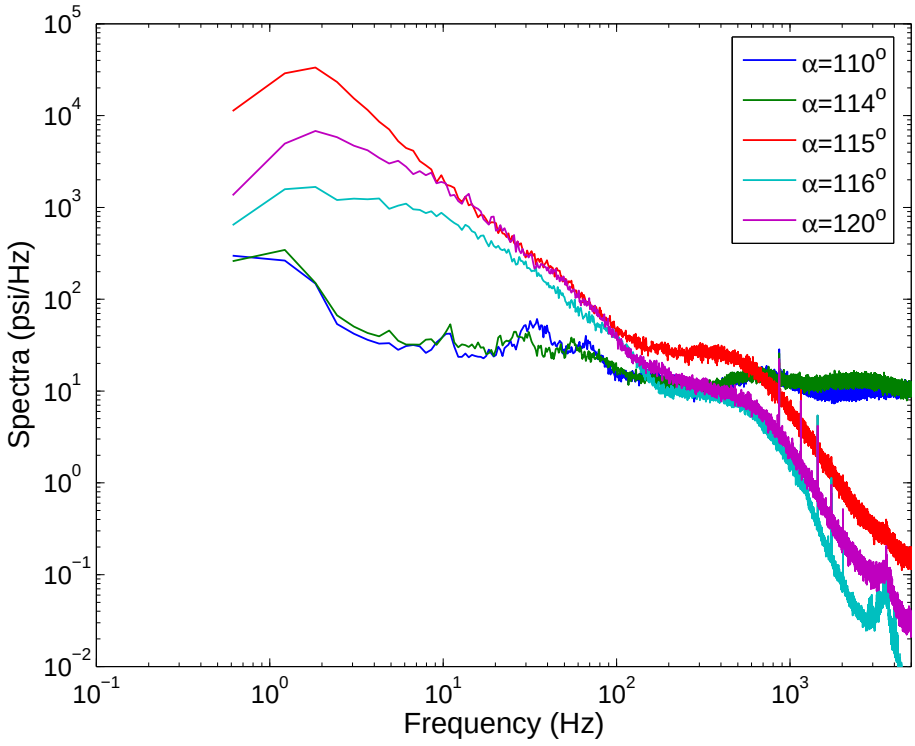

(b) Spectra

Figure 3.6: Spectrum of the center aperture pressure sensor (Sensor No. 21) at $\alpha = 110°$ to $120°$.

blocks of 2048 sample points and computed with Equation 3.2.

$$S(\omega)\delta(\omega - \omega') = \langle \hat{p}(\omega)\hat{p}^*(\omega') \rangle \tag{3.2}$$

The ω is the angular frequency, $\hat{}$ is the Fourier operator, * is the complex conjugate of the signal, and $\langle\rangle$ is the ensemble average of the pressure time series. The Fourier transform of the pressure time series is defined in Equation 3.3,

$$\hat{p}(\omega) = \frac{1}{2\pi} \int_{-\infty}^{\infty} e^{i\omega t} p(t) dt \tag{3.3}$$

where $p(t)$ is the pressure time series and $\hat{p}(\omega)$ is the Fourier transformed pressure signal. At the lower pitch angles of $\alpha = 110^\circ$ and 114° the flow is attached to the aperture which gives a relatively flat frequency response. When the flow separates over the aperture, the spectrum shows a dramatic increase in the lower frequencies as compared to the attached cases. This implies that there was an increase in amount of large scale structures over the aperture as the elevation angle increased. Above $400Hz$ there is a sharp roll off that corresponds to a decrease in small structures within the flow. Sharp, distinct peaks occur in the range from 800Hz to 2000Hz and correspond to small structures within the wake.

Figure 3.7 shows the separation height of the wake. The separation height is marked where the flow is less than 99% of the freestream velocity. As the pitch angle is increased the wake sized is increased until $\alpha = 120^\circ$ where the height decreases. This decrease is most likely due to three dimensional effects washing out the velocity in the field of view of the measurements.

This series of tests provided the range of motion for dynamic pitching. The desired dynamic pitch range was one which the flow state over the aperture goes from attached

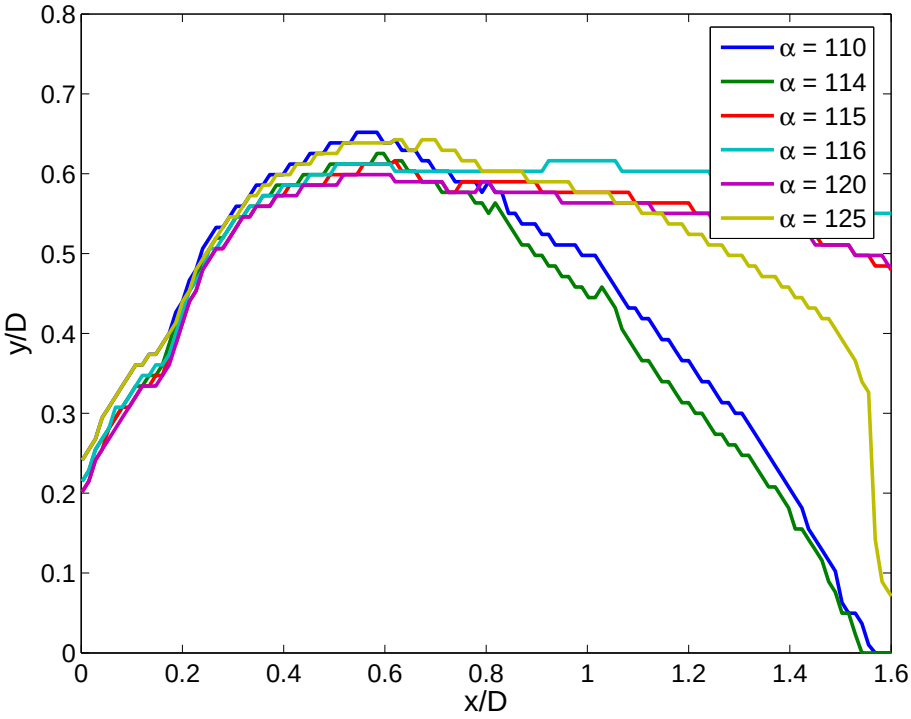

Figure 3.7: Separation height of the flow around the turret at various fixed angles.

to separated back to attached flow. Therefore using the static pitching baseline tests the dynamic pitch range cycle was set to 110° to 120° and back to 110°.

3.2.2 Various Static Elevation Angles with Steady Suction

Using the relationship between the duty cycle and average coefficient of momentum seen in Figure 2.5, several open loop, unsteady suction modulation cases over a range of various set duty cycles were investigated for a series of static pitch angles. The range of static angles was from 110° to 130° at 5° intervals and the range of duty cycles was from 30% to 90% at 20% intervals. The corresponding coefficient of momentum, defined in Equation 2.3, for each open loop control duty cycle case is shown in Table 3.2. The steady suction control at the elevation angles in which the flow over the

Duty Cycle	C_μ
30%	12.32×10^{-4}
50%	17.50×10^{-4}
70%	27.24×10^{-4}
90%	33.94×10^{-4}

Table 3.2: Coefficient of momentum for duty cycle cases.

aperture was separated effectively reduced the turbulence levels and delayed the onset of separation over the aperture.

Of particular interest is the effectiveness of the unsteady suction modulation at the pitch angle of 120°, since this angle represents the maximum dynamic pitch angle. Figure 3.8 shows the mean velocity comparison between no control and the duty cycle modulation range of 30%, 50%, 70%, and 90% at 120° elevation angle. The mean velocity magnitude for each control case is ensemble averaged over 1,000 instantaneous velocity snapshots. Duty cycle actuation at 30% and 50% had little effect, only slightly reducing size of the wake. A greater amount of wake reduction was seen with the

suction of 70% and 90% duty cycle. At the higher duty cycle suction actuation, the control input was able to keep the flow attached to the aperture. Examination of the u_{rms} at $\alpha = 120°$ over the range of suction actuation is seen in Figure 3.9. In the wake of the turret, the u_{rms} was reduced even with just 30% duty cycle. The greater the suction the further reduction of the u_{rms} was seen in the panels of Figure 3.9. Focusing in on the area above the aperture, a high amount of u_{rms} persisted until the 70% duty cycle case, as seen in Figure 3.9(d). A significant amount of suction was required to decrease the velocity fluctuation directly over the aperture. Seen in Figure 3.10(b), the 30% duty cycle case shifted the location of the intense $\frac{-\langle u_1 u_2 \rangle}{U_\infty^2}$ closer to the aperture as well as reducing the thickness. The 50% duty cycle case saw an even thinner area of high $\frac{-\langle u_1 u_2 \rangle}{U_\infty^2}$ above the aperture. Both Figures 3.10(d) and 3.10(e) show small levels of $\frac{-\langle u_1 u_2 \rangle}{U_\infty^2}$, again indicating a reduction of the fluctuating velocities. The u_{rms} and $\frac{-\langle u_1 u_2 \rangle}{U_\infty^2}$ are ensemble averaged over 1,000 velocity snapshots for each case.

As the suction is increased the size of the wake is decreased as seen in Figure 3.11. The separation height is marked where the flow is less than 99% of the freestream velocity.

The change in the flow also can be seen in the frequency domain of Sensor 21, in Figure 3.12. The spectrum is averaged over 500 blocks containing 2048 data points each. The open-loop cases of 30% and 50%, the spectra fall closely upon each other, especially for the frequencies above 10Hz. Comparing the baseline cases to the 30% and 50% cases, a broad band shift occurred at the lower frequencies. This corresponds to a change in the large scale structures within the flow. For these open loop cases, a large peak occur at $10Hz$ is related to the control input. This peak represents a large scale structure due to the unsteady actuation. At the higher duty cycle cases of 70% and 90% the frequency response was flat across the frequency domain indicating

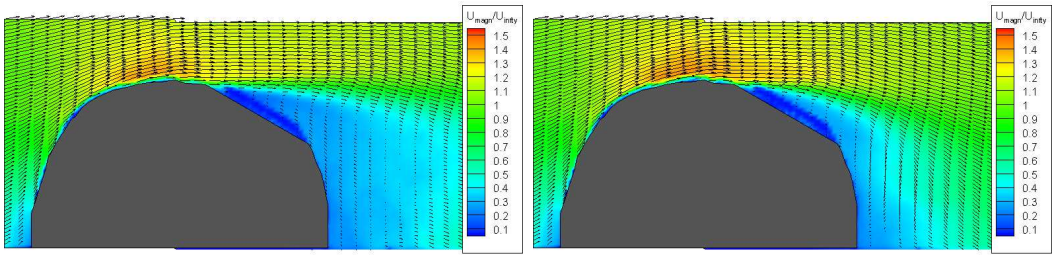

(a) No Suction

(b) 30% Duty Cycle

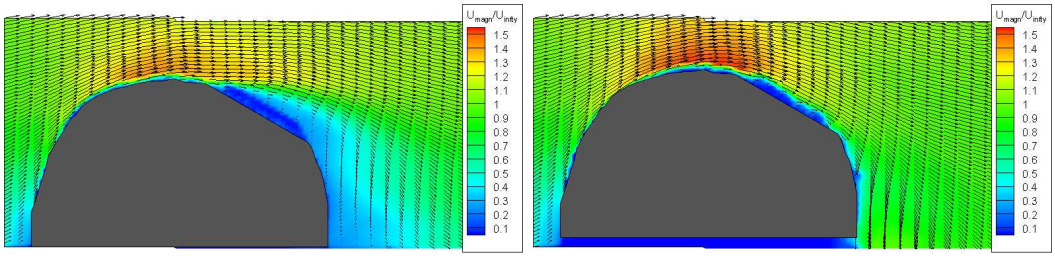

(c) 50% Duty Cycle

(d) 70% Duty Cycle

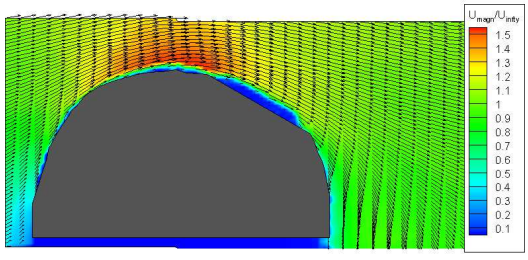

(e) 90% Duty Cycle

Figure 3.8: Normalized mean velocity magnitude ($\langle\sqrt{\tilde{u}_1^2 + \tilde{u}_2^2}\rangle/U_\infty$) contours and mean velocity vectors of the flow field over the turret at a static angle of attack of 120° with various unsteady suction slot actuation: no suction, 30%, 50%, 70%, and 90% duty cycle modulation.

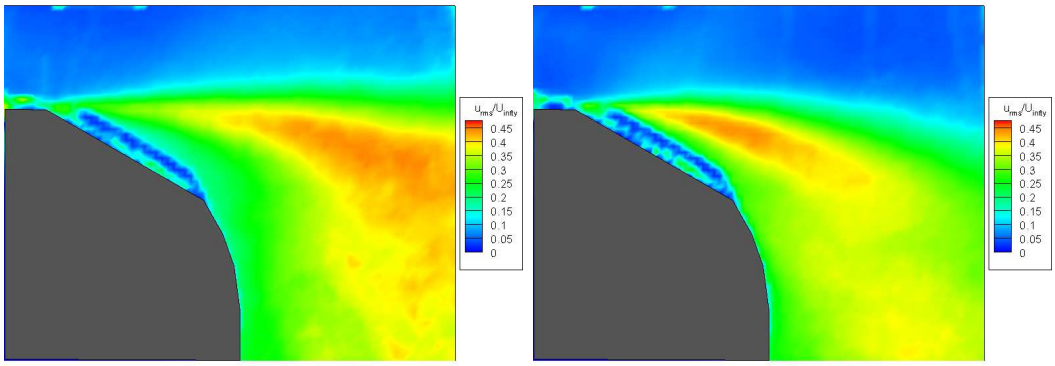

(a) $DC = 0$ (b) $DC = 30$

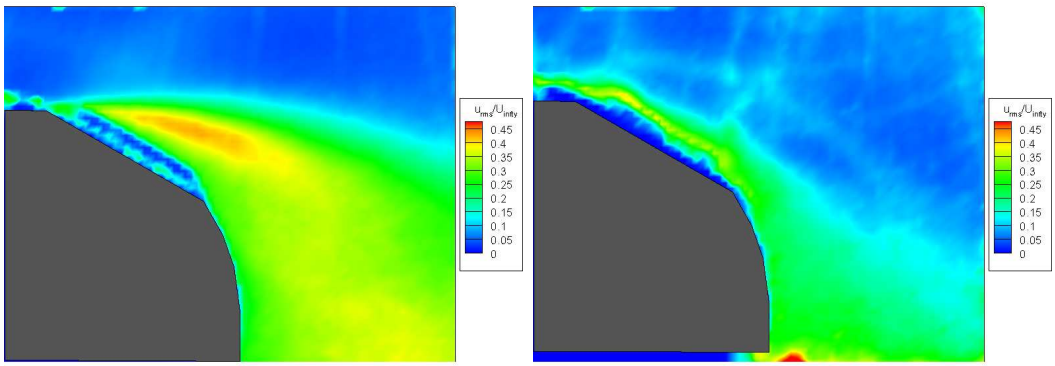

(c) $DC = 50$ (d) $DC = 70$

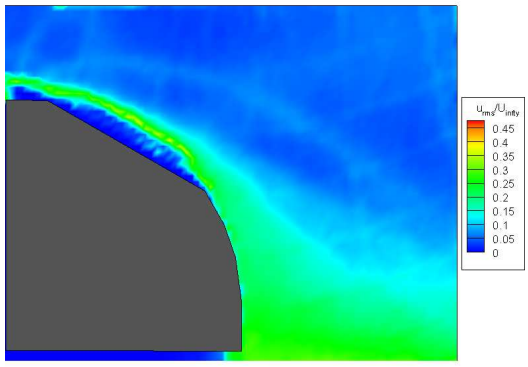

(e) $DC = 90$

Figure 3.9: u_{rms}/U_∞ contours of the flow field over the turret at 120° with unsteady suction modulation.

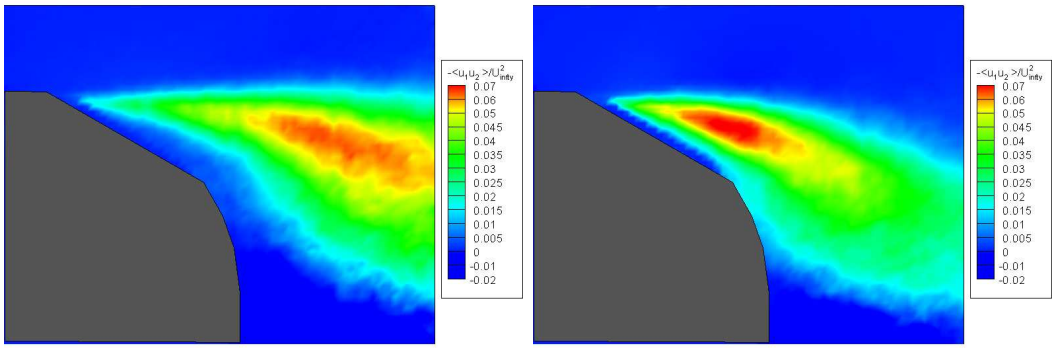

(a) $DC = 0$ (b) $DC = 30$

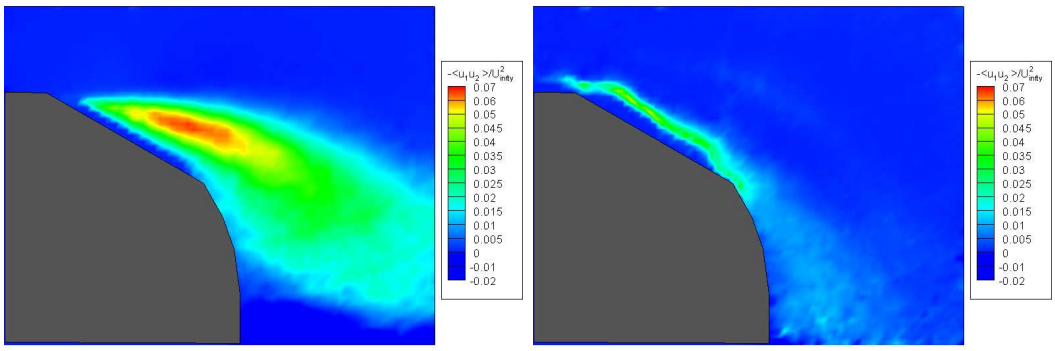

(c) $DC = 50$ (d) $DC = 70$

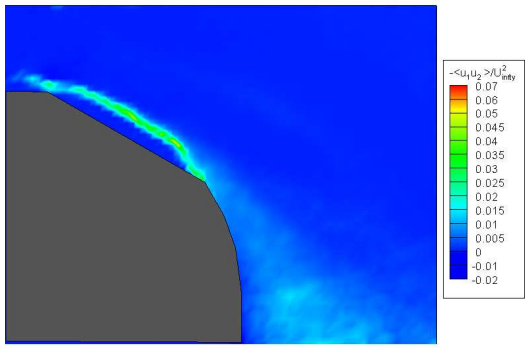

(e) $DC = 90$

Figure 3.10: $-\langle u_1 u_2 \rangle / U_\infty^2$ contours of the flow field over the turret at 120° with suction.

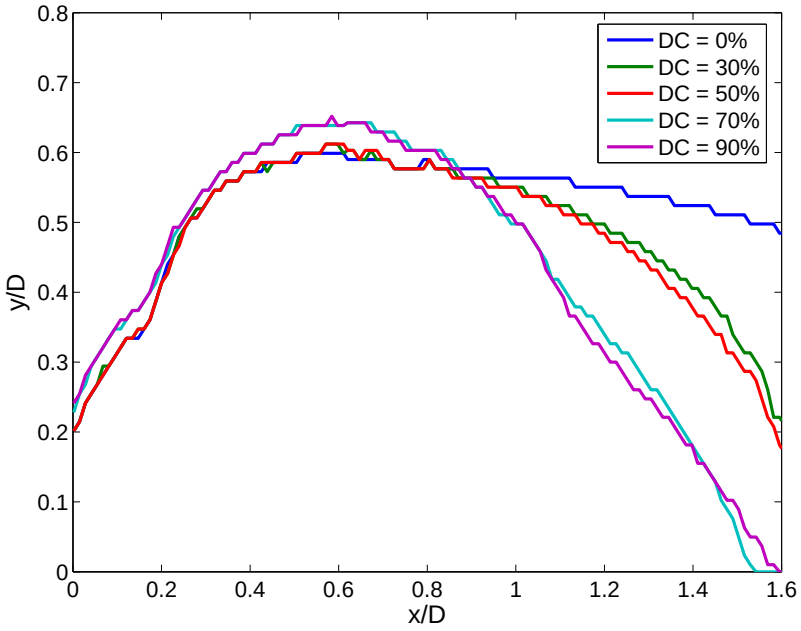

Figure 3.11: Separation height of the flow around the turret at $\alpha = 120°$ for various duty cycle cases.

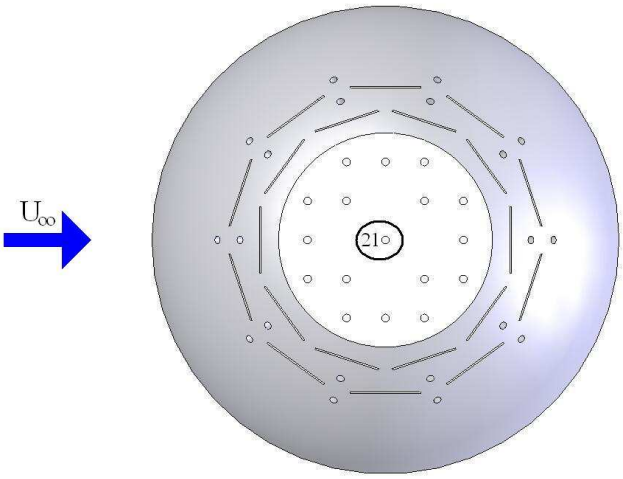

(a) Sensor Location

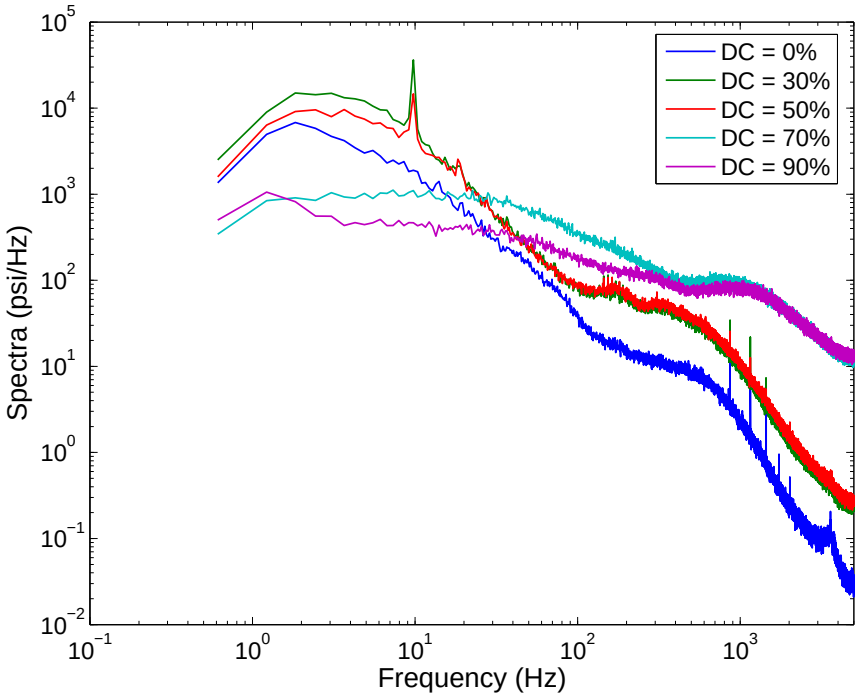

(b) Spectra

Figure 3.12: Spectrum of the center aperture pressure sensor (Sensor No. 21) for $\alpha = 120°$ for various unsteady suction duty cycle cases.

that the flow was attached. The sharp peak seen at 10Hz is no longer seen in the frequency response for the 70% and 90% duty cycle cases.

This set of experiments demonstrated that an increase of the elevation angle, α, required more suction to keep the flow attached to the aperture. There also seems to be an optimum actuation that exists between 50% to 70% duty cycle, within this range the flow stays attached to the aperture. Increasing the duty cycle beyond this optimum point achieved only moderate reductions in u_{rms}.

Increasing the elevation also shifted the location of the shear layer over the aperture. In a study performed by Andino [6] on a similar turret configuration using synthetic jet actuators, a comparable reduction in the u_{rms} and $\frac{-\langle u_1 u_2 \rangle}{U_\infty^2}$ was observed over the aperture. The possible organization of the flow due to the open loop unsteady suction, also observed by Andino [6], would improve the performance an adaptive optics system.

3.3 Dynamically Pitching Turret

The next series of the tests examined the role in which a dynamically pitching turret affects the flow over the aperture.

The hemisphere of the turret was pitched dynamically in a sinusoidal matter using the following prescribed function:

$$\alpha(t) = \left[115 - 5\cos(\frac{\omega}{\pi}t)\right] \tag{3.4}$$

where $\omega = 2.4$ deg/s. The pitch rate was provided by the Air Force. The non-

dimensional rotation rate is $\varpi = 0.00192$ based on Equation 4.2.

$$\varpi = \frac{\omega D}{360^{\circ} U_{\infty}} \tag{3.5}$$

The non-dimensional rotation rate is a function of turret diameter D, rotation rate ω, freestream velocity U_{∞}, and maximum rotation range. One dynamic pitch run consisted of three pitch cycles where, one pitch cycle had a period of $8\frac{1}{3}$ seconds. The desired pitch range was one in which the flow over the aperture would be initial attached, then separated, and finally reattached. This range was established in the previous section (Section 3.2.1). The pitch range was set to be from 110° to 120° then back to 110°. Due to the intensive time to collect the data and data storage requirements, data was collected for 102 pitch cycles. Although more pitch cycle would be ideal, 102 pitch cycles is adequate for this test to obtain reasonable averages.

3.3.1 Dynamic Pitching Turret without Suction

As the hemisphere rotated through its pitch cycle, flow over the aperture went from being attached to separated back to attached, as seen in Figure 3.13.

Figure 3.13 shows the mean velocity magnitude contours at five elevation angles: 110°, 115° pitching backward, 120°, 115° pitching forward, and 110°. The mean velocity magnitude, u_{rms}, and $\frac{-\langle u_1 u_2 \rangle}{U_{\infty}^2}$ at each angle are phase averaged over 102 pitch cycles. The static case at $\alpha = 115^{\circ}$, Figure 3.3(b), the flow is separated and highly turbulent, while in the dynamic pitch case at the backwards pitching angle of $\alpha = 115^{\circ}$, Figure 3.13(b), the flow is attached to the aperture. This difference in the flow state between the two cases reveals that the dynamic pitching delayed the onset of separation and the formation of an adverse pressure gradient. Also comparing the backward pitching angle at $\alpha = 115^{\circ}$, Figure 3.13(b), and the forward

pitching angle at $\alpha = 115°$, Figure 3.13(d), the flow indicates the presence of a strong hysteresis. In fact, separation over the aperture occurred at an elevation angle of 118° while the hemisphere pitched backwards and when the hemisphere pitched forward reattachment happens at an elevation equal to 112°. Separation occurred at the leading edge of the aperture. The dynamic pitching cases shows that rotation delays the increase of the adverse pressure gradient above the aperture. This delay in the adverse pressure gradient also delays the separation from 115° to 118°.

Rotation of the hemisphere caused the location of the peak u_{rms} over the aperture to shift when compared to the static pitch cases. The peak u_{rms} initially starts out close to the aperture but as the hemisphere pitches dynamically backwards the u_{rms} area thickens until an angle of 120°. When the hemisphere rotates forward dynamically the peak u_{rms} thins and moves vertically off the aperture. The $\frac{-\langle u_1 u_2 \rangle}{U_\infty^2}$ had a similar trend as the u_{rms} through the pitch cycle. For the first half of the cycle, the $\frac{-\langle u_1 u_2 \rangle}{U_\infty^2}$ was close to the aperture until an elevation angle of 120°. Dynamically pitching forward, the intense area of $\frac{-\langle u_1 u_2 \rangle}{U_\infty^2}$ lifted off of the aperture. This indicates that the shear layer is on the aperture while the hemisphere is pitching forward and when the hemisphere pitches back to 110° the shear layer lifts off the aperture vertically.

The flow over the aperture demonstrated characteristics of dynamic stall over an airfoil even though the turret flow is three dimensional. Dynamic stall is characterized by McCroskey et al. [47] as a "shedding of a strong vortex-like disturbance from the leading-edge region" that distorts the pressure distribution and produces "transient forces and moments that are fundamentally different from their static-stall counterparts". The presence of dynamic stall characteristics can be seen in the fluctuating, surface pressure distribution at the centerline of the turret, shown in Figure 3.16(b). The amplitude of the fluctuating surface pressure of the furthest leading pressure sen-

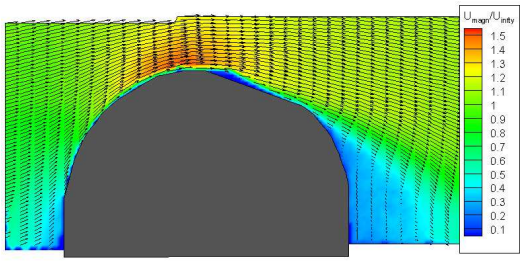

(a) $\alpha = 110°$, Start of Cycle

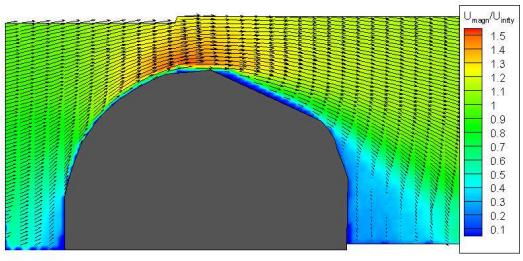

(b) $\alpha = 115°$ Pitching Backwards

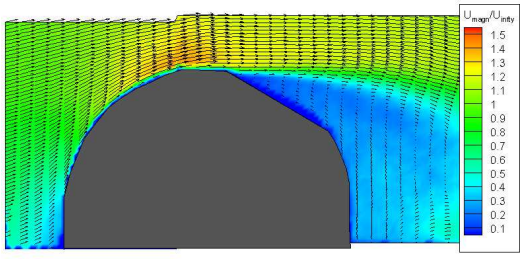

(c) $\alpha = 120°$

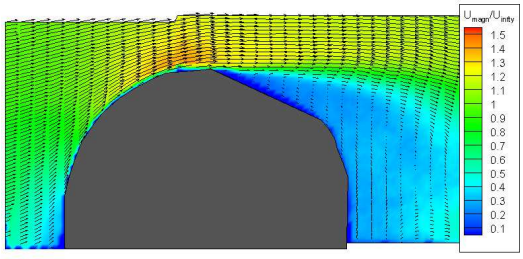

(d) $\alpha = 115°$ Pitching Forwards

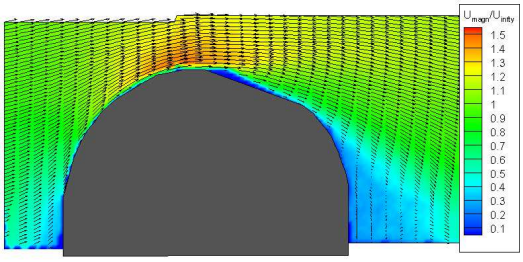

(e) $\alpha = 110°$, End of Cycle

Figure 3.13: Normalized mean velocity magnitude ($\langle\sqrt{\tilde{u}_1^2 + \tilde{u}_2^2}\rangle/U_\infty$) contours and mean velocity vectors of baseline pitching turret.

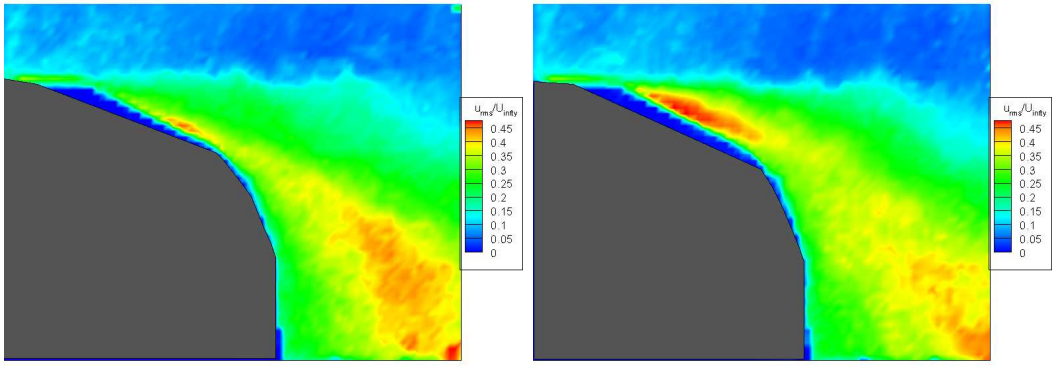

(a) $\alpha = 110°$, Start of Cycle

(b) $\alpha = 115°$ Pitching Backwards

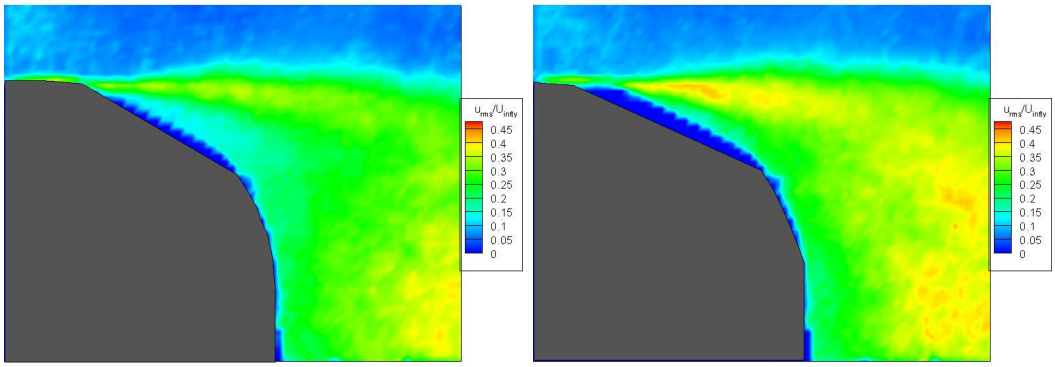

(c) $\alpha = 120°$

(d) $\alpha = 115°$ Pitching Forwards

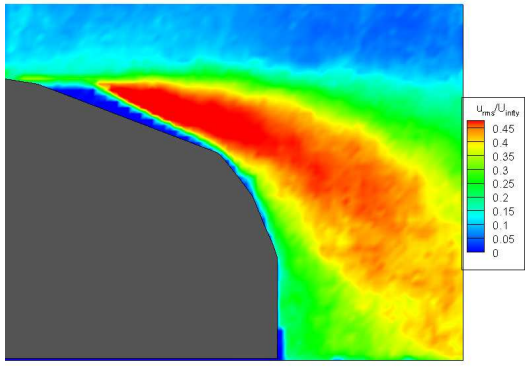

(e) $\alpha = 110°$, End of Cycle

Figure 3.14: u_{rms}/U_∞ contours of baseline pitching turret.

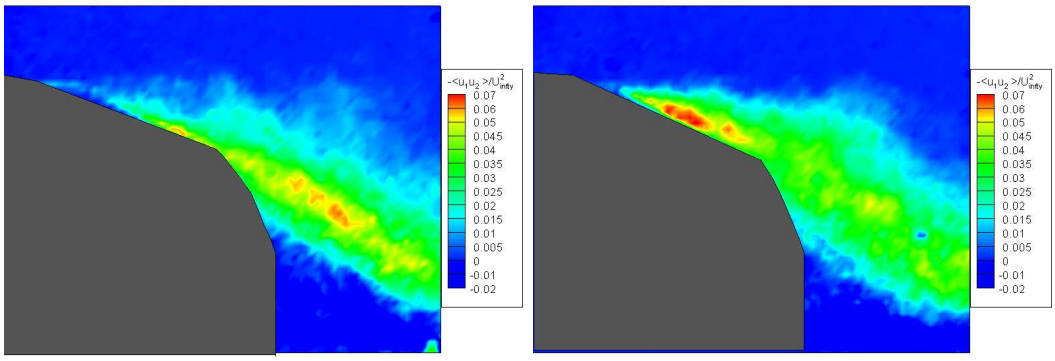

(a) $\alpha = 110°$, Start of Cycle

(b) $\alpha = 115°$ Pitching Backwards

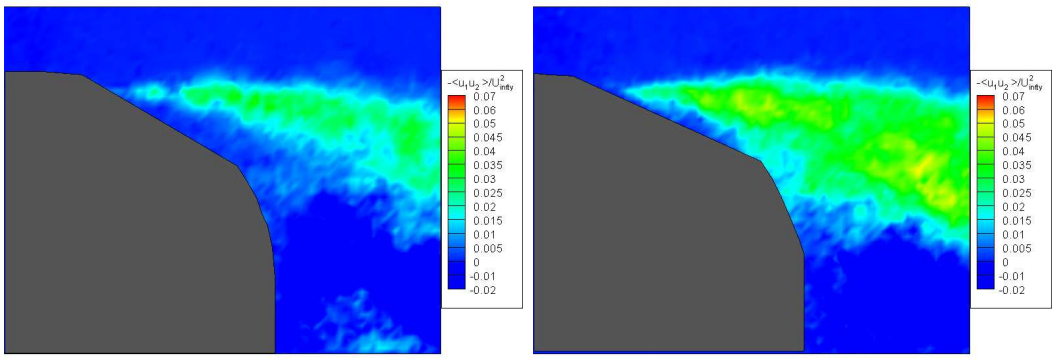

(c) $\alpha = 120°$

(d) $\alpha = 115°$ Pitching Forwards

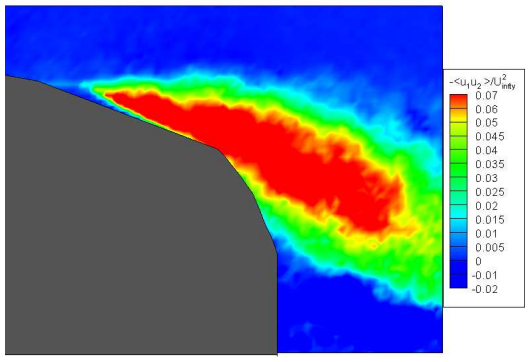

(e) $\alpha = 110°$, End of Cycle

Figure 3.15: $-\langle u_1 u_2\rangle/U_\infty^2$ contours of baseline pitching turret.

sor, Sensor No. 1 seen in the top panel of Figure 3.16(b), increases as the hemisphere pitches back and decreases when pitching forward. This pressure trend correlates well to the pitch angle. Downstream of the leading pressure sensor, the pressure time series of Sensors No's 7, 14, 21, and 28 exhibit the opposite trend of Sensor No. 1, as seen in the bottom panels of Figure 3.16(b). For Sensors 7, 14, 21, and 28 the amplitude of the fluctuating surface pressure decrease as the flow becomes separated and the intense area of the u_{rms} lifts off the aperture. When the

On the aperture, the small surface pressure amplitude corresponds to when the flow is separated and the increased amplitude corresponds to attached flow. Looking at both the u_{rms} in Figure 3.14 and the fluctuating surface pressure in Figure 3.16(b), the decrease in the surface pressure amplitude corresponds to the shift of the intense u_{rms} area off of the aperture. The increase in the surface pressure amplitude corresponds to the location of the intense u_{rms} area being directly over the aperture.

The fluctuating surface pressure at the centerline was transformed into frequency space, seen in Figure 3.16(c). The pressure spectrum is ensemble averaged over 500 blocks of 2048 sample points. A change in the spectrum occurs from ahead of the aperture to on the aperture. The narrow band of frequency peaks from 900Hz to 1500Hz, seen in Sensor 1, is shifted into a broad band of frequencies in Sensors 14, 21, and 28. This indicates that the flow over the aperture contains an increased range of small scale structure sizes. In the low frequency range, a jump in the amplitude of the spectra occurs from Sensor 1 to Sensor 14. The increased amplitude corresponds to a sharp increase in the number of large scaled structures within the flow over the aperture. As the flow convects downstream over the aperture, it can be seen in Figure 3.16(c) that the amplitude of the spectrum in the frequency range below 100Hz decreases. This shift in the amplitude implies there is a decrease in the number of large scaled structures. In the higher frequency range, the sensors over the aperture

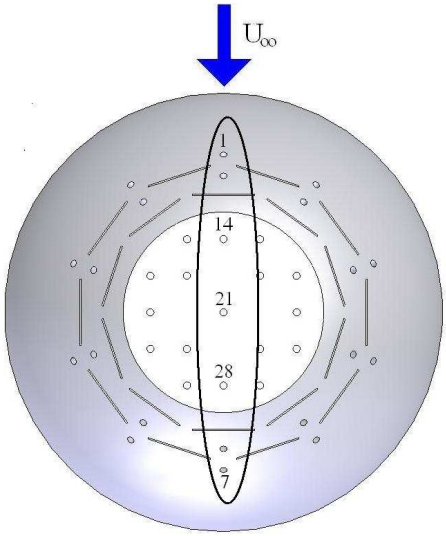

(a) Sensor Location

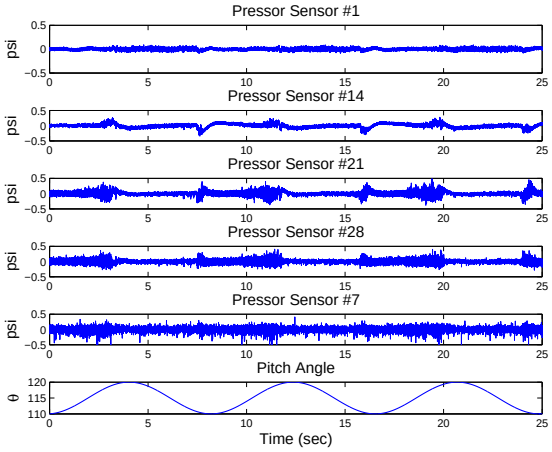

(b) pressure time series

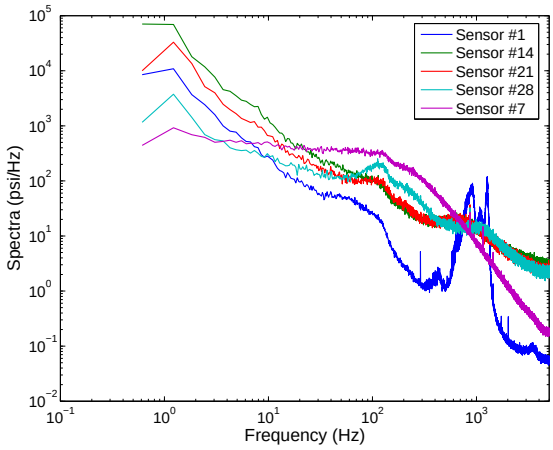

(c) Spectra

Figure 3.16: The centerline fluctuating surface pressure in time and frequency space with no control. The freestream flow is from top of the page to the bottom.

(Sensors 14, 21, and 28), a small peak existed at the 100Hz. This peak represented a shedding frequency coming off the aperture. Sensor 7 indicates that the flow is continuously separated throughout the pitch cycle.

Due to the highly three dimensional nature of the flow over the turret, the flow was not homogeneous over the aperture. Figure 3.17 shows the spectrum for the leading edge of the aperture (Sensors 13, 14, and 15) in the top panel, the middle of the aperture (Sensors 20, 21, and 22) in the middle panel, and the trailing edge of the aperture (Sensors 27, 28, and 29) in the bottom panel. The spectrum was similar for the low frequencies up to 100Hz. The large structures exist uniformly across the aperture while the small structures are not uniform. At the leading edge sensors the peaks around 1000Hz seen at the center of the turret were not seen in the off center sensors. These structures represented by the sharp peak are only at the center of turret. In all the sensors a small peak at 100Hz exist which implies that an associated structure sheds over the entire aperture. Sensor 22 the flow seems to be completely separated through out the pitch cycle.

These results show that even at the modest pitch rate of $2.4\frac{deg}{sec}$ the flow was significantly influenced by the motion of the turret.

3.3.2 Open loop Control via Unsteady Suction Modulation for a Dynamically Pitching Turret

Multiple unsteady suction modulation cases were examined over duty cycle modulations of 30%, 50%, 70%, and 90% with an underlying constant driving frequency of $25Hz$. Open-loop control cases were studied to determine the effectiveness of the suction actuation as the hemisphere rotated through its pitch cycle. The suction was activated prior to each run to obtain a steady state in the flow before the pitching

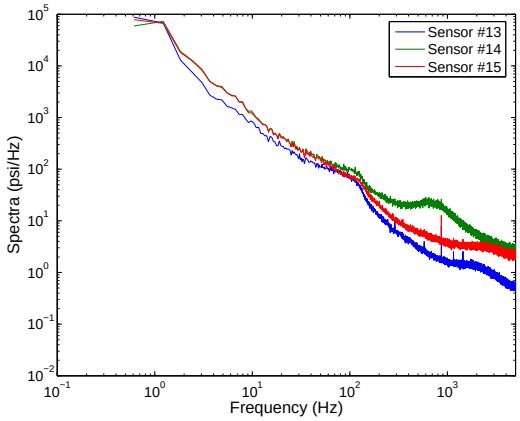

(a) Front Sensors

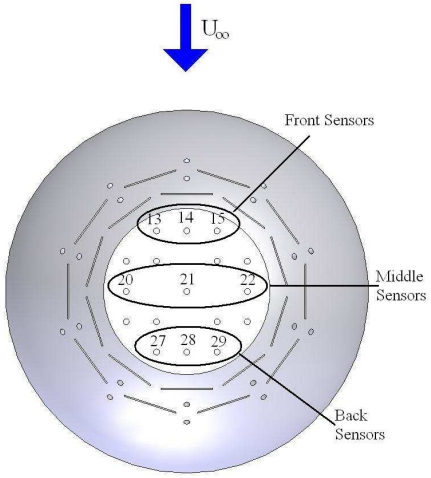

(b) Sensor Location

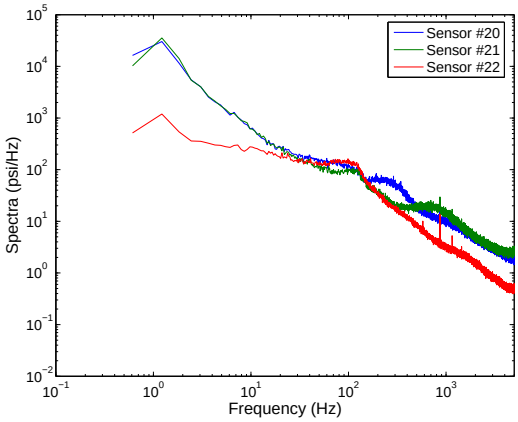

(c) Middle Sensors

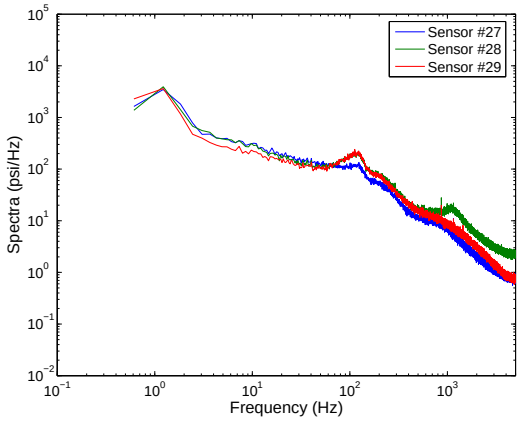

(d) Back Sensors

Figure 3.17: Spectrum of the off center fluctuating surface pressure with no control. The freestream flow is from top of the page to the bottom.

commenced.

Similarly to the static pitch cases (Section 3.2.2), the open loop suction control for the dynamically pitching turret had enough control authority to be able to delay massive separation of the flow over the aperture throughout the pitch cycle of the hemisphere. Shown in Figure 3.18 is mean velocity magnitude of the maximum open loop control case of 90% duty cycle. Throughout the pitch cycle, the flow seems to have remained attached to the aperture. Comparison of Figure 3.13 and Figure 3.18 shows a significant reduction in the size of wake over the aperture as the hemisphere rotated through its pitch cycle. While the hemisphere was rotating back, the location of the peak u_{rms} was shifted behind the turret, as shown in Figure 3.19. When the aperture reached an elevation angle of 120° the peak u_{rms} area moved over the aperture and remain over the aperture while the hemisphere pitched forward. Although the flow is attached through the pitch cycle, a persistent high area of $\frac{-\langle u_1 u_2 \rangle}{U_\infty^2}$ can be seen over the aperture in Figure 3.20. Suction was able to prevent the flow from massively separating but a shear layer did persist over the aperture.

The open loop control also had a clear effect upon the fluctuating surface pressure. For example Figure 3.21(b) shows the centerline, fluctuating surface pressure time series for the 90% duty cycle case. The suction actuation caused an increase in the pressure amplitude for Sensors 14, 21, and 28 as compared to the baseline case. When the flow separates a significant increase in the pressure fluctuations occur, this indicating that the separation over the aperture is being lessened. This reduction in the adverse pressure gradient leads to a delay in separation over the aperture. The spectrum of the centerline surface pressure is seen in Figure 3.21(c) corresponding to the pressure time series in Figure 3.21(b). In the low frequency ranges, the spectra for the pressure over the aperture was slightly shifted to higher frequencies resulting in a more broad band frequency response, as compared to the baseline case. The broad

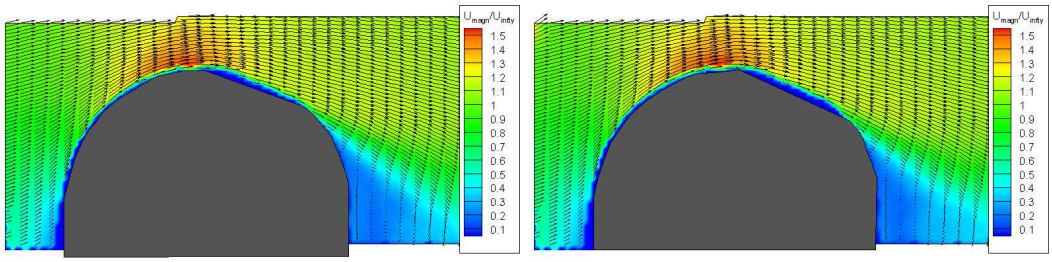

(a) $\alpha = 110°$, Start of Cycle

(b) $\alpha = 115°$, Pitching Backwards

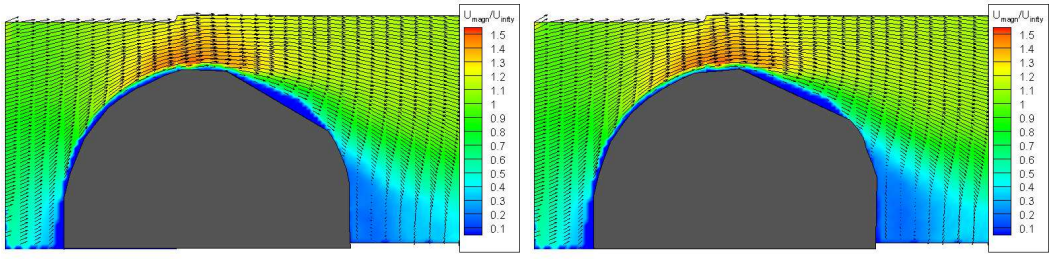

(c) $\alpha = 120°$

(d) $\alpha = 115°$, Pitching Forwards

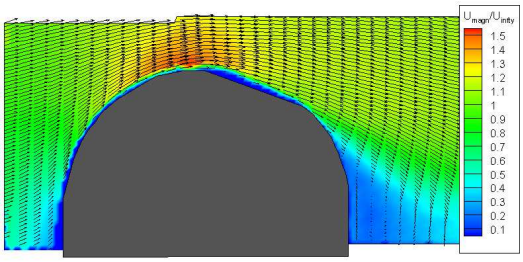

(e) $\alpha = 110°$, End of Cycle

Figure 3.18: Normalized mean velocity magnitude ($\langle\sqrt{\tilde{u}_1^2 + \tilde{u}_2^2}\rangle/U_\infty$) contours and mean vectors of a open loop control at 90% duty cycle.

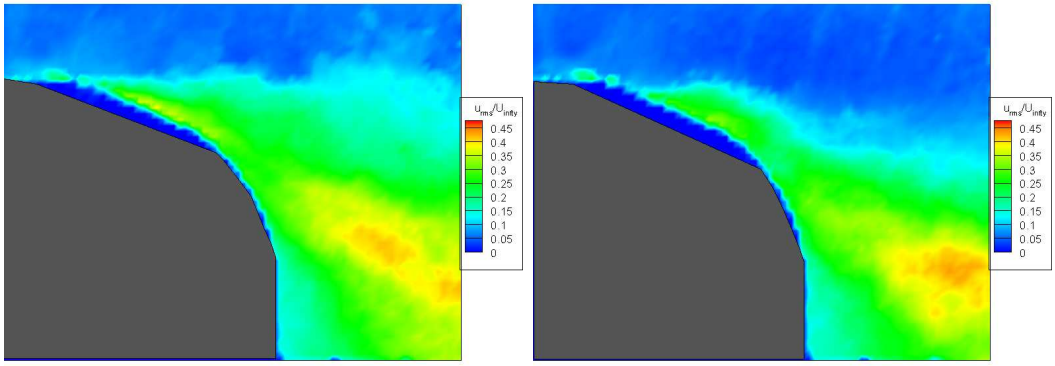

(a) $\alpha = 110°$, Start of Cycle

(b) $\alpha = 115°$, Pitching Backwards

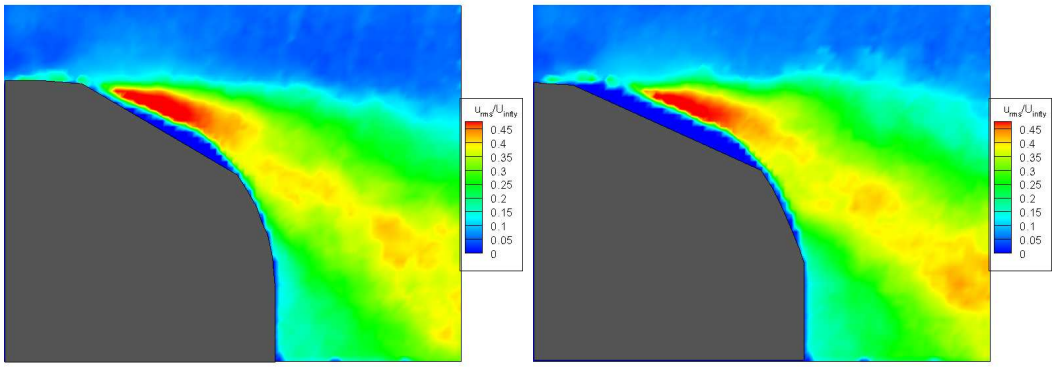

(c) $\alpha = 120°$

(d) $\alpha = 115°$, Pitching Forwards

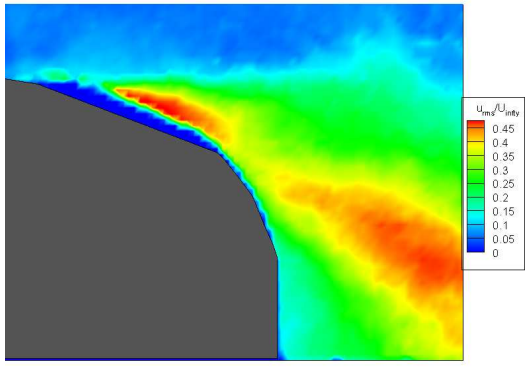

(e) $\alpha = 110°$, End of Cycle

Figure 3.19: u_{rms}/U_∞ contours of DC of 90% pitching turret.

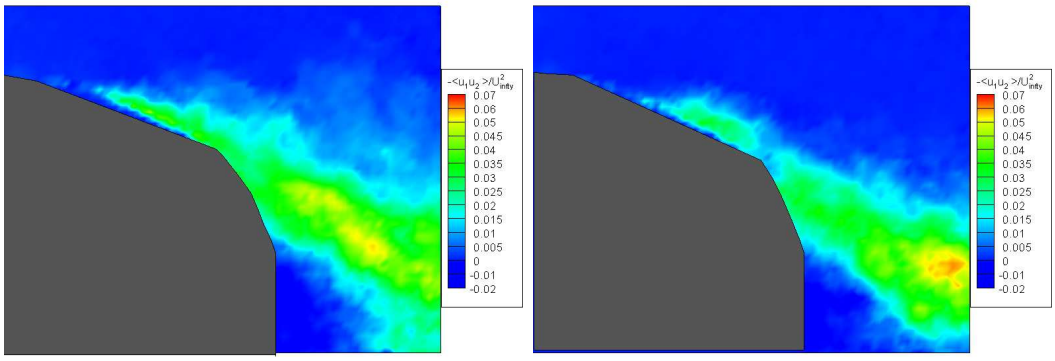

(a) $\alpha = 110°$, Start of Cycle

(b) $\alpha = 115°$, Pitching Backwards

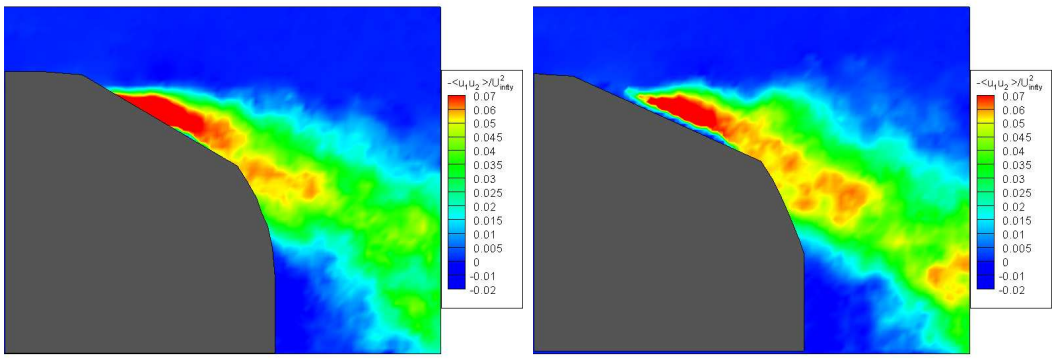

(c) $\alpha = 120°$

(d) $\alpha = 115°$, Pitching Forwards

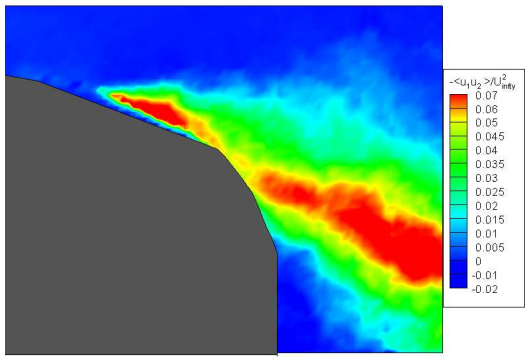

(e) $\alpha = 110°$, End of Cycle

Figure 3.20: $-\langle u_1 u_2 \rangle / U_\infty^2$ contours of DC of 90% pitching turret.

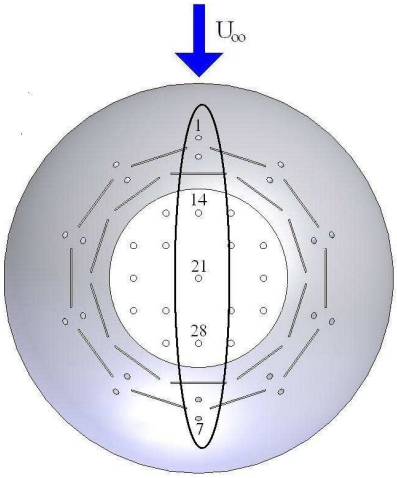

(a) Sensor Location

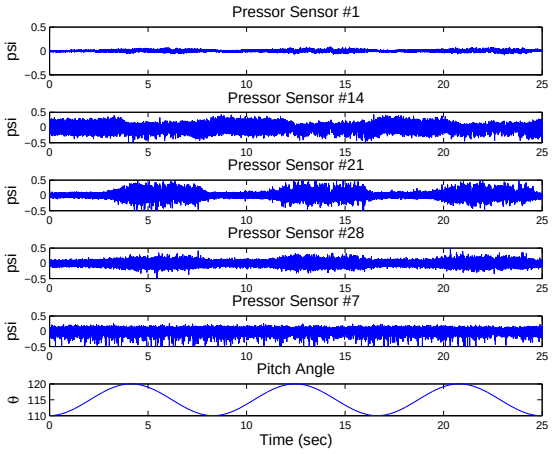

(b) Pressure Time Series

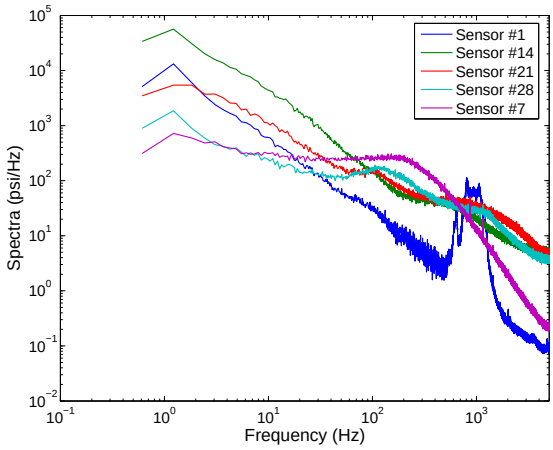

(c) Spectra

Figure 3.21: The centerline fluctuating surface pressure in time and frequency space for the 90% duty cycle suction case. The freestream flow is from top of the page to the bottom.

band peaks at 100Hz and 1000Hz in the baseline case were reduced in amplitude for the 90% duty cycle case. The shifts in the low and high frequencies infer that the flow structures were being altered by the actuation. The spectrum for Sensor 7, like in the baseline case, indicates the flow is massively separated throughout the pitch cycle.

An indication of the amount of the performance of reducing the fluctuation velocity can be seen in the reduction of the spatially averaged u_{rms}. The spatial velocity root mean square, $\langle u_{rms} \rangle$, was obtained by integration of the u_{rms} over the PIV window area, where the u_{rms} is defined in Equation 3.1. The cost of the suction system is defined as the amount of duty cycle. The overall cost is defined as the average duty cycle ($\langle DC \rangle (\%)$) throughout the control case. Utilizing the change in $\langle u_{rms} \rangle$ and the average duty cycle, $\langle DC \rangle$, of the control run a controller efficiency (ξ) can be quantified with the following term:

$$\xi = \left| \frac{\langle u_{\text{rms}} \rangle_{\text{Control}} - \langle u_{\text{rms}} \rangle_{\text{No Control}}}{\langle DC \rangle} \right|. \tag{3.6}$$

The efficiency does have units of m/s but does not have any significance. Table 3.3 shows the normalized spatial u_{rms}, average duty cycle, and the efficiency of the actuation system for each open loop case. The suction actuation reduced the spacial

Run Description	$\frac{\langle u_{\text{rms}} \rangle}{U_\infty}$	$\langle DC \rangle$ (%)	ξ
0% Duty Cycle	0.18	0	–
30% Duty Cycle	0.11	30	0.12
50% Duty Cycle	0.08	50	0.11
70% Duty Cycle	0.07	70	0.09
90% Duty Cycle	0.06	90	0.07

Table 3.3: Summary of no and open loop control results from the dynamically pitching turret.

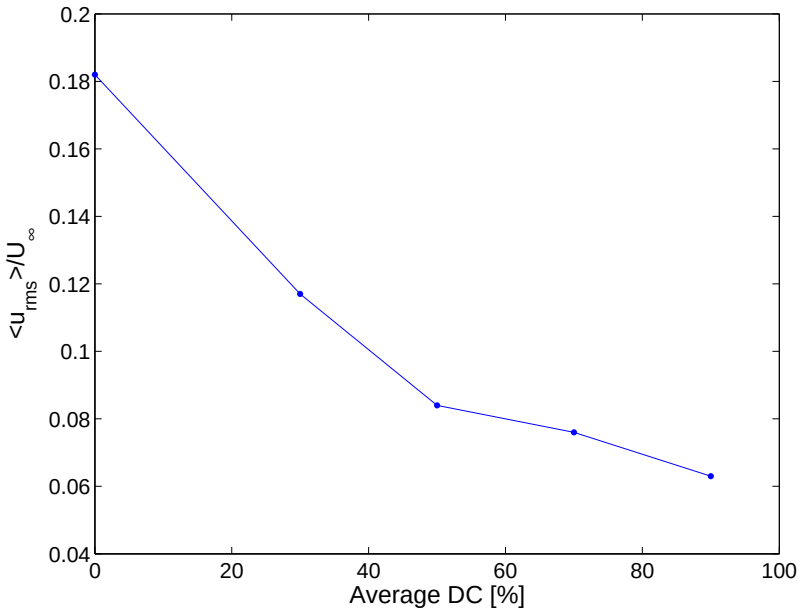

Figure 3.22: Open loop control $\frac{\langle u_{\mathrm{rms}} \rangle}{U_\infty}$ versus duty cycle for a pitching turret

u_{rms} within the flow over aperture. The greater the suction, the greater cost required to achieve the decrease in $\langle u_{rms} \rangle$. Figure 3.22 shows the $\frac{\langle u_{\mathrm{rms}} \rangle}{U_\infty}$ at the various duty cycle cases.

The hysteresis of the $\frac{\langle u_{\mathrm{rms}} \rangle}{U_\infty}$ for baseline and open loop control can be seen in Figure 3.23. Comparison of the baseline and open loop control shows a significant drop in the $\frac{\langle u_{\mathrm{rms}} \rangle}{U_\infty}$ through out the pitch cycle. Both panels show a delay in the flow as the turret pitches.

Unlike the static pitch open loop control cases, the duty cycle showed a more subtle change in flow in the frequency space. Figure 3.24(b) shows the spectrum for each of the control cases at the center pressure sensor of the aperture (Sensor No. 21). In the frequency range below $10Hz$, the control cases observed a decrease in the amplitude of the spectra, while for the frequencies above $10Hz$ there was a slight increase. The slight changes were due to a persistent shear layer over the aperture.

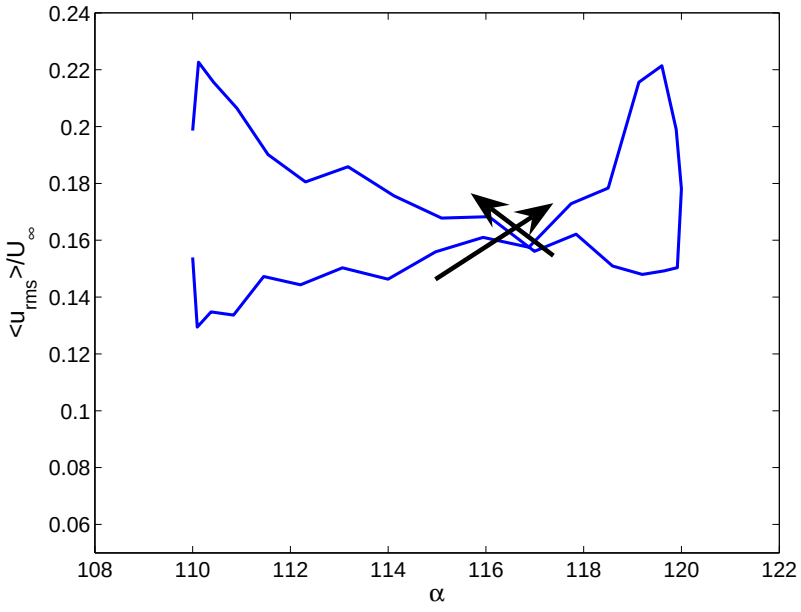

(a) Baseline

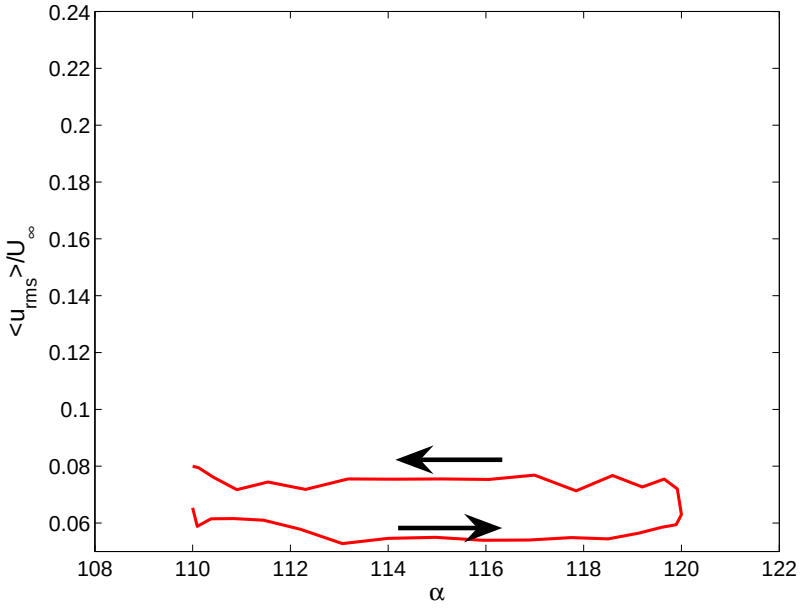

(b) 90 % Duty Cycle

Figure 3.23: Comparison of the hysteresis of the normalized $< u_{rms} >$ between baseline and open loop control for a pitching turret.

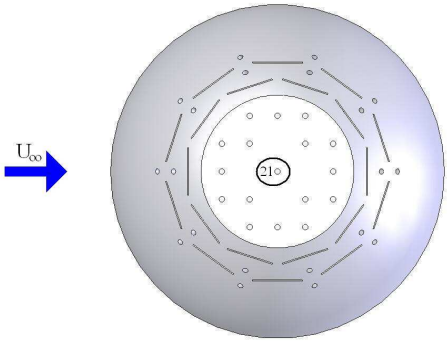

(a) Sensor Location

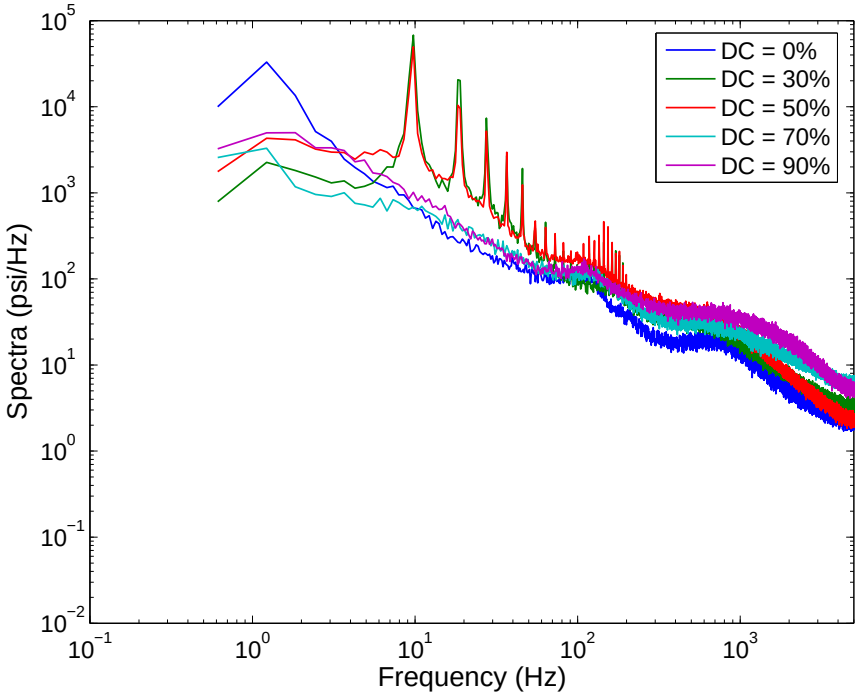

(b) Spectra

Figure 3.24: Spectrum of the center aperture pressure sensor (Sensor No. 21) for a dynamically pitching hemisphere at various duty cycles.

Although the $\langle u_{rms} \rangle$ was significantly reduced by the suction, a shear layer was still present over the aperture of the turret. Like the static pitch open loop cases of 30% and 50%, spikes were present at $10Hz$ but in this case a harmonic frequency has seemed to have developed within the flow.

3.3.3 Simple Proportional Closed-loop Control for a Pitching Turret

In attempt to build a more efficient flow control system than the open loop unsteady suction modulation, a control system was design in which the suction modulation would be altered as the adverse pressure and velocity fluctuation increase or decrease over the aperture. The goal of the adaptive flow control was to keep the flow attached to the aperture with a minimum amount of actuation.

Like the previous runs, the turret was pitched at a rate of $\omega = 2.4$ deg/s between 110° and 120° according to the function in Equation 3.4.

Controller Design

For the case with no flow control over a pitching turret, it has already been shown in Section 3.3.1 that at the higher pitch angles a strong adverse pressure gradient forms which causes the flow to separate over the aperture. As the hemisphere rotated through its pitch cycle with no flow control the amplitude of the fluctuating surface pressure at Sensor No. 1 showed a strong correlation to the pitch angle. Seen in the top panel of Figure 3.16(b), as the pitch angle increased the fluctuating surface pressure amplitude increased and as the pitch angle decreased the amplitude of the fluctuating surface pressure decreased as well. Work done by Pinier et al. [58] utilized a feedback control signal (estimated POD expansion coefficients) in which the amplitude of the

signal corresponded to separated flow. Noticing the a similar trend, the Sensor No. 1's fluctuating pressure signal was used as a feed back signal in a simple proportional closed loop controller. Before the pressure signal was outputted from the controller, the signal was digitally filtered at various frequencies using a Butterworth filter. Four closed loop control cases were explored with different filter cases:

- Band Pass: Frequencies (Hz) in the range $[30, 500]$,
- Band Stop: Frequencies (Hz) in the range $[0, 8] \cup [12, 500]$,
- Low Pass: Frequencies (Hz) in the range $[0, 500]$,
- Very Low Pass: Frequencies (Hz) in the range $[0, 8]$.

The upper end of the band pass, band stop, and low pass filters were set to remove the frequencies within the flow above 500Hz. The frequencies above 500Hz are associated with the small structures and can be considered as noise for feedback control purposes. The lower end of the band pass filter was set to remove the frequencies below 30Hz; this range contains the majority of actuation energy within the flow, as seen in Figure 3.24(b). The lower limit of the band stop was set to remove the range of frequencies associated with the first peak of the actuation, as seen in Figure 3.24(b). For the last filter, very low pass filter was set to remove the frequencies above 8Hz, eliminating the frequencies containing the actuation and only keeping the large scale structure information.

A simple proportional controller was implemented for the initial closed loop control system. The controller is described in Equation 3.7 and in illustrated in Figure 3.25.

$$\dot{u} = \begin{cases} Kp_1 & 0 < t < \mathcal{T}p_1 \\ 0 & \mathcal{T}p_1 < t < \mathcal{T} \end{cases} \tag{3.7}$$

The period of the carrier frequency of the actuation signal to the valves at 25Hz is defined as $\mathcal{T}$.

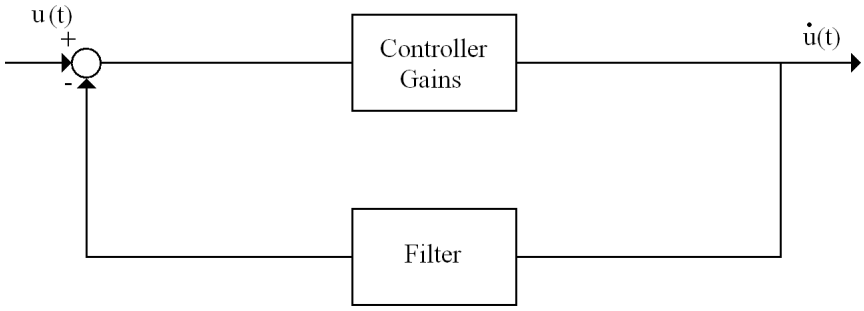

Figure 3.25: Control Diagram for the Simple Proportional Controller.

Thus, the duty cycle percentage is directly proportional to the amplitude of the fluctuating pressure of Sensor No. 1. All of the 20 jet slots were activated, operating as a single unit in each closed-loop control case. Although the ultimate objective of the closed-loop control was to reduce velocity fluctuations over the aperture, the controller objective for the initial closed-loop cases was to drive the pressure rms of Sensor No. 1 to zero. The gain, K, was adjusted to ensure that the feed back signal was between 0 and 100% duty cycle. Thus, K was set to 1200 and has no units.

Closed Loop Flow Control Results

Figure 3.26 shows the closed loop control case of band pass filtered, phase averaged velocity magnitude measurements of 102 pitching cycles at five elevation angles for the band pass filtered case. As the hemisphere rotated through its pitch cycle, the suction actuation was able to prevent the flow from massively separating. Although the separation was reduced, a shear layer over the aperture did persist through out the pitch cycle. Similar results of the separation suppression and a persistent shear

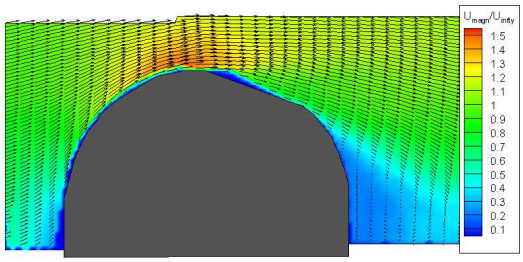

(a) $\alpha = 110°$, Start of Cycle

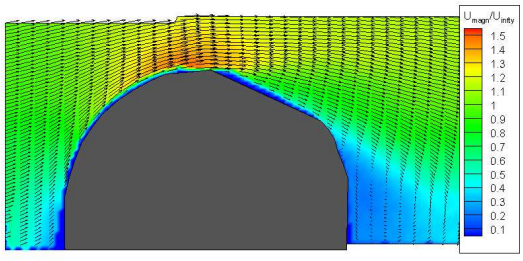

(b) $\alpha = 115°$ Pitching Backwards

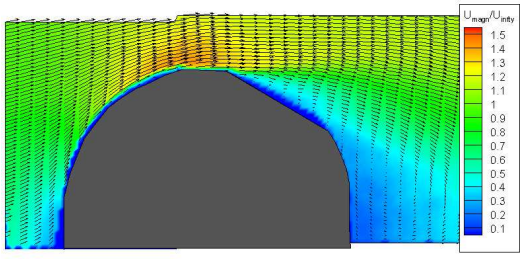

(c) $\alpha = 120°$

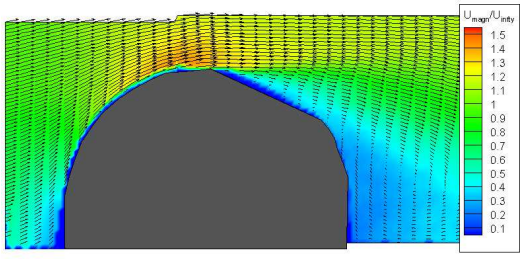

(d) $\alpha = 115°$ Pitching Forwards

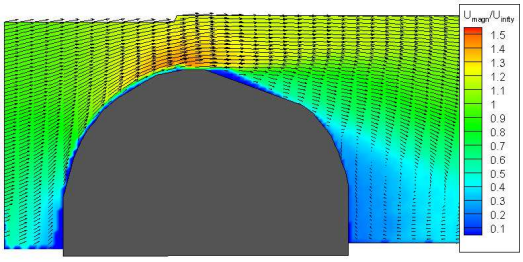

(e) $\alpha = 110°$, End of Cycle

Figure 3.26: Normalized mean velocity magnitude ($\langle\sqrt{\tilde{u}_1^2 + \tilde{u}_2^2}\rangle/U_\infty$) contours and mean velocity vectors of simple close loop control for the band pass filtered case.

layer over the aperture were seen in both the band stop filter and low pass filter cases. For the last simple closed-loop case of the very low pass filter, the flow did separate over the aperture at the extreme elevation angles. The poor performance of the very low pass filter case indicates that the filter removed too much of the frequency content within the feedback signal to be an effective controller.

Shown in Figure 3.27 is the u_{rms} for the band pass filtered, closed loop control case. Throughout the pitch cycle the u_{rms} remained low as compared to the baseline pitching case. The high u_{rms} area seen in both Figures 3.14 and 3.19 was significantly reduced over the aperture. The closed loop control was able to keep high velocity fluctuations over the aperture from occurring. An area of moderate shear stress seems to remain over the aperture of the turret with the same intensity throughout the pitch cycle, as seen in Figure 3.28. Comparing Figure 3.28 to the baseline case seen in Figure 3.20, the intensity of $\frac{-\langle u_1 u_2 \rangle}{U_\infty^2}$ was significantly reduced.

Figure 3.29 shows the separation height of the wake behind the pitching turret at various elevation angles. Closed loop control reduced the size of the wake more consistently than open loop control due to its ability to adapt to the changing flow conditions.

The fluctuating surface pressure time series of the centerline sensors, seen in Figure 3.30(b), shows the effect on the flow of the band pass filtered, closed loop flow control case. The drop in the amplitude of fluctuating pressure at the high elevation angles in the baseline, dynamic pitching case (Figure 3.16(b)) was eliminated with the closed loop control. The fluctuating pressure signals on the aperture seem to be constant throughout the time history, indicating that the control input delayed the onset of massive separation. Comparing the closed loop control case in Figure 3.30(b) to the open loop control case in Figure 3.21(b) the flow over the aperture remains more consistent throughout the pitch cycle without a dramatic increase in the amplitude

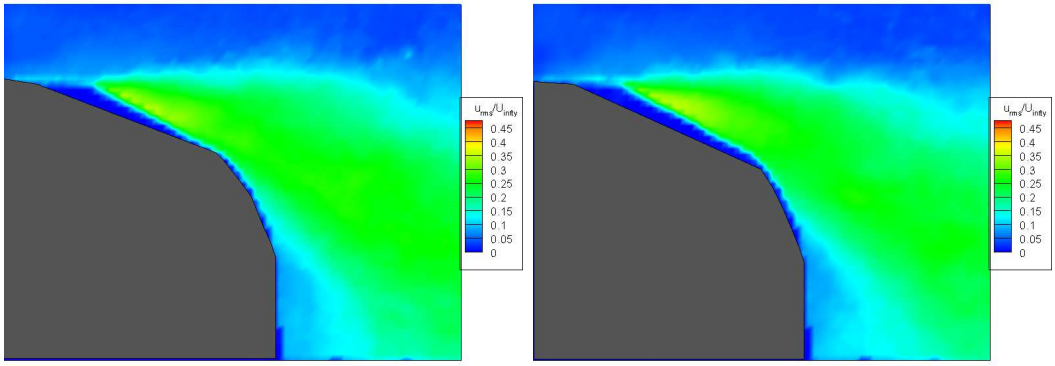

(a) $\alpha = 110°$, Start of Cycle

(b) $\alpha = 115°$ Pitching Backwards

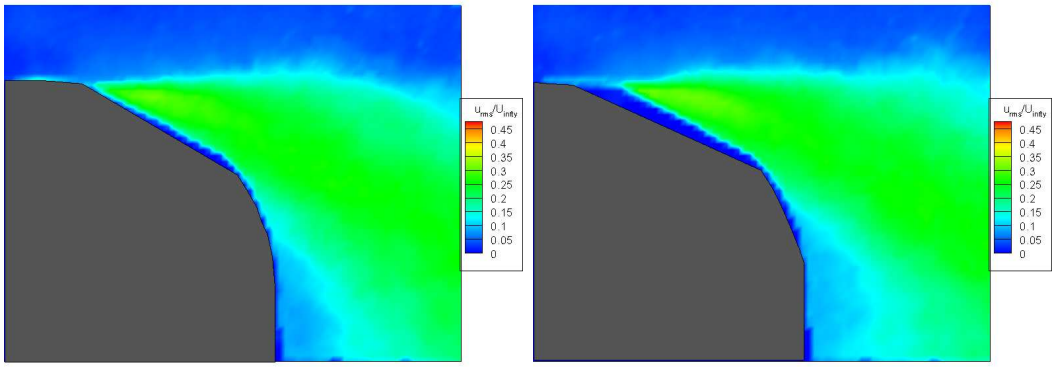

(c) $\alpha = 120°$

(d) $\alpha = 115°$ Pitching Forwards

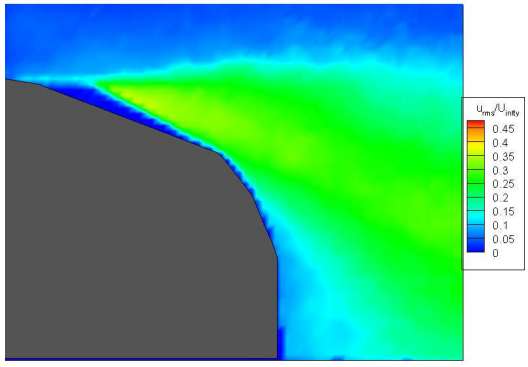

(e) $\alpha = 110°$, End of Cycle

Figure 3.27: u_{rms}/U_∞ contours of band pass filtered closed loop control pitching turret.

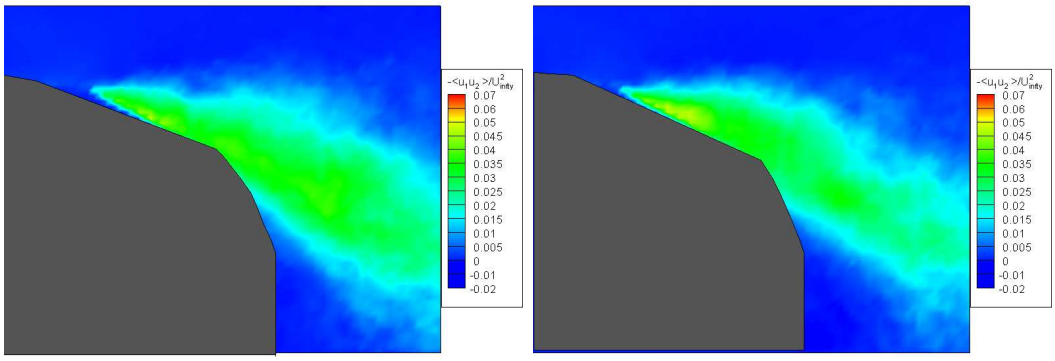

(a) $\alpha = 110°$, Start of Cycle

(b) $\alpha = 115°$ Pitching Backwards

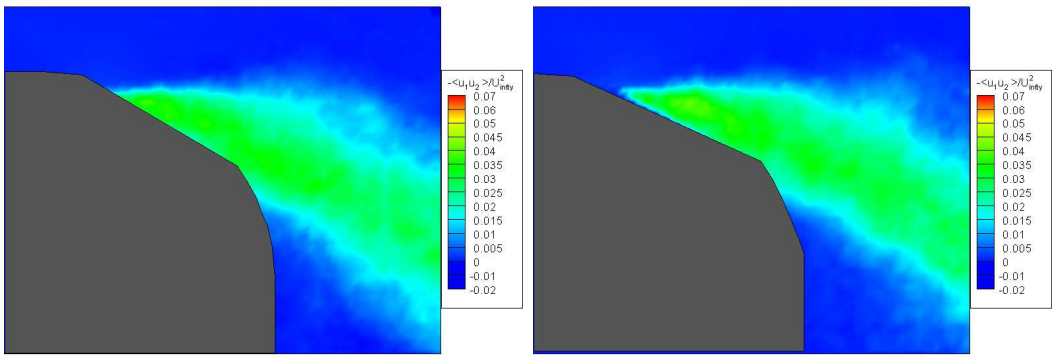

(c) $\alpha = 120°$

(d) $\alpha = 115°$ Pitching Forwards

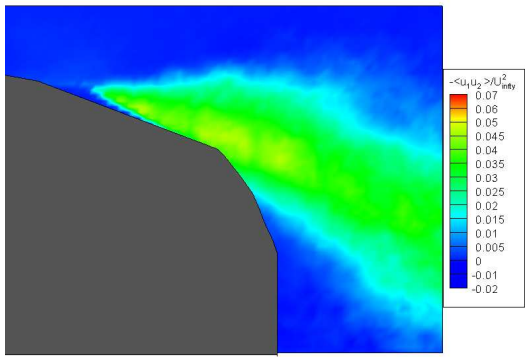

(e) $\alpha = 110°$, End of Cycle

Figure 3.28: $-\langle u_1u_2\rangle/U^2_\infty$ contours of band pass filtered closed loop control pitching turret.

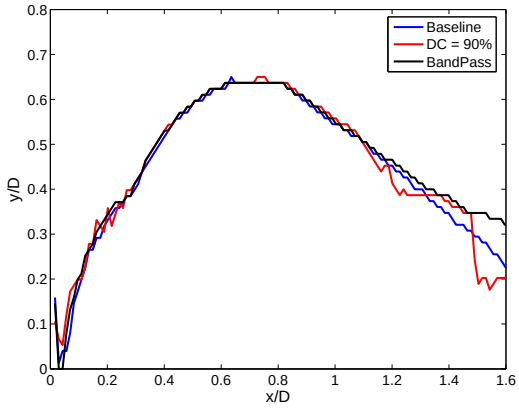

(a) $\alpha = 110°$, Start of Cycle

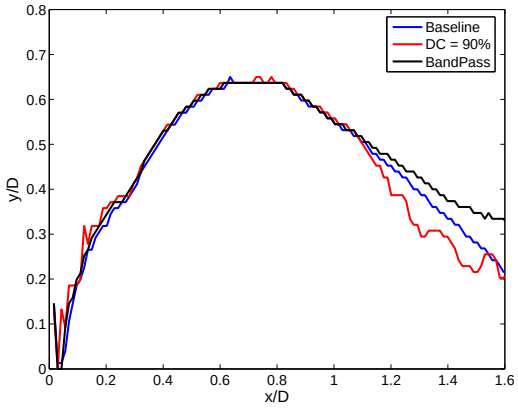

(b) $\alpha = 115°$ Pitching Backwards

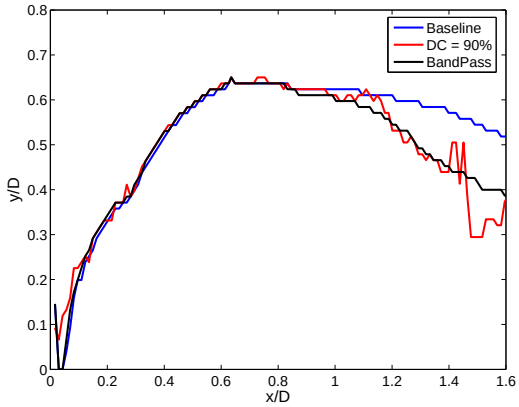

(c) $\alpha = 120°$

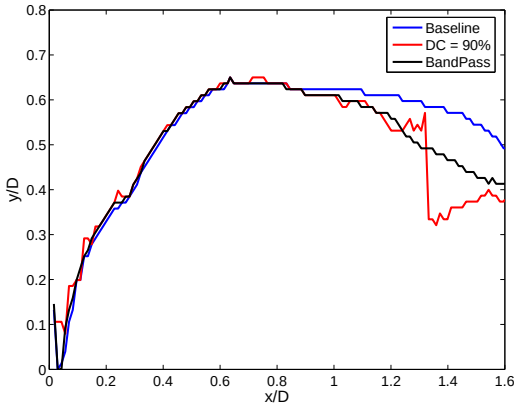

(d) $\alpha = 115°$ Pitching Forwards

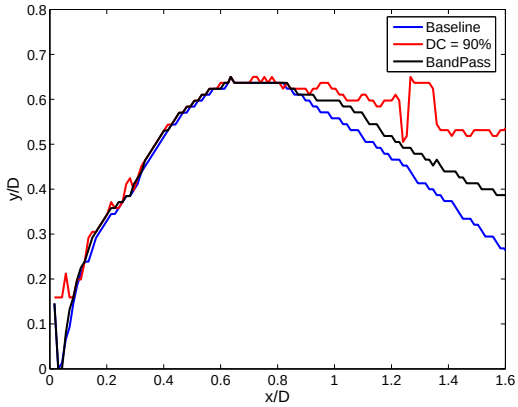

(e) $\alpha = 110°$, End of Cycle

Figure 3.29: Separation height of the pitching turret. Based on location of 99% of the freestream velocity.

of the fluctuating pressure. Figure 3.30(c) shows the spectra at the centerline of the

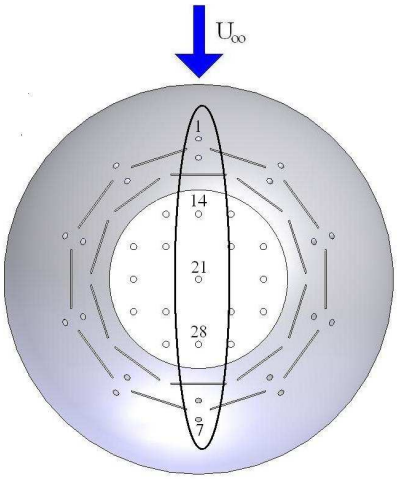

(a) Sensor Location

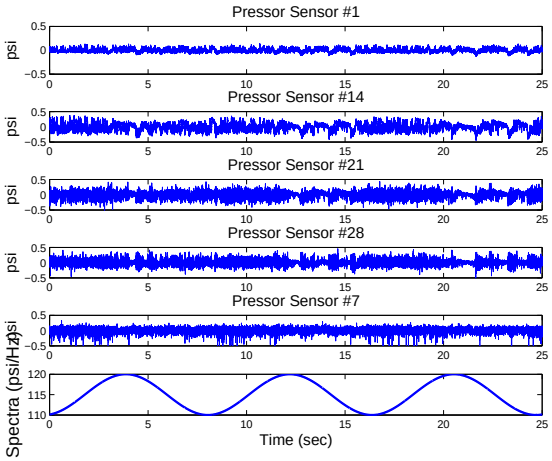

(b) Pressure Time Series

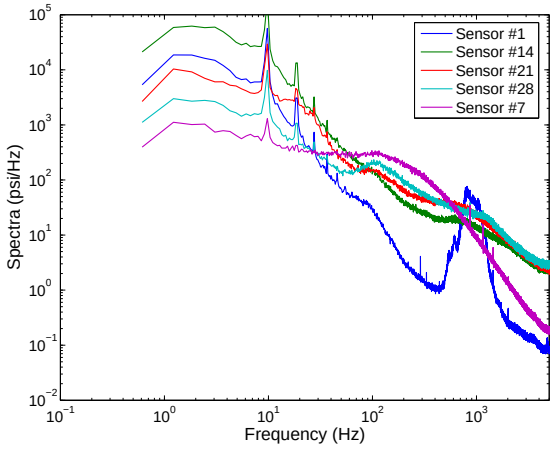

(c) Spectra

Figure 3.30: The centerline fluctuating surface pressure in time and frequency space with band pass filtered closed loop control. The freestream flow is from top of the page to the bottom.

turret for the band pass filtered, closed loop control case. In the low frequency range, the sensors on the aperture have a broad peak to about 30Hz. This indicates a wide range of large scale structures within the flow. The peak at 10 Hz is associated with the control input. The unsteady suction modulation introduces large scale structures

into flow with a frequency of about 10Hz. Although the flow was completely separated throughout the pitch cycle at the location of Sensor 7, a peak at 10 Hz is seen as well. Thus, the flow structure introduced by the control input was sensed over the entire hemisphere.

Table 3.4 shows the performance output in terms of the normalized averaged spatial $\langle u_{rms} \rangle$, averaged duty cycle, and efficiency (all defined in Section 3.3.2) for each closed loop control case. The low pass filtered case reduced the normalized $\langle u_{rms} \rangle$ the greatest out of the four closed loop control cases. Although the low pass filtered case had the greatest reduction, this controller paid a heavy cost in the required amount of suction, shown in terms of $\langle DC \rangle$. On the other hand the very low pass case has the least reduction for a moderate cost in duty cycle. Overall the simple closed loop control was able to have a significant reduction in the turbulence level above the turret. Figure 3.22 shows the $\frac{\langle u_{\mathrm{rms}} \rangle}{U_\infty}$ at the various closed loop control cases.

Run Description	$\frac{\langle u_{\mathrm{rms}} \rangle}{U_\infty}$	$\langle DC \rangle$ (%)	ξ
0% Duty Cycle	0.182	0	–
Band Pass	0.0881	33	0.15
Band Stop	0.0728	44	0.13
Low Pass	0.0655	42	0.15
Very Low Pass	0.0970	35	0.13

Table 3.4: Summary of baseline and the various closed loop control results from the dynamically pitching turret.

The hysteresis of the $\frac{\langle u_{\mathrm{rms}} \rangle}{U_\infty}$ for baseline, open loop control, and closed loop control can be seen in Figure 3.32.

The spectrum of Sensor no. 21 in Figure 3.33 shows the changes due to the closed loop control cases. The frequency response in the lower ranges is much broader than the baseline case. Another interesting trend is that even though the very low pass

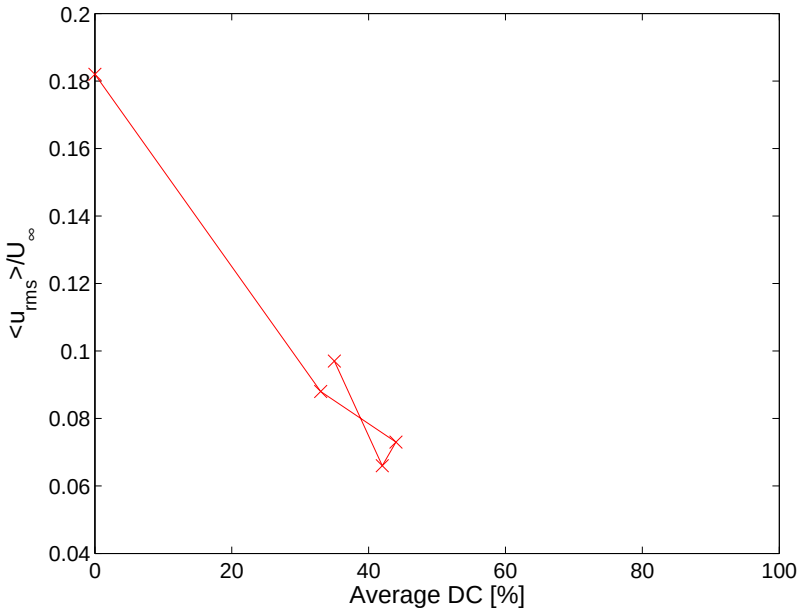

Figure 3.31: Initial loop control $\frac{\langle u_{\mathrm{rms}} \rangle}{U_\infty}$ versus duty cycle for a pitching turret

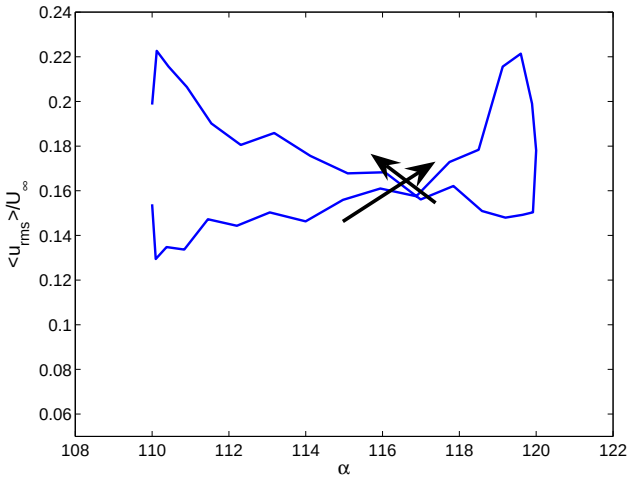

(a) Baseline

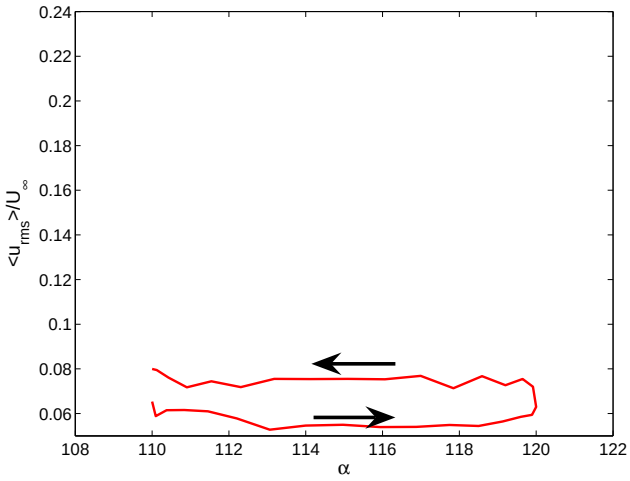

(b) 90 % Duty Cycle

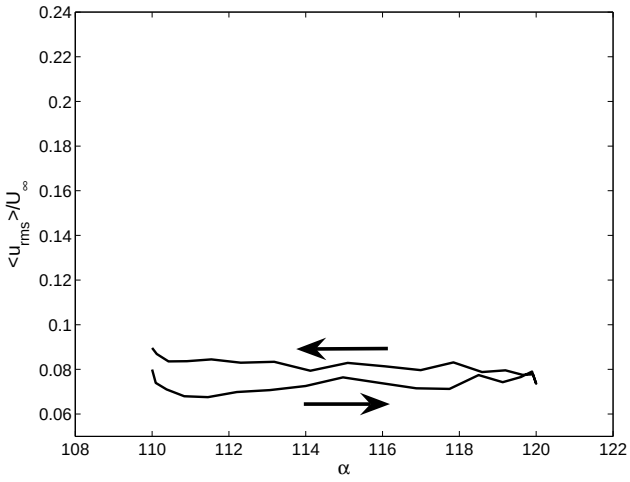

(c) Band Pass Filtered

Figure 3.32: Comparison of the hysteresis of the normalized $\langle u_{\text{rms}} \rangle$ between baseline, open loop control, and closed loop control for a pitching turret.

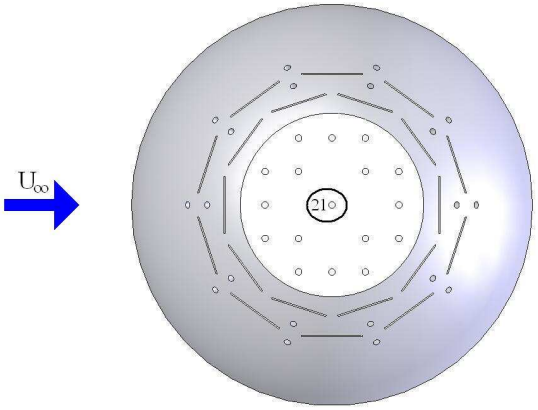

(a) Sensor Location

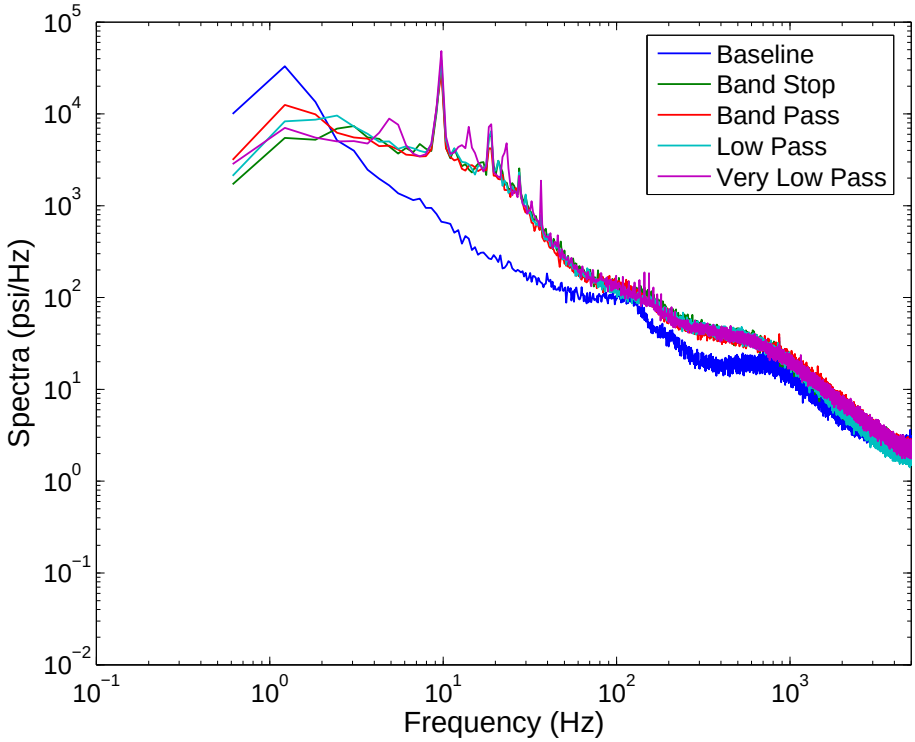

(b) Spectra

Figure 3.33: Spectrum of the center aperture pressure sensor (Sensor No. 21) for a dynamically pitching hemisphere with the various closed-loop control cases.

case is clearly not performing as well as the others, each of the closed-loop control laid upon each other in the frequencies above 20Hz.

3.4 Measurement and Dynamical Model-Based Feedback Flow Control

The closed loop control system in Section 3.3.3 showed a significant decrease in the u_{rms} along with a reduction in the average duty cycle cost of the suction system. Building upon this success a more advanced control system employing a measurement estimator coupled with a dynamical estimator was developed and demonstrated in a joint effort by Clear Science Corp. and Syracuse University. The more advance closed loop control system was initially developed in CFD and implemented in experimental test. The experimental tests were not used as validation for the CFD but for implementation of the CFD developed controller.

This work can be found in further detail in Thirunavukkarasu et al. [80] and Wallace et al. [86]. It is also included in this for completeness.

3.4.1 The CFD Model

The CFD model employs the method of Detached Eddy Simulation (DES), first proposed by Spalart et al. [69] and applicable to turbulent flows—particularly flows with separation. Large Eddy Simulation (LES) is an alternative method that uses filters to resolve some (but not all) of the length scales in a turbulent flow as described by Squires [72]. This requires a considerably finer grid than a Reynolds-Averaged Navier-Stokes (RANS) model does, because the RANS model resolves only the mean flow. LES can become computationally expensive in many problems involving high

Reynolds number flows with a large range in scales. A hybrid RANS-DES formulation provides a compromise between fidelity and expense by resolving larger eddies in the outer flow where separation-induced structures reside and reverting to the RANS model in the wall region where length scales are very small. The CFD code is CFL3D [11], and a one-equation, Spalart-Allmaras (S-A) turbulence model [71] is applied in the wall region.

The S-A model contains a destruction term, which is proportional to $(\tilde{\nu}/d)^2$ where d is the distance to the wall and $\tilde{\nu}$ is the eddy viscosity. When balanced with the production term, this term adjusts the eddy viscosity to scale with the local deformation rate (S) and d: $\tilde{\nu} \propto Sd^2$. Sub-grid-scale (SGS) eddy viscosities are proportional to S and the grid spacing Δ: $\tilde{\nu}_{\mathrm{SGS}} \propto S\Delta^2$. The S-A SGS model is derived by replacing d with a length scale Δ that is proportional to the grid spacing. The model used in the DES formulation is derived by replacing the length scale of the S-A destruction term to be the minimum of Δ and the distance to the closest wall: $\tilde{d} \equiv \min(d, C_{\mathrm{DES}}\Delta)$ where $\Delta \equiv \max(\Delta x_1, \Delta x_2, \Delta x_3)$ and $C_{\mathrm{DES}} = 0.65$.

Figure 3.34 contains views of the CFD grid. The left panel of Figure 3.34 contains a projection of the grid onto the lower boundary of the computational domain. The other outer boundaries are located 15 turret diameters from the turret surface in a radial direction. The middle panel of the figure contains a projection of the grid onto the turret surface. The centerline of the turret is coincident with the x_2-axis. The right panel contains a slice of the grid on the centerplane. The turret is symmetric about this plane, but symmetry is not imposed. The full domain is modeled in order to accommodate rotations in the yaw direction (about the x_2 axis). The grid is structured with a total of 14.68 million points. The wall spacing is 2.54×10^{-4} centimeters, yielding $y^+ \sim 0.8$ at a Reynolds number of 450,000. The spatial resolution is finer in the region around the aperture in order to adequately resolve the separated flow with

DES.

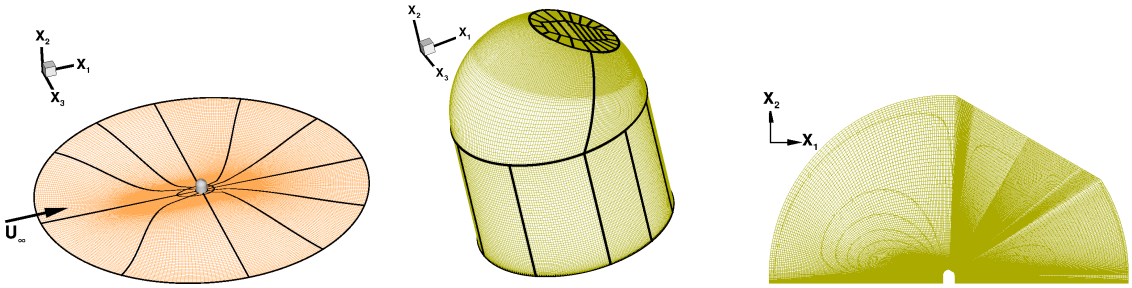

Figure 3.34: Views of the 3D CFD grid. Projections of the grid onto the bottom boundary (left), the turret surface (middle), and the centerplane (right).

In the control simulations, the turret pitches sinusoidally about the x_3 axis only, according to the following prescribed function:

$$\theta(t) = \theta_0 + \Delta\theta \left(\frac{\pi}{180}\right) \sin\left[\left(\frac{2\pi k_r}{L_{ref}}\right) t\right]. \tag{3.8}$$

θ_0 is the nominal pitch angle of $2\pi/3$ or 120°: the angle between a line normal to the aperture and the free stream flow direction ($+x_1$ axis). $\Delta\theta = 1°$ yields an oscillation range between 119° and 121°. k_r is the reduced frequency ($k_r = 0.0415$), and $L_{ref} =$ 15.24 centimeters. The dimensionless time in Equation 3.8 is non-dimensionalized by L_{ref} and the free stream speed of sound. Differentiating Equation 3.8 with respect to time yields a maximum pitch rate of 587 degrees per second.

3.4.2 Model-Based Controller Design

Control Input and Performance Output

The control objective is to minimize levels of separation and velocity fluctuations above the aperture. The performance output should be a measure of these levels. Control then becomes a tracking problem with the controller maintaining, or tracking,

a value of the performance output that corresponds to low levels of separation and velocity fluctuations. Flow begins to separate when the wall-normal velocity gradient at the wall approaches zero. The viscous component of force acting on the turret surface is a function of the velocity gradients and wall shear stresses through the constitutive relation. The streamwise component of viscous force, or integrated shear stress, acting on the aperture surface (Ω) is

$$F_V^1 = \frac{\varpi}{2} \int \left(\frac{\partial u^l}{\partial x^1} + \frac{\partial u^1}{\partial x^l} \right) n^l \, d\Omega. \tag{3.9}$$

where $\varpi = 2Ma_\infty / Re_\infty$ and n^l is the l component of the surface normal.

An initial control test utilized values of the performance output computed by the high-dimensional CFD model. These CFD data will not be available in practical applications, but the initial tests are designed to evaluate the performance of regulators. In the actual control-in-the-loop simulations, the performance output is approximated by low-dimensional estimators. In both the initial and final tests, the output is defined as integrated shear stress: $y = F_{\mathrm{V}}^1$. The target value of the output is equal to the time-averaged integrated shear stress for which the flow is attached: $y_T = 0.0362$. Lower, more negative values of the shear stress, integrated over the aperture surface, correspond to higher levels of separation above the surface; therefore, increasing F_V^1 will reduce separation.

Figure 3.35 contains results from the initial control run with CFD-computed output in the loop: time histories of performance output in the left panel and control input in the right. From the red curve in the left panel, fluctuations in the output are small when the turret is stationary at the nominal pitch angle; the value is slightly negative. For the pitching turret without actuation (blue curve), oscillations in output are significant with values dipping below -0.02 when the turret is pitched fully

back. From the green curve in the left panel, open-loop control raises the mean value of output, but the oscillation levels actually increase, even though positive values are maintained. In the open-loop simulation, the suction jet is steady with a momentum coefficient of $c_\mu = -0.0138$ (the green curve in the right panel of Figure 3.35). From the purple curve in the left panel, the closed-loop controller produces lower oscillations in output than the open-loop controller. From the purple curve in the right panel, it does so with fairly large changes in control input, which varies between values of -0.002 and -0.04.

Low-Dimensional Estimators

Deployable feedback systems that control in real time will have to rely on models that are much more computationally efficient than the high-dimensional CFD model. To that end, two types of low-dimensional state estimators have been developed and tested: measurement-based and dynamical. Used together, these two components form a compensator and Kalman filter for dealing with uncertainties and noise, as described in Section 3.4.2. The system state is defined as a perturbation velocity ($\acute{u}^i(\mathbf{x}, t)$). A low-dimensional approximation of $\acute{u}^i(\mathbf{x}, t)$ is derived by the method of proper orthogonal decomposition (POD) [43].

A correlation tensor is constructed using N snapshots (solutions) of the unsteady flow at $t = t_{(1)}, t_{(2)}, ..., t_{(N)}$:

$$R_{(mn)} = \int_\Omega \acute{u}^i_{(m)}(\mathbf{x})\acute{u}^j_{(n)}(\mathbf{x})d\mathbf{x} \quad (m, n = 1, ..., N)\,, \tag{3.10}$$

with $\acute{u}^i_{(m)}(\mathbf{x}) = \acute{u}^i(\mathbf{x}, t_{(m)})$ denoting the ith contravariant component of perturbation velocity from snapshot m (a single solution at a particular time step from an unsteady CFD simulation). Constructed in this manner, the eigenvectors of $R_{(mn)}$ maximize

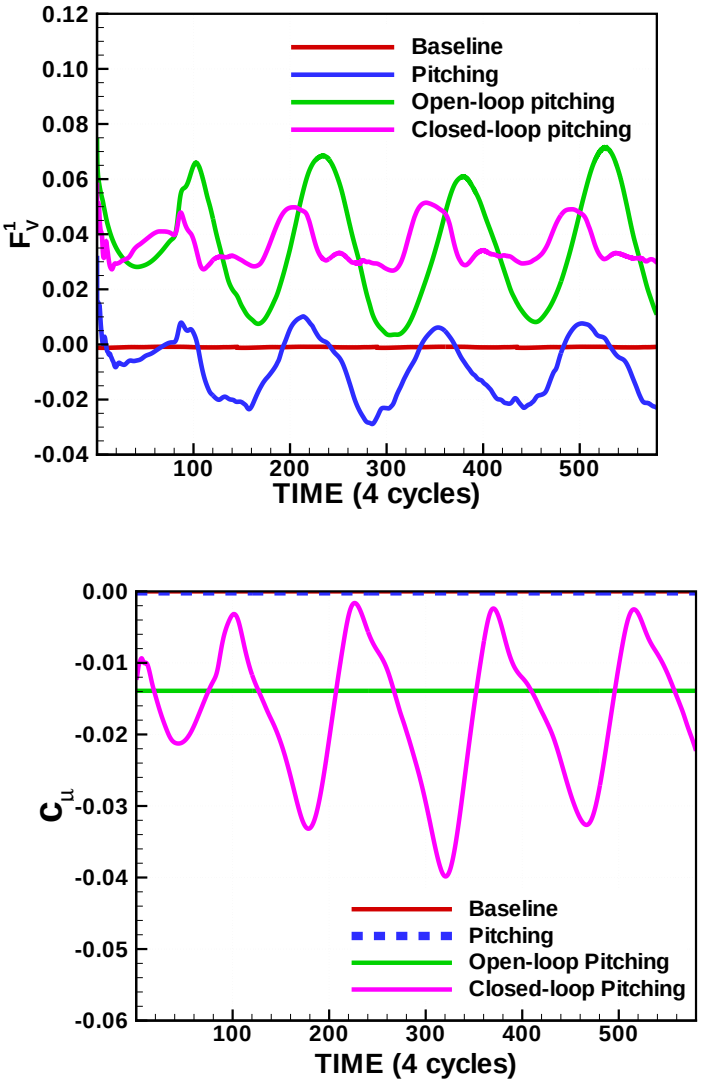

Figure 3.35: Time histories of performance output (left panel) and control input (right panel) from simulations with no actuation (red and blue curves), an open-loop control simulation (green curves), and a closed-loop control simulation with CFD-computed output in the loop (purple curves).

the mean square projection of the flow velocity, represented as

$$\acute{u}^i(\mathbf{x},t) = a_{(n)}(t)\phi^i_{(n)}(\mathbf{x}) \tag{3.11}$$

where

$$a_{(n)}(t) = \int_\Omega \acute{u}^i(\mathbf{x},t)\phi_i^{(n)}(\mathbf{x})d\mathbf{x}\,, \tag{3.12}$$

Using 51 snapshots from an unsteady simulation to construct the POD model, 98% of the kinetic energy in the flow is represented in just two POD modes. The time-dependent coefficients of these two modes, $a_{(1),(2)}(t)$, form the state estimates that are used by both the dynamical and measurement-based estimators.

The dynamical estimator is derived by projecting the momentum conservation equation (a partial differential equation, PDE) onto a low-dimensional set of POD eigenvectors, producing a set of coupled ordinary differential equations (ODEs):

$$\begin{aligned}\frac{da_{(n)}}{dt} = \; & \alpha^{<0000>}_{(n)} + \varpi\alpha^{<1000>}_{(n)} + \left(\alpha^{<0010>}_{(n)(\mu)} + \varpi\alpha^{<1010>}_{(n)(\mu)}\right)\dot{\eta}_{(\mu)} + \alpha^{<0001>}_{(n)(\mu)}\frac{d\dot{\eta}_{(\mu)}}{dt} \\ & + \alpha^{<0020>}_{(n)(\mu\nu)}\dot{\eta}_{(\mu)}\dot{\eta}_{(\nu)} + \left(A^{<0100>}_{(np)} + \varpi A^{<1100>}_{(np)} + A^{<0110>}_{(np)(\mu)}\dot{\eta}_{(\mu)}\right)a_{(p)} + A^{<0200>}_{(npq)}a_{(p)}a_{(q)} \\ & + \left(\beta^{<0100>}_{(n)(\rho)} + \varpi\beta^{<1100>}_{(n)(\rho)} + \beta^{<0110>}_{(n)(\rho)(\mu)}\dot{\eta}_{(\mu)} + B^{<0200>}_{(np)(\rho)}a_{(p)}\right)\zeta_{(\rho)} \\ & + \beta^{<0001>}_{(n)(\rho)}\frac{d\zeta_{(\rho)}}{dt} + \beta^{<0200>}_{(n)(\rho\sigma)}\zeta_{(\rho)}\zeta_{(\sigma)}.\end{aligned} \tag{3.13}$$

The system in Equation 3.13 contains linear and bi-linear terms involving $a_{(n)}$, $\zeta_{(\rho)}$, and $\dot{\eta}_{(\mu)}$. The POD coefficient $a_{(n)}$ is the dependent variable, $\zeta_{(\rho)}$ is the surface jet magnitude, and $\dot{\eta}_{(\mu)}$ is a modal representation of surface velocity due to rotation of the turret. In the case of the pitching turret with only one rotational degree of freedom, $\mu = 1$ and $\eta = \theta$. $\alpha^{<0000>}_{(n)}$, $\alpha^{<1000>}_{(n)}$, $\alpha^{<0010>}_{(n)(\mu)}$, $\alpha^{<1010>}_{(n)(\mu)}$, $\alpha^{<0001>}_{(n)(\mu)}$, $\alpha^{<0020>}_{(n)(\mu\nu)}$, $A^{<0100>}_{(np)}$, $A^{<1100>}_{(np)}$, $A^{<0110>}_{(np)(\mu)}$, $A^{<0200>}_{(npq)}$, $\beta^{<0100>}_{(n)(\rho)}$, $\beta^{<1100>}_{(n)(\rho)}$, $\beta^{<0110>}_{(n)(\rho)(\mu)}$, $B^{<0200>}_{(np)(\rho)}$, $\beta^{<0001>}_{(n)(\rho)}$, and $\beta^{<0200>}_{(n)(\rho\sigma)}$

are time-invariant coefficients that are computed once during the model construction phase.

A linear dynamical estimator is formed by simply excluding the bi-linear terms in Equation 3.13:

$$\dot{\hat{\mathbf{x}}} = \mathbf{a}_0 + \mathbf{A}_1\hat{\mathbf{x}} + \mathbf{b}_0 u + \mathbf{b}_2\dot{u} + \mathbf{b}_3\dot{\eta} + \mathbf{b}_4\ddot{\eta} \tag{3.14}$$

where regular letters denote scalars, bold lower-case letters denote vectors and bold upper-case letters denote matrices. The vector $\hat{\mathbf{x}}$ is composed of POD coefficients, and the dynamical model in Equation 3.14 predicts the evolution in time of those coefficients.

Another important component of the control system is a measurement-based estimator developed by Adrian [1] and demonstrated numerically by Carlson and Miller [14], which correlates the flow dynamics around a surface with discrete measurements taken on the surface. Pressure measurements are used here. The key is that the measured quantity correlates with the state estimate (the POD coefficients). The estimated POD coefficient may be written as a series expansion with successive terms containing increasing powers of the pressure:

$$\tilde{a}_{(n)}(t;t) = B_{(ni)}p_{(i)}(t) + C_{(nij)}p_{(i)}(t)p_{(j)}(t) + D_{(nijk)}p_{(i)}(t)p_{(j)}(t)p_{(k)}(t) + \cdots \tag{3.15}$$

This may be truncated to include only the linear term:

$$\tilde{a}_{(n)}(t) \approx B_{(ni)}p_{(i)}(t). \tag{3.16}$$

The elements of $B_{(ni)}$ are selected to minimize the mean square difference between the measurement-based estimates of the system state and the actual state, computed by projecting CFD solutions onto the POD eigenfunctions. $\tilde{a}_{(n)}(t)$ are

measurement-based estimates of the POD coefficients that approximate the instantaneous perturbation velocity:

$$\tilde{u}^i(\mathbf{x},t) \approx \tilde{a}_{(n)}(t)\phi^i_{(n)}(\mathbf{x}). \tag{3.17}$$

State estimates from either the dynamical estimator or the measurement-based estimator (or both) will be used to approximate the performance output "in the loop." Substituting the low-dimensional velocity representation into Equation 3.9 yields the output approximation:

$$F^1_{\mathrm{V}} = \varpi(c^{<1000\mathrm{V}>1} + d^{<1100\mathrm{V}>1}_{(\rho)}\zeta_{(\rho)} + c^{<1010\mathrm{V}>1}_{(\mu)}\dot{\eta}_{(\mu)} + C^{<1100\mathrm{V}>1}_{(m)}a_{(m)}). \tag{3.18}$$

where $c^{<1000\mathrm{V}>1}$, $c^{<1010\mathrm{V}>1}_{(\mu)}$, $d^{<1100\mathrm{V}>1}_{(\rho)}$, and $C^{<1100\mathrm{V}>1}_{(m)}$ are integro-differential functions of velocity, computed off-line and only once, during the model construction step.

Before using them for control, estimators were constructed with data from the initial control simulation (with CFD-computed output in the loop), and their accuracies were evaluated. The left panel of Figure 3.36 compares time histories from the dynamical and measurement-based estimators over one pitching cycle (blue and green curves, respectively) with values obtained by projecting CFD solutions onto the POD eigenvectors (red curve). Comparisons are good with the exception of the measurement-based estimation of $a_{(2)}$, which captures the correct trend but is mixed with measurement noise. The second POD mode contains only a small percentage of the perturbation energy—as evidenced by the much smaller maximum value in the right vertical axis—and the signal-to-noise ratio is commensurately small. The right panel of Figure 3.36 compares time histories of performance output (viscous force acting on the aperture surface) using the dynamical and measurement-based

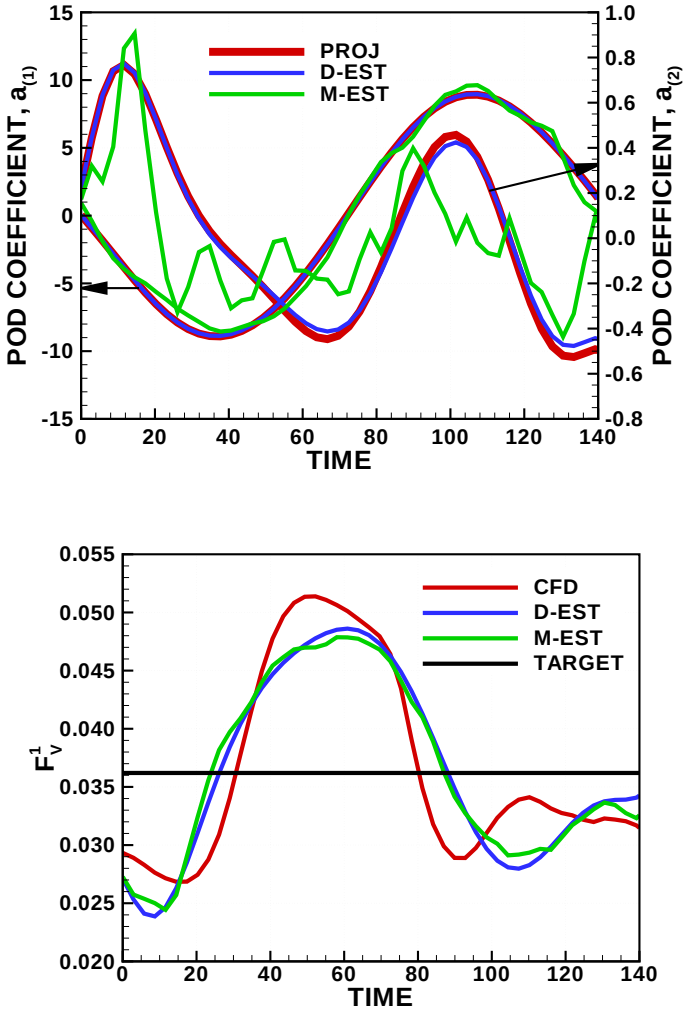

Figure 3.36: In the left panel, comparisons of dynamical and measurement-based state estimates (blue and green curves, respectively) with POD coefficients obtained by projecting CFD solutions onto the POD eigenvectors (red curve). Note that the left vertical axis is the first POD coefficient and the right the second with arrows indicating which curves correspond to the two axes. In the right panel, comparisons of performance output approximations using dynamical and measurement-based state estimates (blue and green curves) with CFD-computed output (red curves).

state estimates in the output approximation of Equation 3.18 (blue and green curves, respectively) with CFD-computed values (red curve). Both low-dimensional approximations are reasonably accurate.

Regulators and Filters

With the control input defined as the time derivative of the unsteady jet ($\dot{u}$), a proportional-integral (PI) regulator is employed in the first set of control-in-the-loop simulations:

$$\dot{u}(t) = K_1 \left[y(t) - y_T \right] + K_2 \int_0^t \left[y(\tau) - y_T \right] d\tau, \tag{3.19}$$

where K_1 and K_2 are the proportional and integral gains, respectively. The unsteady jet velocity is

$$u(t) = \int_0^t \dot{u}(\tau) d\tau, \tag{3.20}$$

providing the time-dependent boundary condition in the CFD model during the control simulations. Choosing $\dot{u}$—rather than u—as the control input has the advantage of "smoothing" the effective jet velocity (u) through the integration operation. The integral term provides additional smoothing of the input, and it also provides a phase shift between input and output. The initial control simulation with CFD-computed output in the loop yielded satisfactory results with the following gain constants: $K_1 = 5.0$ and $K_2 = 0.0$.

Adding a filter to a regulator produces a compensator, capable of "compensating" for both modeling uncertainties and measurement noise. Modeling uncertainties will exist in both the simulations and the experiments. Measurement noise in the CFD simulations, even with DES, is not large, but noise in the wind tunnel pressure measurements is, and a filter must be included in a controller that will operate effectively. A Kalman filter uses both the dynamical and measurement-based estimators jointly to offset errors from each. It weights contributions from the two sources of error in determining levels of compensation that are applied. In systems with low levels of measurement noise and higher levels of dynamical model uncertainty, filter param-

eters impose greater reliance on the measurement-based estimator and less on the dynamical estimator. In systems with more measurement noise, parameters impose less reliance on the measurements and more on the dynamical estimator.

Adding a continuous Kalman filter to the dynamical estimator in Equation 3.14 yields

$$\dot{\hat{\mathbf{x}}} = \mathbf{a}_0 + \mathbf{A}_1\hat{\mathbf{x}} + \ \mathbf{b}_0 u + \mathbf{b}_2\dot{u} + \mathbf{b}_3\dot{\eta} + \mathbf{b}_4\ddot{\eta} + \ \mathbf{K}_f\left(\hat{\mathbf{x}}_m - \mathbf{H}\hat{\mathbf{x}}\right) \tag{3.21}$$

where $\mathbf{H}$ is a sensitivity term, defined here as the unity matrix and $\hat{\mathbf{x}}_m$ is the measurement-based state estimate. The Kalman gain, $\mathbf{K}_f(t)$, provides a means of weighting confidence in the measurement-based state estimate against confidence in the dynamical estimate. Large values of $\mathbf{K}_f(t)$ place more weight on the measurement-based estimate. As $\mathbf{K}_f(t)$ approaches zero, weighting of the dynamical estimate increases. The Kalman gain is defined as

$$\mathbf{K}_f = \mathbf{P}\mathbf{H}^T\mathbf{V}_s^{-1}. \tag{3.22}$$

$\mathbf{V}_s$ is the power spectral density of the error in measurement-based state estimates due to measurement noise:

$$\mathbf{V}_s = \mathbf{B}\mathbf{D}_z\mathbf{V}\mathbf{D}_z\mathbf{B}^T \tag{3.23}$$

where $\mathbf{V} = V_p\mathbf{I}$ is the power spectral density of the measurement noise. $\mathbf{D}_z$ is a diagonal matrix with diagonal entries equal to $\partial f/\partial z|_{z=p_0}$. $\mathbf{P}$ represents the covariance of the measurement-based and dynamical estimates and is determined from the Riccati equation:

$$\dot{\mathbf{P}} = \mathbf{A}_1\mathbf{P} + \mathbf{P}\mathbf{A}_1^T + \mathbf{W} - \mathbf{P}\mathbf{H}^T\mathbf{V}_s^{-1}\mathbf{H}\mathbf{P}. \tag{3.24}$$

$\mathbf{W} = W_p\mathbf{I}$ is the process noise power spectral density, representing modeling uncertainties.

3.4.3 Feedback Control Simulations

Two sets of feedback control simulations were performed: without measurement noise and with measurement noise. In the latter, white noise is superposed on the surface pressure measurements at levels commensurate to noise in the wind tunnel tests in order to develop filter designs that will work effectively in the experiments. Noise must be manually added to the surface pressure signals because DES is capable of capturing only the larger fluctuations in the flow—omitting the small-scale fluctuations that result in measurement noise. Because of this, root-mean-square (rms) values of velocity fluctuations are on the order of five times higher in the wind tunnel than in the detached-eddy simulations.

To define and quantify measurement noise, surface pressure is first decomposed into two parts, the true pressure signal $p_s(t)$ and a noise component $p_n(t)$: $p(t) = p_s(t) + p_n(t)$. The signal-to-noise ratio (SNR) is then defined as SNR $\equiv \langle p_s^2 \rangle / \langle p_n^2 \rangle$ where $\langle \cdot \rangle$ denotes time averaging. Noise levels in the simulation are matched to levels in the wind tunnel by examining the average surface pressure spectrum from a wind tunnel run. The spectrum in Figure 3.37 is computed by averaging data from 18 pressure sensors in the wind tunnel model. Using a cut-off frequency of 500 Hertz, measurements above the cut off are considered noise, and the SNR is computed as the ratio of the area under the signal region to the area under the noise region (marked as green and grey, respectively, in Figure 3.37). Using the areas in Figure 3.37 yields a SNR of 3.77.

Pressure measurements in the CFD simulations are modified to improve the condition number of the measurement estimator. The noise is defined as

$$p_n = \frac{|\hat{p}_1 - \hat{p}_2|}{R_N} \, \xi \tag{3.25}$$

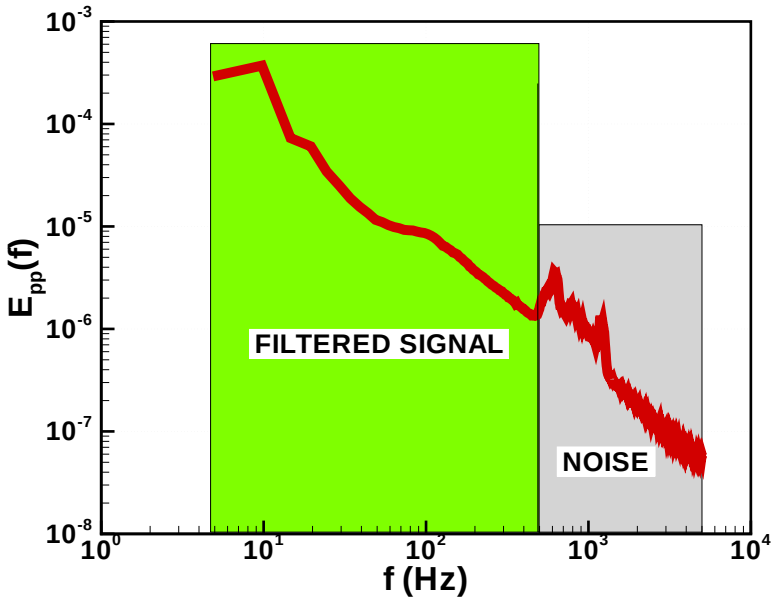

Figure 3.37: Quantification of the signal-to-noise ratio of surface pressures in the wind tunnel experiment. The pressure spectrum is computed with data from 18 sensors. A cut-off frequency of 500 Hertz separates the pressure signal that the controller would use from higher-frequency content that would not be fed back to the controller (marked as the green and grey regions, respectively.

where ξ is a random variate with zero mean and unit variance and $\hat{p}_{1,2}$ are pressure optima. Equating the different definitions of noise used in the simulations and the experiments, an experimental signal-to-noise ratio of 3.77 yields a CFD noise factor of $R_N \approx 4$. To ensure that noise levels are at least as high as noise in the wind tunnel, a value of $R_N = 5$ is prescribed for the control-in-the-loop CFD simulations.

In the first closed-loop-control simulation, noise is not added to the pressure measurements, and the Kalman filter is excluded from the controller. Figure 3.38 contains time histories of performance output (left) and control input (right) from the CFD simulation with no measurement noise. The PI regulator uses output approximations based on the measurement-based estimator exclusively, although CFD-computed val-

ues of output are included in order to evaluate controller performance. The estimator uses eight pressure sensors located on the turret surface. The green curve in the left panel of Figure 3.38 is from the open-loop simulation with a constant suction jet. The purple and black curves are from the model-in-the-loop simulation: purple, the CFD (plant) values of output and black, the model values from the measurement-based estimator (these are the values that the regulator uses to control). The grey curve is from the initial control simulation (also shown previously in Figure 3.35).

Comparing the black and purple curves, the model approximation of output does track the target value closely, but differences exist between the output approximation and plant values. Comparing the purple and green curves, the closed-loop controller provides modest improvements over open-loop control. Comparing the grey and purple curves, using plant values of output in the loop provides tighter control, which is not unexpected. The right panel of Figure 3.38 compares control input (suction jet velocity) from the initial simulation with CFD-computed output in the loop (grey curve) with input from the model-in-the-loop simulation. Tighter control is achieved in the initial simulation through larger variations in suction velocity.

The next set of simulations includes measurement noise, and a Kalman filter is included in the controller. Three simulations were performed with measurement noise, and the parameters that were used in the simulations are listed in Table 3.7. The integral gain is set to zero and the proportional gain is 5 in each. Also, the noise factor (R_N) in each is 5.0, again, comparable to the noise levels in the pressure signals of the wind tunnel tests. The three simulations are distinguished by the assigned values of the filter parameters. The measurement covariance (V_p) appears in Equation 3.24, the Riccati equation, through the power spectral density of error in Equation 3.23, and the process covariance (W_p) and the measurement covariance appears in Equation 3.24 through $\mathbf{W} = W_p\mathbf{I}$. The assigned measurement covariance is 0.003 in each

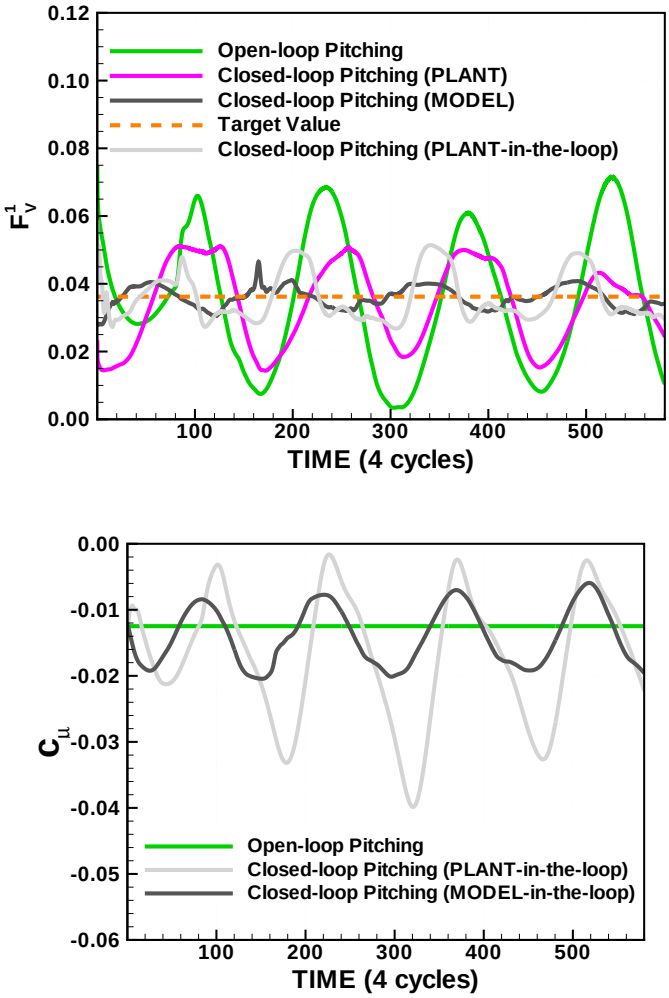

Figure 3.38: Time histories of performance output (left) and control input (right) from the CFD simulations with no measurement noise.

simulation, but the process covariance is assigned as 10 in Run 1, 0.1 in Run 2 and 0.01 in Run 3. Higher values of W_p result in less reliance on (or confidence in) the dynamical estimator and more on the measurements. Therefore, Run 2 places less confidence in the (noisy) measurements than Run 1—and Run 3 even less.

Figure 3.39 contains results from the simulations with measurement noise, along with results from the previous no-noise simulation for comparison. Time histories of

Quantity	Symbol	Run 1	Run 2	Run 3
Proportional gain	K_1	5	5	5
Integral gain	K_2	0	0	0
Signal-to-Noise Ratio	R_N	5.0	5.0	5.0
Process covariance	W_p	10	0.1	0.01
Measurement covariance	V_p	0.003	0.003	0.003

Table 3.5: Parameter settings for the control runs with noise.

output (viscous force on the aperture) from the plant (CFD model) are included in the left panel. These reflect the actual performance of the controllers. Time histories of the output from the estimators are included in the right panel. These are the values that the controllers use to track the output. Comparing the red, green, and orange curves of the right panel indicates that Run 2 does a much better job of filtering the measurement noise than Run 1, and Run 3 does better yet—obviously because the filter is tuned to do so. Comparing the red, green, and orange curves in the left panel, this results in much better controller performance—with Run 3 performing best.

The left panel of Figure 3.40 contains time histories of control input (jet momentum coefficients) from the same set of runs. From the red curve, Run 1 expends more energy in suction even though its performance is poor, highlighting the fact that the Kalman filter can work but must be properly calibrated. The right panel of Figure 3.40 contains time histories of fluctuating velocity (u_{rms}) integrated over a volume of the aperture field of view adjacent to the aperture surface. The extent of control effectiveness of the suction jets is limited to a region near the surface. From the figure, baseline fluctuations in the flow over a stationary turret with no control are 0.1 m/s (black curve), and average fluctuations over a pitching turret with no control are about the same (brown curve). Both the closed- and open-loop controllers reduce average values to approximately 0.06 (blue and cyan curves, respectively). No measurement noise has been added in these two control simulations. The blue and cyan

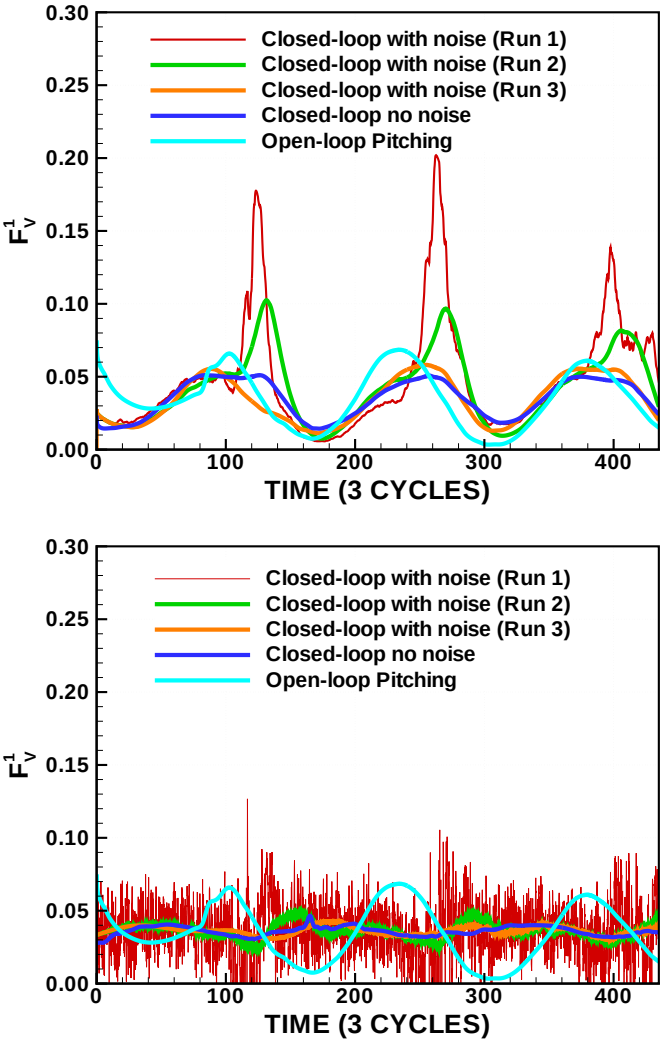

Figure 3.39: Time histories of output from the control-in-the-loop CFD simulations with measurement noise. Results from the simulation with no noise are included for comparison. Output from the plant (CFD model) in the left panel and output from the estimator in the right panel.

curves in the left panel of Figure 3.39 show that tracking of integrated shear stress is slightly tighter with closed-loop control than with open loop, but the blue and cyan curves in the right panel of Figure 3.40 reveal that control of u_{rms} is about the same. Tracking u_{rms} directly, rather than integrated shear stress, would be a logical next step, and this step is taken in the advanced controller design for the wind tunnel

experiments as described in Section 3.4.4.

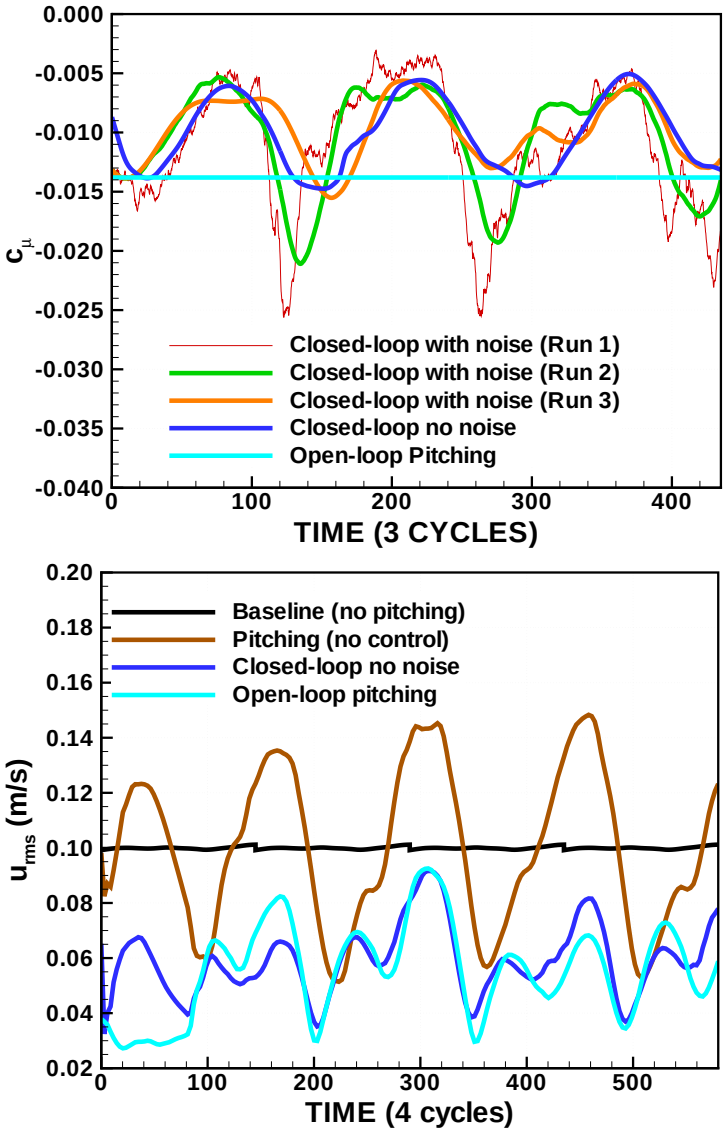

Figure 3.40: Time histories of input from the control-in-the-loop CFD simulations with measurement noise (left panel). Results from the simulation with no noise are included for comparison. Time histories of u_{rms} integrated over a volume of the aperture field of view adjacent to the aperture (right panel).

To compare the cost-effectiveness of closed-loop control, the quantity $\langle c_\mu \rangle$ provides a measure of the energy requirements for control (the jet momentum coefficient

integrated over time), and the quantity (α) is a measure of the energy savings of closed-loop control over open-loop:

$$\langle c_\mu \rangle = \frac{1}{T}\int_0^T c_\mu(t)dt \quad \text{and} \quad \alpha = \frac{|\langle c_\mu \rangle|_{\text{open-loop}} - |\langle c_\mu \rangle|}{|\langle c_\mu \rangle|_{\text{open-loop}}} \times 100\%. \tag{3.26}$$

Table 3.6 summarizes the results. The simulation with measurement noise and a heavy reliance on the dynamical estimator (Run 3) provides the greatest savings: 28.2%.

Run	Energy Cost ($\langle c_\mu \rangle$)	Cost Savings (α) %
Closed-loop with Noise (Run 1)	-0.0114	17.4
Closed-loop with Noise (Run 2)	-0.0106	23.1
Closed-loop with Noise (Run 3)	-0.0099	28.2
Closed-loop with no Noise	-0.0102	26.1
Open-loop	-0.0138	–

Table 3.6: Energy costs and the cost savings of closed-loop control over open-loop.

3.4.4 Wind Tunnel Controller Design

Data obtained from the initial closed-loop run were used to construct an advanced controller that employed a dynamical estimator coupled with a Kalman filter. The advanced controller design is described in detail in Section 3.4.2.

A more robust controller would utilize both velocity measurements and multiple pressure sensors by relying on a general pressure-velocity correlation contained within the measurement-based estimator rather than any specific relationship between surface pressures and velocity. The velocity measurements taken with the PIV at a rate of $4Hz$ were used to construct the measurement and dynamic estimators as well to evaluate controller performance. Although the velocity measurements were not time resolved, the strong correlation between velocity and pressure [28] allows for a time

resolved measurement to further enrich the velocity data set. The single pressure sensor used in the initial closed-loop runs was chosen because it correlated well with pitch angle: pressure variance increased as the angle (and extent of flow separation) increased. The correlation seems to be due primarily to the sensor's location upstream of the jet slots, which will change as the yaw angle changes. The measurement-based estimator in the more advanced controller utilized 18 sensors: Sensor Nos. 1, 2, 3, 5, 6, 8, 11, 12, 13, 14, 15, 16, 17, 18, 25, 26, 29 and 30, identified in the right panel of Figure 2.6(a). These sensors maximize the correlation between pressure and velocity. Pressure sensors that are located on the aperture itself for the purpose of investigating the flows and developing the preliminary controllers; however, these sensors would interfere with operation in real optical applications, and final designs would exclude them.

Experimental Controller Plant

The first step in constructing estimators was to compute a set of POD basis functions using PIV snapshots. The left panel of Figure 3.41 contains the POD energy distributions in the reduced-order model (ROM) built with snapshots obtained from the initial closed-loop run. Four POD modes contain more than 80% of the perturbation energy, and this number of modes is chosen for the estimators. The right panel of Figure 3.41 contains comparisons of time histories of rms velocity fluctuations averaged over 34 sets of three pitching cycles from the PIV data (labeled as "RAW") and time histories obtained by projecting the PIV snapshots onto the four POD modes: $u_{\text{rms}}(t) \approx \sqrt{a_{(n)}(t)a_{(n)}(t)},\ n = 1, 4$. Even with only four modes in the models, the approximations based on projections are very accurate.

The next step is to use the POD models to construct the linear measurement-based and linear dynamical estimators described in Section 3.4.2. Figure 3.42 con-

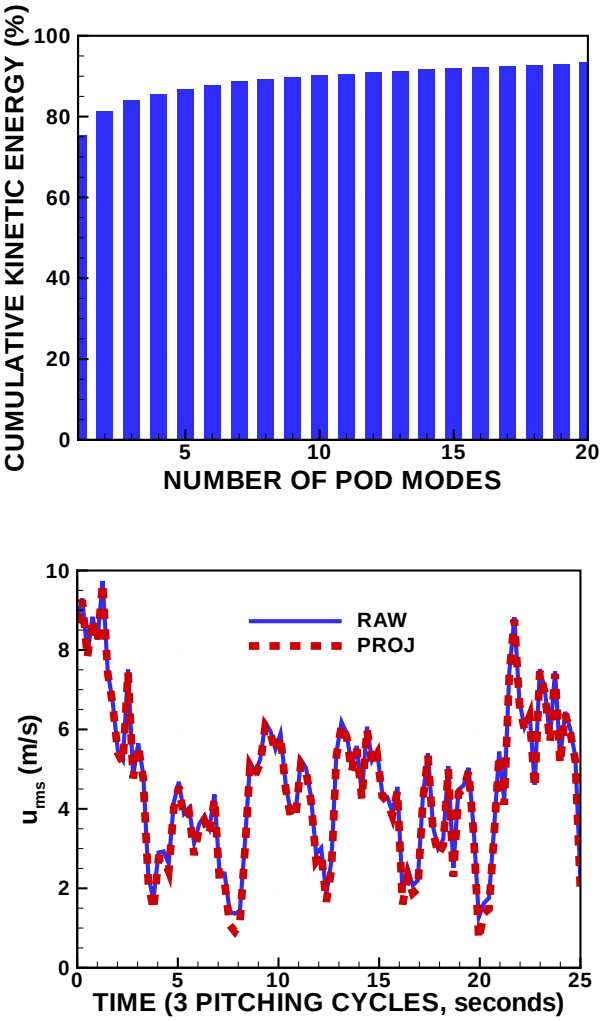

Figure 3.41: Energy distribution in the POD-based ROM (left). Time histories of u_{rms} from the PIV data (RAW) and approximations obtained by projecting the PIV snapshots onto the first four modes in the model (PROJ) (right).

tains time histories of the POD coefficients from the dynamical estimators (D-EST), the measurement-based estimators (M-EST), along with the values obtained by projecting the PIV snapshots onto the four POD modes averaged over 34 sets of three pitching cycles. From the top left panel of the Figure 3.42, predictions from both types of estimator are accurate in predicting the trends in the first POD coefficient,

and this mode contains more than 75% of the perturbation energy. Note how much less noise there is in the dynamical state estimates than in the measurement-based state estimates. This was exploited with the Kalman filter.

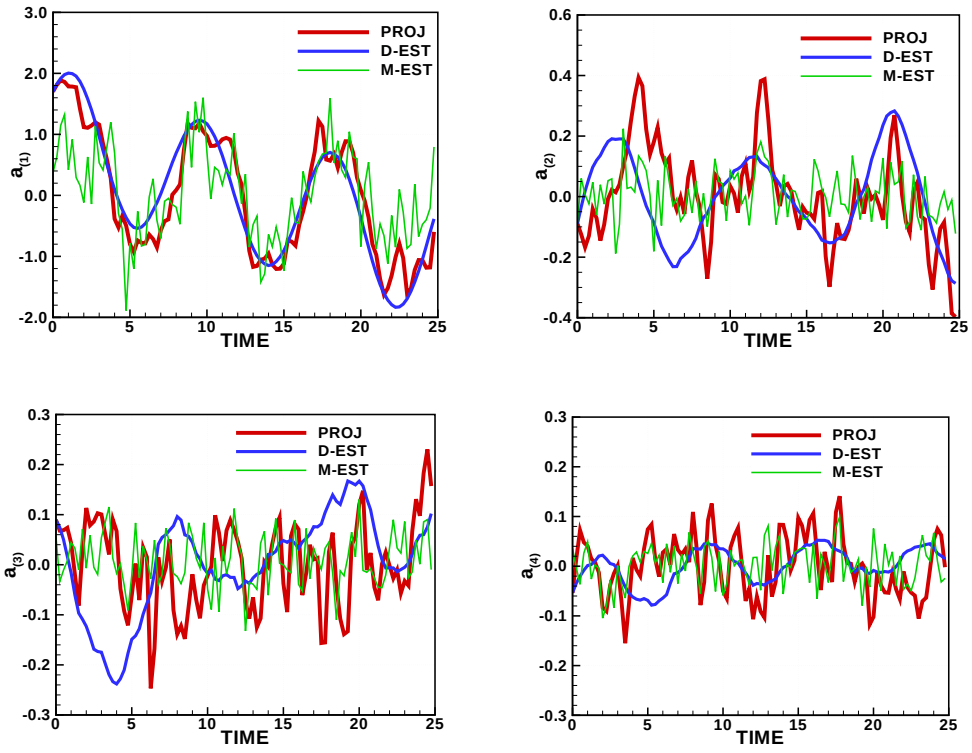

Figure 3.42: Time histories of the first four POD coefficients from the dynamical estimator (D-EST), the measurement-based estimator (M-EST), and values obtained by projecting the PIV snapshots onto the four POD modes of the model (PROJ).

Regulator

As stated above, the control objective in the wind tunnel experiment was to minimize velocity fluctuations in the aperture field of view (or at least over the area of intersection between the PIV window and field of view). Figure 3.43 contains approximations of u_{rms} from the dynamical and measurement-based estimators, along with

values from the projected POD coefficients averaged over 34 sets of three pitching cycles. From Figure 3.43, the dynamical estimator was able to accurately track the velocity fluctuations. The measurement-based estimator exhibits relatively high noise levels, even when the pressure signals are filtered, but the dynamical estimator and Kalman filter were designed to address this issue.

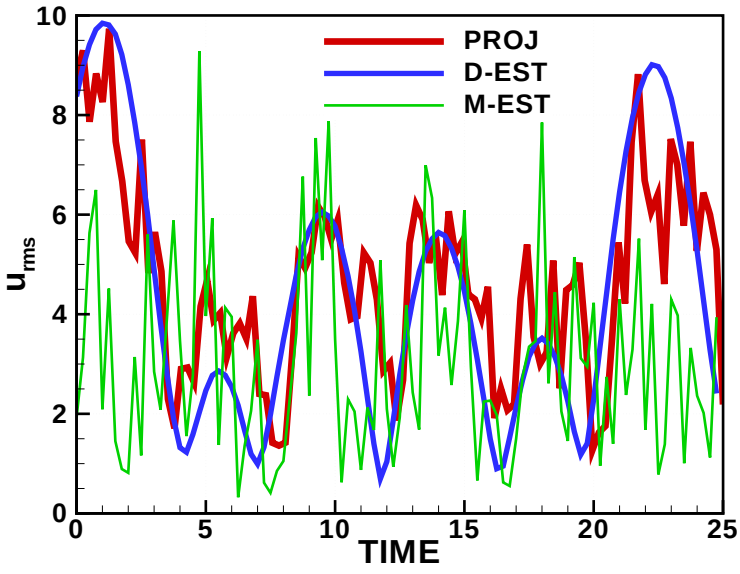

Figure 3.43: Approximations of u_{rms} from the dynamical estimators (D-EST), measurement estimators (M-EST), along with values obtained from projected POD coefficients (PROJ).

With performance output defined as spatially integrated values of $u_{\text{rms}}(t)$, the controller utilized approximations from the estimators, and the PI regulator in Equation 3.19 becomes

$$\dot{u} = k_1(\sqrt{\hat{x}_n(t)\hat{x}_n(t)} - 0) + k_2 \int_0^t (\sqrt{\hat{x}_n(\tau)\hat{x}_n(\tau)} - 0)d\tau \tag{3.27}$$

where u is the suction valve duty cycle percentage and the objective was to reduce

fluctuating velocity to zero. The gains ($k_{1,2}$) are determined heuristically, which can be a time-consuming process involving a number of wind tunnel runs. Alternatively, a Linear Quadratic Regulator (LQR) automatically determines gains that minimize the following cost function:

$$J \equiv \frac{1}{T}\int_0^T (\hat{x}_n \hat{x}_n + r\dot{u}^2)dt. \tag{3.28}$$

The parameter r weights the penalty assigned to the control input ($\dot{u}$).

Next, the dynamical estimator from Equation 3.21 is written as

$$\dot{\hat{\mathbf{x}}} = \mathbf{a}_0 + \mathbf{A}_1\hat{\mathbf{x}} + \mathbf{b}_0 u + \mathbf{b}_2\dot{u} + \mathbf{C}\mathbf{w} \quad \text{and} \quad \dot{\mathbf{w}} = \mathbf{H}\mathbf{w} \tag{3.29}$$

where

$$\mathbf{C} = (\mathbf{b}_3 \;\; \mathbf{b}_4), \quad \mathbf{w} = (\dot{\eta}, \ddot{\eta})^T, \quad \text{and} \quad \mathbf{H} = \begin{pmatrix} 0 & 1 \\ -\omega^2 & 0 \end{pmatrix}. \tag{3.30}$$

ω is the pitching frequency, defined in Equation 3.4. Defining an augmented state estimate as $\mathbf{z} \equiv (\hat{\mathbf{x}}, u, \mathbf{w})^T$ and minimizing the cost function in Equation 3.28 produces the following control law:

$$\dot{u} = -K_m^{LQR} z_m. \tag{3.31}$$

The following gains were computed for the dynamical estimator without the Kalman filter:

$$\mathbf{K}^{LQR} = (-0.2746 \;\; 0.5013 \;\; 0.0482 \;\; -0.0949 \;\; 0.0064 \;\; -1.3309 \;\; -3.2540)^T \times 10^3. \tag{3.32}$$

The gains in Equation 3.32 were computed after reducing the weighting factor r in Equation 3.28 to its lowest possible value, which effectively imposed no penalty on

the control input.

3.4.5 Closed-loop Control Run with an Advanced Controller

Three compensators (LQR regulators with Kalman filters) were designed using three different values of the process covariance while the measurement error covariance (V_p) was set to 3.3×10^{-4}. As the process covariance (W_p) decreased, the controller relied more on the dynamical estimator and less on the measurement-based estimator. From Table 3.7, the process covariance is highest in Run 1 and lowest in Run 3.

Quantity	Symbol	Run 1	Run 2	Run 3
Signal-to-Noise Ratio	SNR	5.0	5.0	5.0
Process covariance	W_p	3.3×10^{-1}	3.3×10^{-4}	3.3×10^{-7}
Measurement covariance	V_p	3.3×10^{-4}	3.3×10^{-4}	3.3×10^{-4}

Table 3.7: Parameter settings for the wind tunnel control runs.

Figure 3.44(b) contains time histories of fluctuating velocity (middle panel) and jet momentum coefficient (bottom panel) from the three control runs, along with baseline histories from the uncontrolled run averaged over 34 sets of three pitching cycles. Comparing the blue, pink, and red curves in the middle panel, it is clear that heavy reliance on the dynamical estimator results in poorer performance. The best control is achieved in Run 1 where the measurement-based estimator dominates. From the pink and red curves in the bottom panel of Figure 3.44(b), the Kalman filter reduces noise in the control input significantly when the dynamical estimator is heavily weighted; however, the blue curve indicates that substantial filtering is effected even in Run 1 when the dynamical estimator is weighted much less: compare the relatively smooth blue curve in the bottom panel of Figure 3.44(b) with the noisy pink curve in the bottom panel of Figure 3.44(a).

From the bottom panel of Figure 3.44(b), the control input modulates with pitch angle in all three runs with the advanced controllers. The phase shift between pitch angle and input varies between the three runs, but the turret motion is clearly driving the input, and modulation in the jet amplitude is not small. Conversely, the pink curve in the bottom panel of Figure 3.44(a) indicates little or no correlation between control input from the simpler controller and pitch angle: modulations in the jet momentum coefficient are essentially random.

Table 3.8 summarizes results from the various runs: time-averaged values of fluctuating velocity, control input ($\langle DC \rangle$), and controller efficiency (ξ)—defined in Equation 3.6. Higher values of ξ correspond to more efficient controllers. Again, the run with a steady suction jet operating at 50% duty cycle is chosen as the representative open-loop case. It effects the largest reduction in fluctuating velocity (57%); however, it is significantly less efficient than the two most efficient closed-loop controllers. The most efficient simple controller (band-pass) reduces fluctuating velocity by 52% and the most efficient advanced controller (Run 1) by 51%.

From the values of ξ in Table 3.8, the advanced controller in Run 1 is 13% more efficient than the most efficient simple controller and 55% more efficient than open-loop control.

Run Description	$\langle u_{\text{rms}} \rangle$	$\langle DC \rangle$ (%)	ξ
No Control	0.182	–	–
Advanced Closed-loop Control (Run 1, $W_p > V_p$)	0.085	30	0.17
Advanced Closed-loop Control (Run 2, $W_p = V_p$)	0.106	40	0.10
Advanced Closed-loop Control (Run 3, $W_p < V_p$)	0.145	41	0.04

Table 3.8: Summary of results from the wind tunnel runs with open- and closed-loop control. ξ in the rightmost column is defined in Equation 3.6 and is a measure of control efficiency—the ratio of fluctuating velocity reduction to required suction.

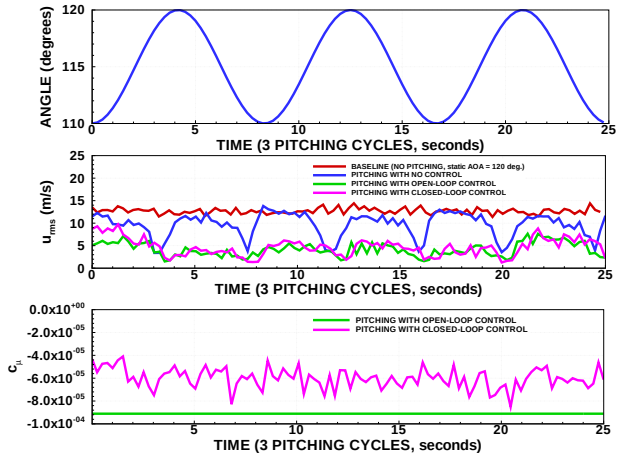

(a) Initial closed-loop control runs

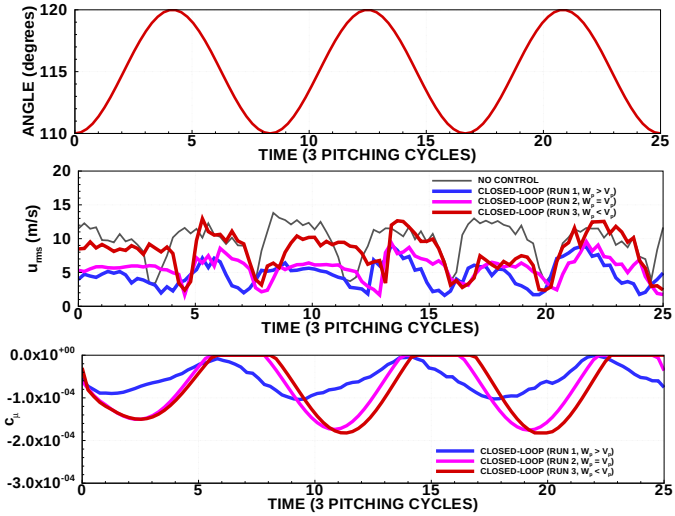

(b) Advance closed-loop control runs

Figure 3.44: Left panel: Comparisons of the baseline (no control), open-loop control, and initial closed-loop control runs. Right panel: Comparison of pitching runs with and without control: results from the new controller.

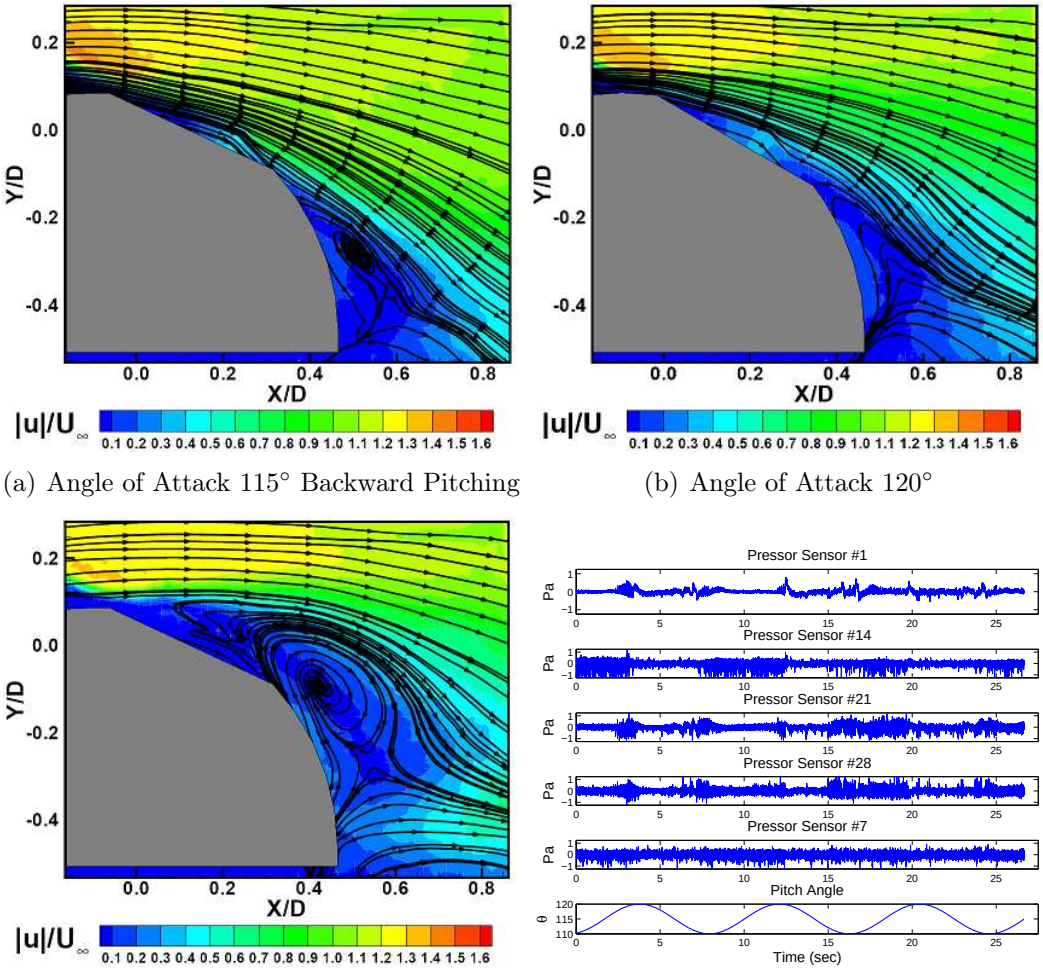

(a) Angle of Attack 115° Backward Pitching

(b) Angle of Attack 120°

(c) Angle of Attack 115° Forward Pitching

(d) Fluctuating Pressure Time Series

Figure 3.45: Velocity contours and streamlines in the PIV centerplane from the run with dynamic pitching and advanced closed-loop control (Run 1) at dynamic pitch angles of 115° (increasing) in the top left panel, 120° in the top right panel, and 115° (decreasing) in the bottom left panel. Time histories of five surface pressures on the turret centerline from the dynamic run in the bottom right panel.

3.5 Summary

In each of the tests it was seen that suction flow control has enough control authority to reduce the wake over the turret.

In the first pitch test the location of the activated suction slots were varied for a

fixed elevation angle. Four different activated slot arrangements were explored: full suction, partial front suction, full front suction, and full back suction. It was found that the separation is sensitive to the location of the control input. For the next set of experiments, a series of fixed elevation angles were examined. The incipient angle was found to be at an angle of 115° and at higher pitch angles the flow was massively separated. This test also set the dynamic pitch range from 110° to 120° back to 110°. Steady suction was applied at each of the fixed elevation angles. The moderate suction amounts reduced the size of the wake while the higher suction amounts was able to reattach the flow.

The effects of the dynamically pitching turret were investigated after the fixed angle experiments. The dynamic pitching turret had a significant affect on the flow. A strong hysteresis developed over the top of the hemisphere, shifting the angle in which separation occurred and delaying reattachment. Applying steady suction reduced the turbulence levels over the aperture. Even at moderate suction amounts, separation was delayed and reattachment was accelerated. To improve upon the efficiency of the control input, a simple proportional feedback controller was implemented within the actuation system. Comparison between spatial u_{rms} and efficiency of the open loop and closed loop control cases is shown in Table 3.9, where $\frac{\langle u_{\mathrm{rms}} \rangle}{U_\infty}$, $\langle DC \rangle (\%)$, and ξ are defined in Section 3.3.2. The closed loop flow control cases obtained similar reductions in the $\langle u_{rms} \rangle$ as the open-loop control but with a lower actuation cost. Figure 3.22 shows the $\frac{\langle u_{\mathrm{rms}} \rangle}{U_\infty}$ for all the control cycle cases.

After exploring the effects that a static and dynamically pitching turret has on the flow, the next series of test examined a dynamically yawing turret. These results are presented in Chapter 4.

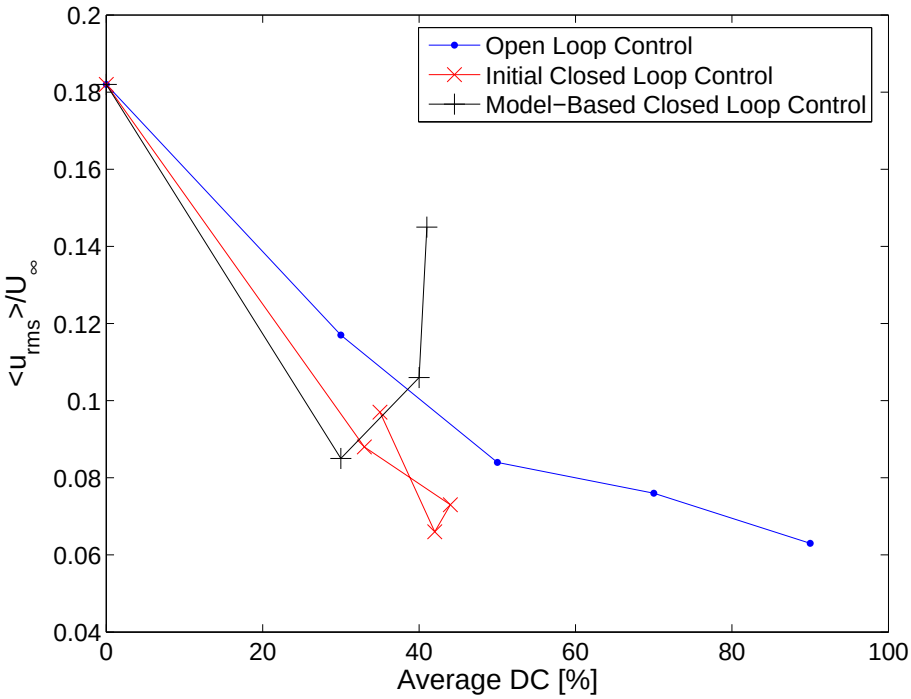

Figure 3.46: All control cases shown for $\frac{\langle u_{\mathrm{rms}} \rangle}{U_\infty}$ versus duty cycle for a pitching turret

Run Description	$\frac{\langle u_{\text{rms}} \rangle}{U_\infty}$	$\langle DC \rangle$ (%)	ξ
Baseline			
0% Duty Cycle	0.182	0	–
Open Loop Control			
30% Duty Cycle	0.117	30	0.12
50% Duty Cycle	0.084	50	0.11
70% Duty Cycle	0.076	70	0.09
90% Duty Cycle	0.063	90	0.07
Closed Loop Control			
Band Pass	0.088	33	0.15
Band Stop	0.073	44	0.13
Low Pass	0.066	42	0.15
Very Low Pass	0.097	35	0.13
Advanced Closed-loop Control (Run 1, $W_p > V_p$)	0.085	30	0.17
Advanced Closed-loop Control (Run 2, $W_p = V_p$)	0.106	40	0.10
Advanced Closed-loop Control (Run 3, $W_p < V_p$)	0.145	41	0.04

Table 3.9: Summary of baseline, open loop control, and closed loop control results from the dynamically pitching turret.

Chapter 4

Flow Control of a Yawing, Three Dimensional Turret

The next series of tests examined the effect of the flow due to the hemisphere rotating in the azimuthal direction (β) or the yaw direction. Both open-loop and closed-loop control experiments were performed in an attempt to reduce the turbulence levels over the aperture of the turret as the hemisphere yawed.

4.1 Dynamically Yawing Turret Hemisphere Parameters

For one yaw cycle, the range is set from 0° to 10° back to 0° at three different elevation angles (α): 110°, 115°, and 120°. The hemisphere is rotated at a rate of $\omega = 2.4$ deg/s in a sinusoidal manner, similar to the pitching motion, defined in Equation 4.1.

$$\beta(t) = \left[5 - 5\cos(\frac{\omega}{\pi}t)\right] \tag{4.1}$$

The yaw rate was provided by the Air Force. The non-dimensional rotation rate is $\varpi = 0.00192$ based on Equation 4.2.

$$\varpi = \frac{\omega D}{360° U_\infty} \tag{4.2}$$

The non-dimensional rotation rate is a function of turret diameter D, rotation rate ω, freestream velocity U_∞, and maximum rotation range. Figure 4.1 shows a visualization of the yaw range, sensor location, and PIV window.

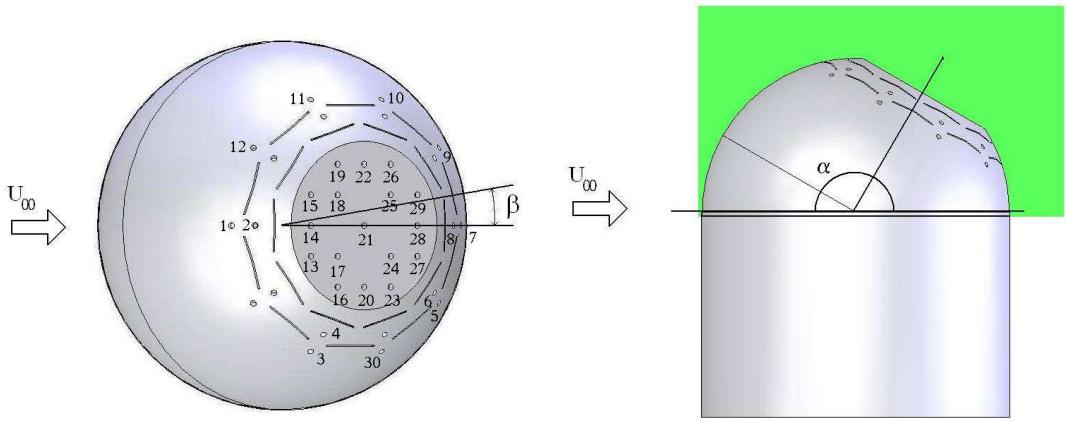

(a) Yaw range and sensor locations (b) PIV window location

Figure 4.1: Yaw range, sensor location, and PIV window of the yawing hemisphere.

Although three elevation angles are explored in this study, only the results for 115° are discussed here in this paper.

4.2 Baseline Flow over the Dynamically Yawing Hemisphere

Data were collected with no suction actuation as the hemisphere yawed in a sinusoidal fashion at the three fixed pitch angles. This motion gave rise to asymmetric flow over

the top of the hemisphere.

Figure 4.2 contains mean velocity magnitude contour plots at the centerline plane of the turret, at a pitch angle of $\alpha = 115°$ and five yaw angles (β) as the turret rotates in a sinusoidal fashion: 0°, 5° clockwise, 10°, 5° counter-clockwise, and 0°. The velocity field is phase averaged over 102 yaw cycles. The low velocities above and just downstream of the aperture reflect separated flow. At the centerline, the flow was continuously separated throughout the yaw cycle.

As the hemisphere rotates through its yaw cycle, the aperture becomes off axis and causes an asymmetric flow to develop over the top of the hemisphere. The asymmetry can be seen in the fluctuating surface pressure over the top of the aperture. Figure 4.3 contains time histories of the fluctuating surface pressure from five sensors on the turret's aperture: Sensors 14, 20, 21, 22, and 28. At the start of the rotation cycle the amplitude of the fluctuating pressure is small in each of the time history panels, indicating that flow is separated on both sides of the aperture. On the left side of the aperture, the fluctuating pressure amplitude increases then decreases as the hemisphere continues through the yaw cycle. The trend in Figure 4.3(a) implies that the level of separation was lower on the left side of the aperture. Looking at surface pressure signals on the right side of the aperture in Figure 4.3(b), the amplitude remains small. Thus, at the center and on the right side of the hemisphere the flow remained massively separated over the aperture throughout the cycle.

The spectra of the centerline, fluctuating surface pressure are seen in Figure 4.3(e). The spectra were ensemble averaged over 500 blocks of 2048 data points. In the frequency range below $70Hz$, each signal closely lay upon each other. Sensor 14 and 21 have a roll off at $70Hz$ and continue to laid upon each other until a frequency of about $150Hz$ while, Sensor 28 has a roll off at $300Hz$. Each sensor has sharp distinct peaks from $550Hz$ to $2050Hz$ at $300Hz$ intervals. These peaks correspond

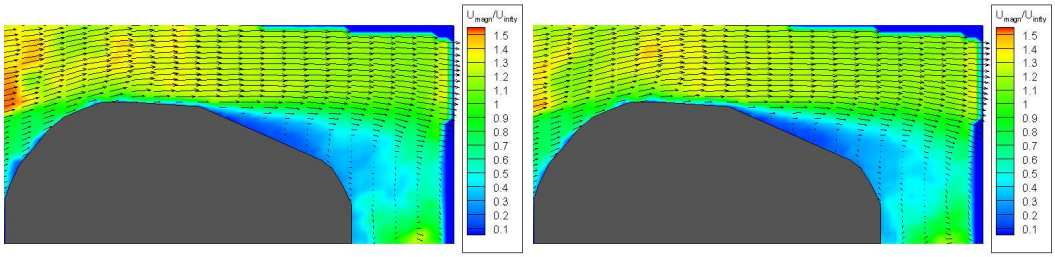

(a) $\beta = 0°$, Start of cycle

(b) $\beta = 5°$ CW

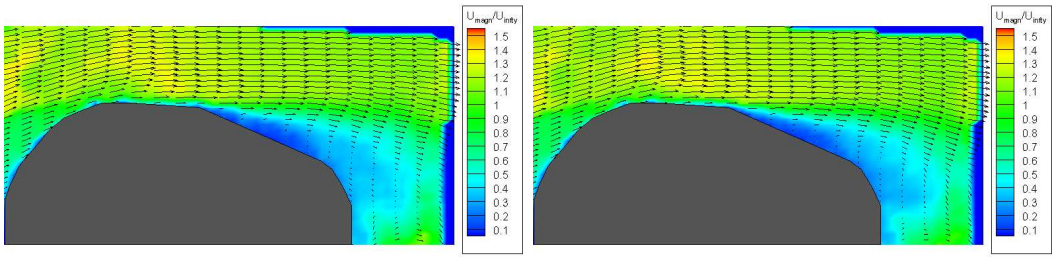

(c) $\beta = 10°$

(d) $\beta = 5°$ CCW

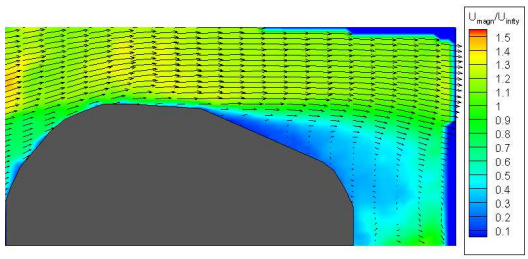

(e) $\beta = 0°$, End of cycle

Figure 4.2: Normalized mean velocity magnitude ($\langle\sqrt{\tilde{u}_1^2 + \tilde{u}_2^2}\rangle/U_\infty$) contours and mean velocity vectors of baseline yawing turret.

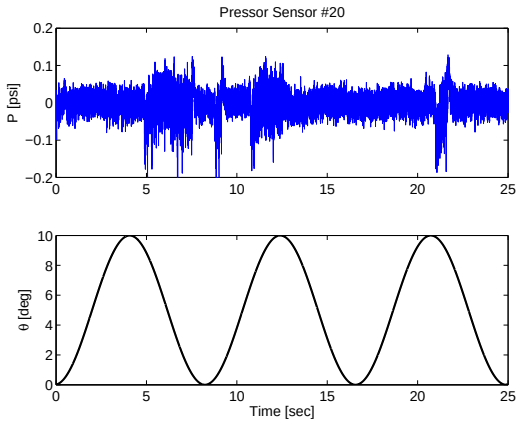

(a) Sensor No. 20

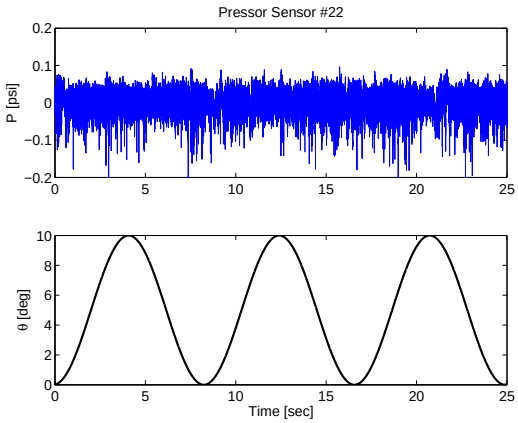

(b) Sensor No. 22

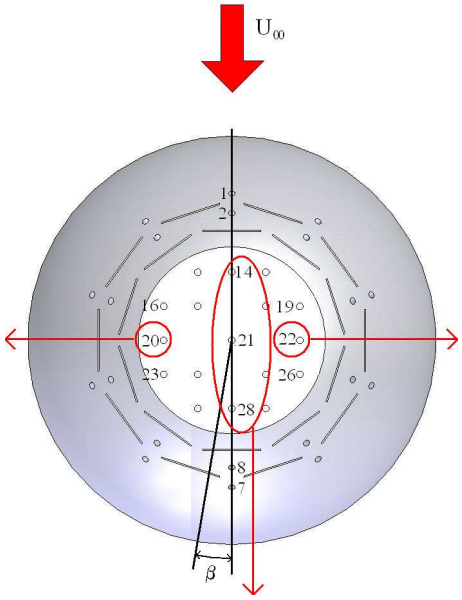

(c) Sensor Locations

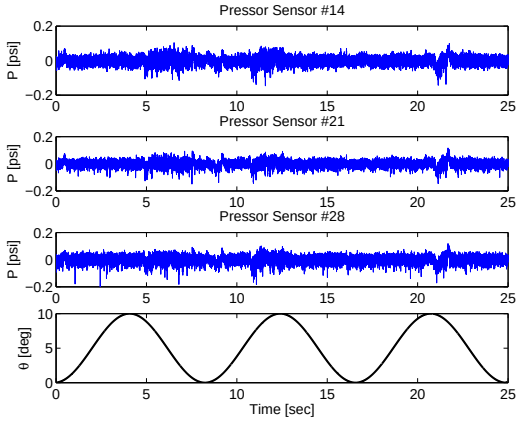

(d) Sensor No. 14, 21, and 28

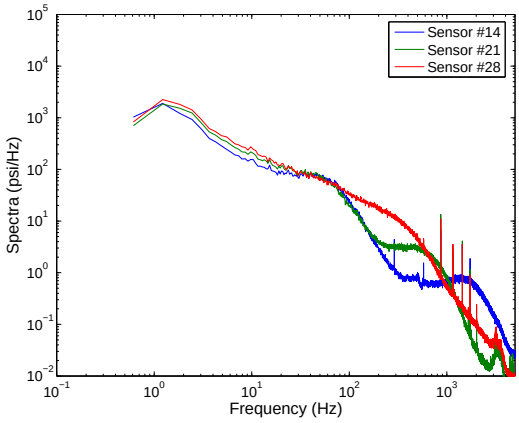

(e) Sensor No. 14, 21, and 28 Spectra

Figure 4.3: Fluctuating surface pressure time series for the baseline case. The freestream flow is from top of the page to the bottom.

to shedding structures over the aperture. Sensor 14 has additional sharp peaks at $300Hz$, which implies that the structure which is associated with this peak was altered as it convected downstream.

Figure 4.4 presents the spectra of the fluctuating surface pressure across the aperture. The spectra from the front row of sensors are seen in Figure 4.4(a). The signals lay upon each other until about 70Hz when the signal slightly shift in frequency and amplitude from each other. The asymmetry of the flow at the leading aperture sensors occurred due to the small scaled structures within the flow. In the middle of the aperture the spectrum in Figure 4.4(c) was slightly shifted in both the amplitude and frequency. Spectra of the trailing edge sensors closely fall on each other, as seen in Figure 4.4(d). This trend represents a well mixed flow across the aperture.

The time modulations in the surface pressures reflected the sinusoidal variation in yaw angle, and differences between the pressures in the left and right panels reflect the asymmetry induced by the non-zero yaw angles.

4.3 Open Loop Flow Control over the Dynamically Yawing Hemisphere

The next set of experiments examined the performance of open-loop control systems, utilizing steady suction while the hemisphere was dynamically yawing. The purpose of studying the effect of the steady suction is to answer the question if suction flow control will reduce the fluctuating velocity over the aperture.

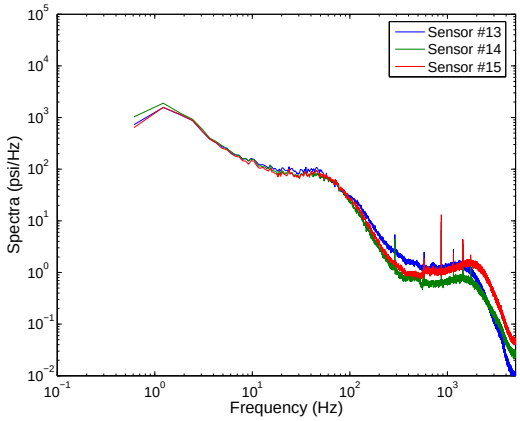

(a) Front Sensors

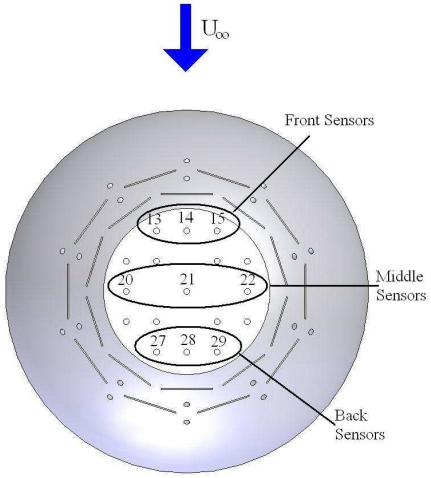

(b) Sensor Location

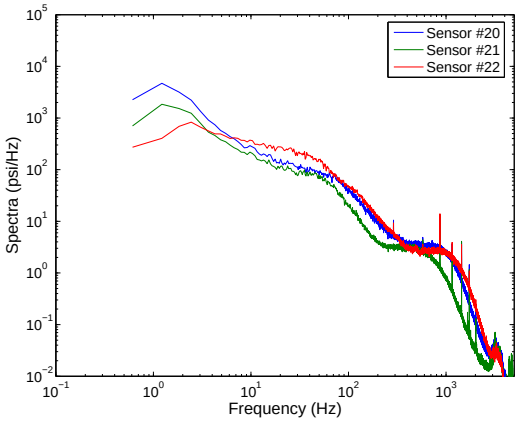

(c) Middle Sensors

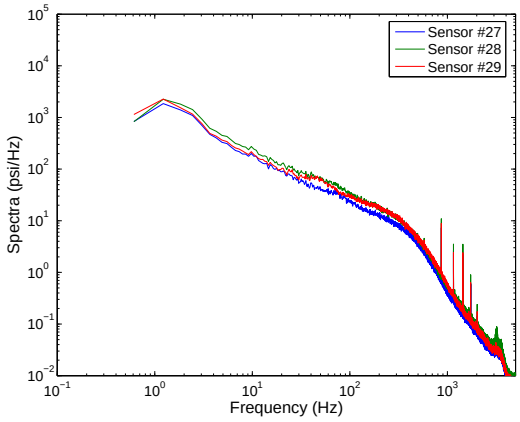

(d) Back Sensors

Figure 4.4: Spectrum of the off center fluctuating surface pressure with no control. The freestream flow is from top of the page to the bottom.

4.3.1 Open Loop Flow Control Parameters

In all of the open-loop tests, the solenoid valves that control suction velocity on the left and right sides of the turret operate in unison, so that actuation is symmetric about the aperture of the turret. The valves are cycled at 25 Hz with a constant duty cycle of 50%. At 50%, the duty cycle produces an average suction of $C_\mu = 0.875 \times 10^{-4}$, according to Equation 2.3.

4.3.2 Open Loop Flow Control Results

Figure 4.5 contains contour plots of the normalized mean velocity magnitude ($\langle\sqrt{\tilde{u}_1^2 + \tilde{u}_2^2}\rangle/U_\infty$) at the centerline plane as the turret rotates sinusoidally through its yaw cycle. Although the flow remains separated, the size of the wake was reduced at various yaw angles. Comparison of the baseline flow in Figure 4.2 and the flow with open-loop control in Figure 4.5 indicates only marginal changes: the flow remains separated at the centerline of the turret. At the extreme yaw angle of 10° the separation seemed to have reached its maximum wake size reduction.

Further evidence that steady suction altered the flow state over the aperture can be seen in Figure 4.6. Figure 4.6 shows the three fluctuating surface pressure times series signals at the centerline of the aperture: Sensor Numbers 14, 21, and 28. At the centerline of aperture the hemisphere rotates towards $\beta = 10°$, the amplitude of the fluctuating surface pressure remained consistent until the hemisphere reached $\beta = 10°$ and started moving back to $\beta = 0°$. When the hemisphere reached the elevation angle of $\beta = 10°$, the amplitude of the fluctuating surface pressure doubled until the hemisphere reached $\beta = 2°$. The pressure signals shown in Figure 4.6 indicate that the state of the flow over the aperture briefly goes from separated to attached and back to separated during the yaw cycle.

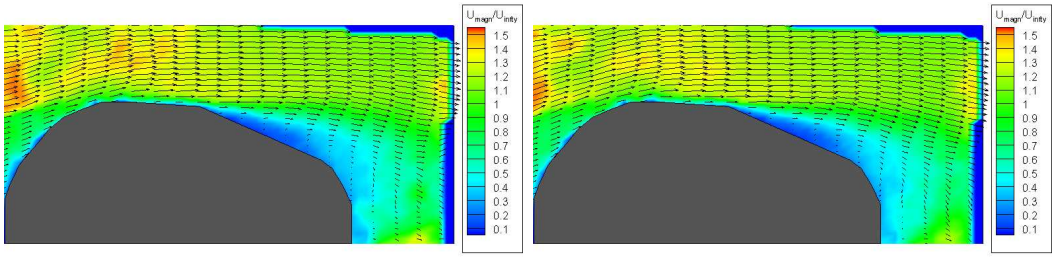

(a) $\beta = 0°$, Start of cycle

(b) $\beta = 5°$ CW

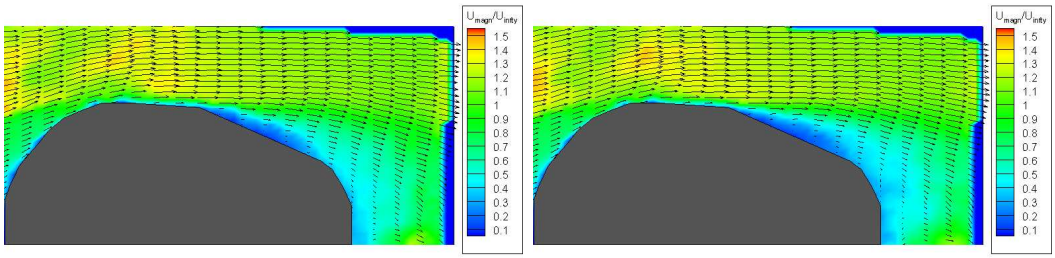

(c) $\beta = 10°$

(d) $\beta = 5°$ CCW

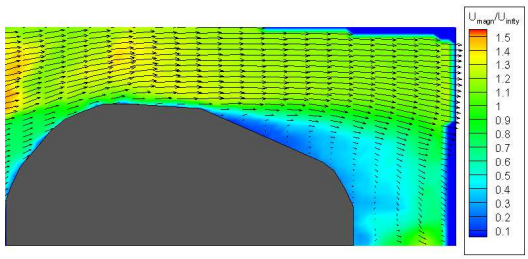

(e) $\beta = 0°$, End of cycle

Figure 4.5: Normalized mean velocity magnitude ($\langle\sqrt{\tilde{u}_1^2 + \tilde{u}_2^2}\rangle/U_\infty$) contours and mean velocity vectors of a yawing turret using open-loop flow control.

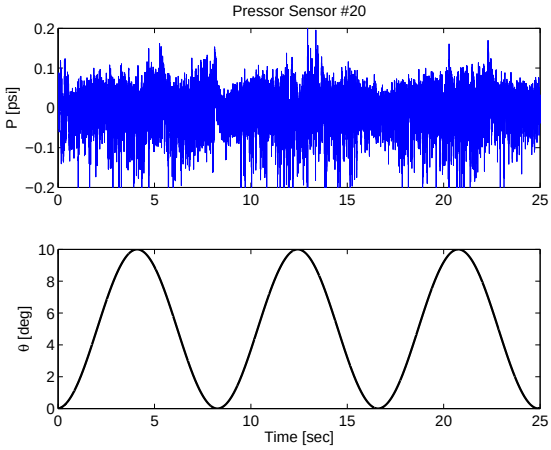

(a) Sensor No. 20

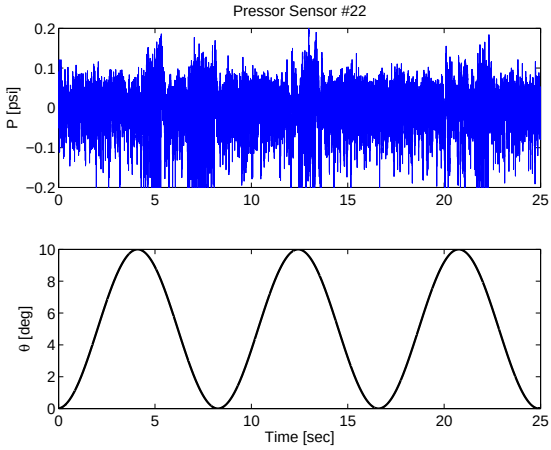

(b) Sensor No. 22

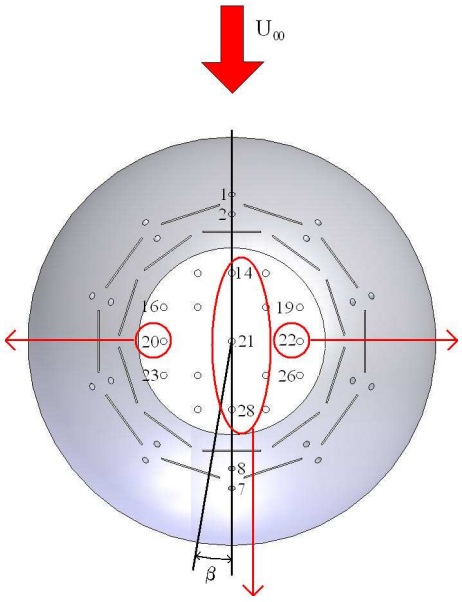

(c) Sensor Locations

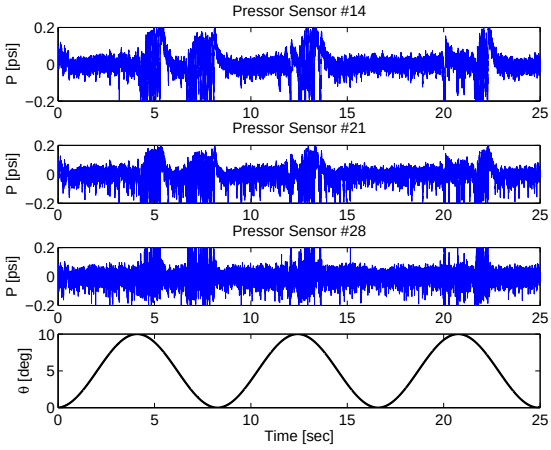

(d) Sensor No. 14, 21, and 28

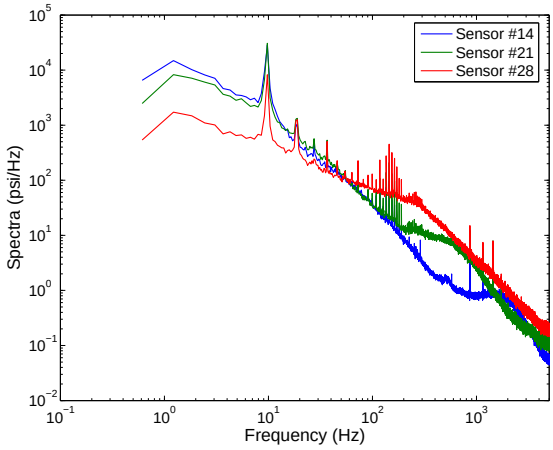

(e) Sensor No. 14, 21, and 28 Spectra

Figure 4.6: Fluctuating surface pressure time series and spectra at the center on the aperture for the open loop control case. The freestream flow is from top of the page to the bottom.

The spectrum for the centerline pressure is seen in Figure 4.6(e). A decrease in the spectra amplitude is seen in the low frequencies up to 50 Hz going from Sensor 14 to 21. This indicates that the number of large scale structures decreased as flow convects downstream. At 10 Hz a sharp peak is sensed by each sensor. This peak represents the control input from the suction actuation. Within the range of 80 Hz to 200 Hz sharp peaks exist for each sensor that resembles a strong harmonic excitation.

Looking at the spectra of the middle pressure sensors, shown in Figure 4.4(c), reveals more of the actuation's affect across the aperture. The sharp peaks seen in Figure 4.6(e) are also seen in Figure 4.4(c), indicating that the structures generated by the control input were present across the aperture. The spectrum of Sensor 20 and 22 fall closely upon each other in the higher frequencies suggesting that the flow on each side of the aperture have similar structures.

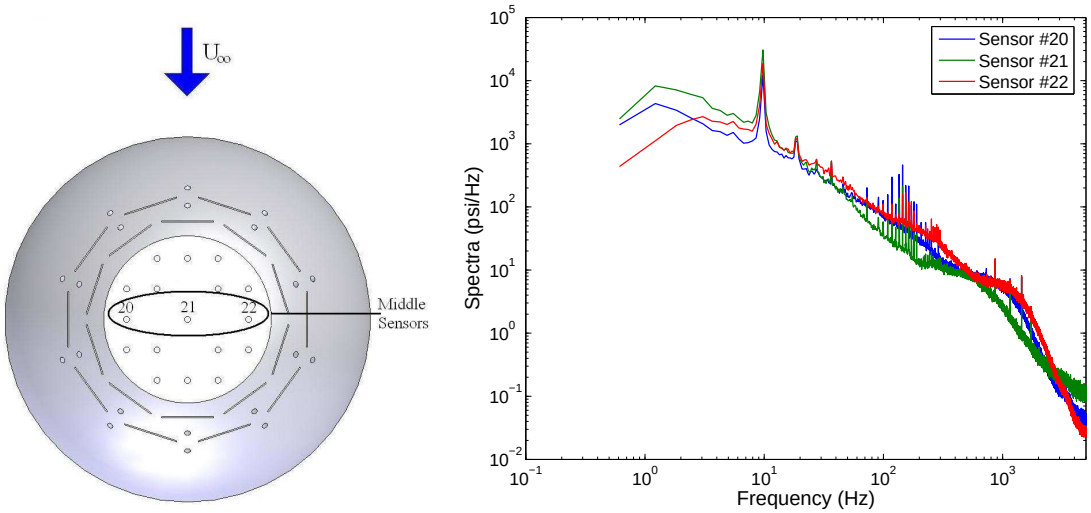

(a) Sensor Location

(b) Middle Sensors

Figure 4.7: Spectrum of the off center fluctuating surface pressure with open loop control.

Like in Section 3.3.2, the performance of the control input can be defined as the spatial velocity rms, $\langle u_{rms} \rangle$. Change in $\langle u_{rms} \rangle$ corresponds to the change in fluctuating

velocities. The $\langle u_{rms} \rangle$ can be found by integrating Equation 3.1 over the velocity field. The first column in Table 4.1 shows the $\langle u_{rms} \rangle$ for both the baseline and open loop unsteady suction modulation cases, the open-loop controller reduces the average velocity fluctuations by approximately 21%. Also in Table 4.1 is the efficiency, ξ, of the open-loop controller which was found to be 0.04. ξ is defined in Equation 3.6, where higher values of ξ correspond to higher efficiency: greater reductions in velocity fluctuations and/or lower required control input.

Run Description	$\frac{\langle u_{\mathrm{rms}} \rangle}{U_\infty}$	$\langle DC \rangle$ (%)	ξ
No Control	0.195	0	–
Open-loop Control	0.153	50	0.04

Table 4.1: Summary of baseline and open loop control results from the dynamically yawing turret at an angle of attack of 115°.

Comparing the centerline surface pressure of the open loop unsteady suction modulation case, Figure 4.6, to the baseline case, Figure 4.3(d), shows distinct differences within the two. The amplitude of the surface pressure at the angles between 10° to 2° for steady suction case was 2.3 times greater than the baseline case. Therefore, one can clearly see that steady suction aided in the reduction of the separation levels over the aperture of the turret.

4.4 Multiple Input Multiple Output Control System

Although the incoming flow was steady and uniform, the effects due to the dynamic yawing of the hemisphere, shown in Section 4.2, caused an asymmetric flow over the top of the aperture. Therefore, the amount of control authority needed to reattach the flow over the aperture is not only a function of time, but location as well. A feedback closed-loop controller was designed by employing a Multiple Input Multiple

Output control system to improve the performance of the actuation system to account for the asymmetric flow. The closed-loop feedback control system performance was then analyzed to determine if using an adaptive flow control scheme would further reduce the turbulence level over the aperture more efficiently than the open loop case in Section 4.3.

4.4.1 Closed-loop Controller Design

The overall goal is to reduce the near field aero-optic effects generated by the density fluctuations within the turbulent regions of the flow over the aperture. Again, a direct way of controlling the density fluctuations is to control the velocity fluctuations. The control objective for the closed-loop feedback system is to drive the fluctuating velocity towards zero using a measurement estimator based proportional controller.

The controller for the closed-loop feedback system consists of a low-dimensional measurement-based estimator and a simple proportional regulator. The measurement-based estimator is designed to provide the controller with information about the flow in real time and to be computationally efficient. The estimator employs a low dimensional representation of the flow that can be fed back in real time using both velocity field and fluctuating surface pressure measurements of the flow.

The PIV system provides a direct spatially resolved measurement of the velocity field. The velocity field obtained from the PIV system is not practical as a feedback signal due to the fact that the measurements are not temporally resolved, large computation cost to obtain the velocity field in real time, and the PIV system itself is difficult to mount and operate on actual flight systems. Surface pressure measurements, on the other hand, are capable of time resolved measurements, minimally intrusive, and easy to mount.

Up to this point the actuation system has been run in unison for both open-loop and closed-loop flow control tests. In order to build a control system that is able to adapt to the asymmetry caused by the dynamic yawing, the controller is set up to send individual feedback signals to each half of the suction slots. The slots are equally divided into two separate zones and each zone is controlled by one valve. According to Figure 3.1: the left zone contains Slot 4, 5, 6, 7, 8, 13, 14, 15, 16, and 17, while the right zone contains Slot 1, 2, 3, 9, 10, 11, 12, 18, 19, and 20. Along with the suction slots being separated into zones, the pressure sensors are also separated into two zones. The pressure sensors are divided along the centerline of the hemisphere: the left zone contains Sensors 3, 5, 13, 20, 27, and 30, while the right zone contains Sensors 9, 10, 11, 15, 22, and 29.

The low-dimensional measurement-based estimator is constructed using the complementary technique with the velocity and surface pressure from the baseline, dynamic yawing case. The complementary technique takes advantage of strengths of both velocity and pressure measurements to give an accurate description of the flow. Employing the complementary technique, described in Section 1.4, a correlation between the surface pressure measurements and velocity based time dependent POD coefficients is calculated to derive a low dimensional estimate of the flow.

The first step in building the low-dimensional measurement-based estimator is to calculate the time dependent, velocity POD expansion coefficients, a_n. The correlation tensor is computed with Equation 4.3, and the orthogonal eigenfunctions, $a_n(t)$, are found with Equation 4.4.

$$C(t,t') = \frac{1}{T}\int_D u_i(\vec{x},\beta,t)u_i(\vec{x},\beta,t')d\vec{x} \tag{4.3}$$

The 'snapshot' correlation tensor is represented as $C(t,t')$, T is the total number of

PIV images, β is the yaw angle, and D is the spatial domain. A correlation tensor is found for each yaw angle. The correlation tensors are then 'lumped' together or integrated together in the eigenvalue problem in Equation 4.4.

$$\sum_{k=1}^{T} \frac{1}{T}[\int_{\tau} C(t,t') \cdot a_n(t')dt'] = \lambda^n a_n(t) \tag{4.4}$$

The integration of the correlation tensor is over the temporal domain of τ consisting of T number of snapshots. With the eigenfunctions determined, the POD expansion coefficients are found using Equation 4.5

$$\phi_i^n(\vec{x}) = \frac{1}{T\lambda^n} \int_{\tau} a_n(t) u_i(\vec{x}, \beta, t)dt \tag{4.5}$$

Work done by Ausseur [8] showed that the first mode obtain from the POD contained sufficient information about the flow to describe the state of the flow. Figure 4.8 shows the energy of distribution of the POD modes. Only the first mode was retained in the construction of the measurement estimator, since the first mode represented 68% of the total energy in the system. Closed loop control work done by Andino et al. [5] examined feeding back various amount of POD modes to a flow control system. This work found that feeding back the first POD mode performed just as well as feeding back the first 18 modes of the POD (representing 99% of the energy). Feeding back more modes would not necessary improve the closed loop control system of the turret.

Next, the a_n obtained from the POD and fluctuating surface pressure, p_j, are implemented into the $mLSM$. The pressure sensor location is represented as j. For

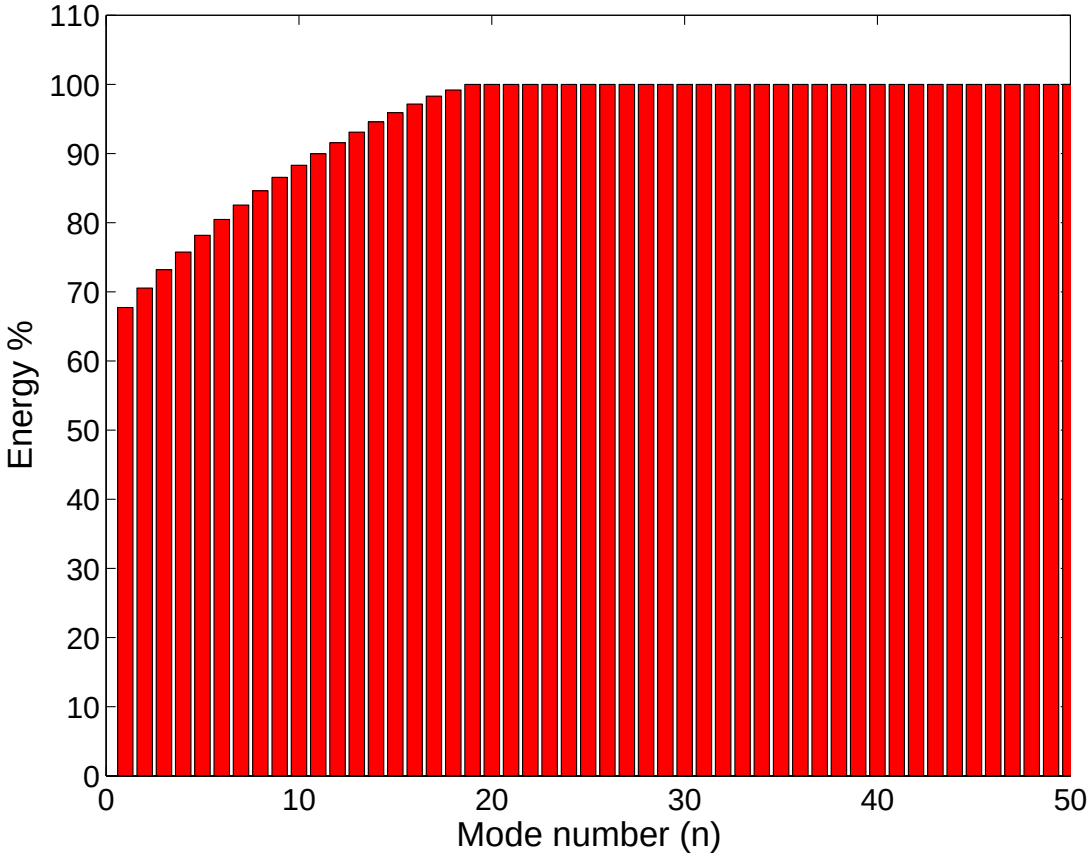

Figure 4.8: Energy distribution of the POD modes.

each side of the turret, a separate $mLSE$ correlation was computed.

$$\langle p_j(t_s)p_j(t_s)\rangle A_{nj,L} = \langle a_n(t_s)p_j(t_s)\rangle \quad j = 3, 5, 13, 20, 27, 30 \tag{4.6}$$

$$\langle p_j(t_s)p_j(t_s)\rangle A_{nj,R} = \langle a_n(t_s)p_j(t_s)\rangle \quad j = 9, 10, 11, 15, 22, 29 \tag{4.7}$$

The a_n and p_j are correlated together and divided by the pressure tensor $\langle p_j(t_s)p_j(t_s)\rangle$, giving the $mLSM$ expansion coefficients, A_{nj}.

The duty cycle of the valve controlling suction to the slots on the left of the PIV plane is set to be proportional to the $mLSM$ based on sensors on the left, $A_{nj,L}$; the duty cycle of the valve controlling flow to the slots on the right is set to be proportional to $mLSM$ based on sensors on the right, $A_{nj,R}$.

Since two feedback signals are sent from the same controller but the left and right zones are not linked together, the system is classified as a decoupled multiple-input-multiple-output (MIMO) closed loop control system. The decoupled MIMO system can also be denoted as two single-input-single-output (SISO) closed loop control systems. Figure 4.9 contains the block diagram for the feedback controller. A fluctuating

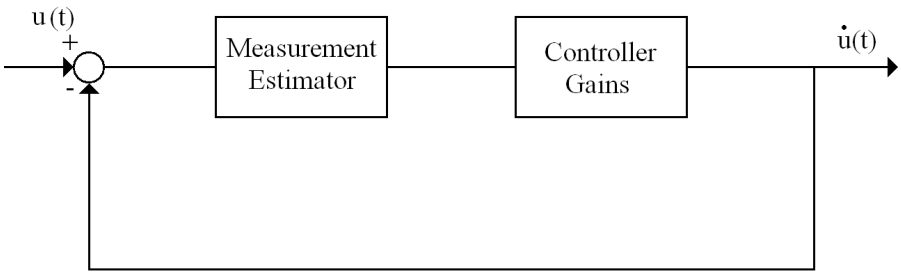

Figure 4.9: Block diagram of the closed-loop controller.

velocity of zero would correspond to POD coefficients $a_n = 0$, which would also lead

to a $mLSM$ coefficients of $A_{1j,L} = 0$ and $A_{1j,R} = 0$. The feedback error, ϵ, for both zones that corresponds to the controller objective (defined earlier) is described in Equation 4.8.

$$\epsilon = A_{1j} \tag{4.8}$$

The control law is described in Equation 4.9,

$$\dot{u} = \begin{cases} KA_{1j,L} & 0 < t < \mathcal{T}A_{1j,L} \\ KA_{1j,R} & 0 < t < \mathcal{T}A_{1j,R} \\ 0 & \mathcal{T}A_{1j,L} < t < \mathcal{T} \\ 0 & \mathcal{T}A_{1j,R} < t < \mathcal{T} \end{cases} \tag{4.9}$$

where $\dot{u}$ is the control input, K is the controller gains, $\mathcal{T}$ is one signal actuation period equal to 0.04 seconds, and A_{nj} are the Complementary Technique expansion coefficients. The controller gains were set to amplify the feedback signal between 0 to 100% duty cycle, therefore $K = 1200$.

4.4.2 Closed-loop Control Results

The closed-loop controller described in Section 4.4.1 was evaluated in a series of wind tunnel runs.

The top panels of Figure 4.10(a) and 4.10(b) contains the feedback signal time history for both the left and right zones respectively, while the yaw angle is shown in the bottom panels of Figure 4.10. Comparing the top and bottom panels, the amplitude of the feedback signal increased as the yaw angle increased. The trend of the amplitude of the feedback signal seems to correspond well to the yaw angle. There does not appear to be a time lag between duty cycle and yaw angle, which

is consistent with proportional control and also indicates that the flow response to changes in the yaw angle is high. The average duty cycle, $\langle DC \rangle$, for the left controller

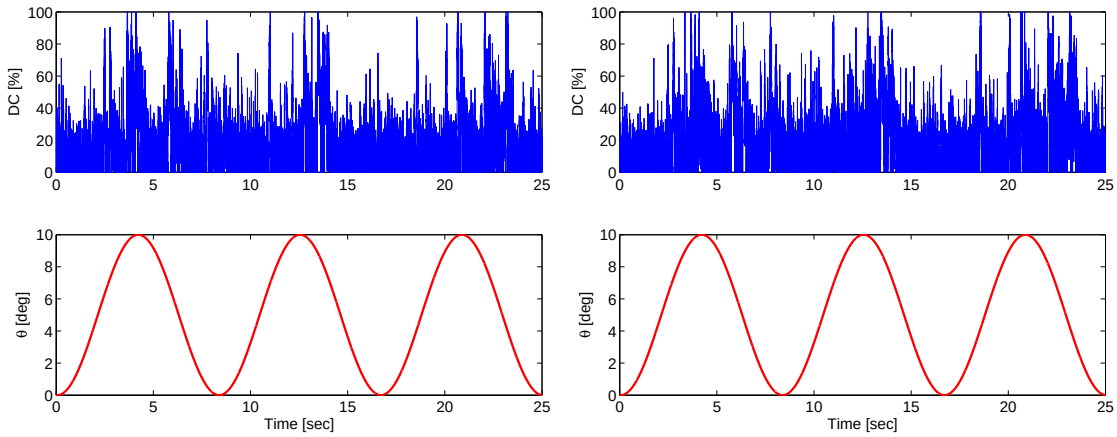

(a) Left Control Signal (b) Right Control Signal

Figure 4.10: Feedback control signals time series for three pitch cycles.

was 35.3% and for the right controller was 41.5%. Thus, the control system fed back a higher amplitude signal for the side which experiences the higher turbulence levels.

The contour plots of the normalized mean velocity magnitude for the closed loop control case are shown in Figure 4.11. The size of the wake region behind the turret was reduced in Figure 4.11 as compared to both the baseline flow (Figures 4.2) and the flow with open-loop control cases (Figure 4.5).

Shown in Figure 4.12 are closed-loop time histories of the fluctuating surface pressure from five sensors on the turret aperture. The time modulations in the surface pressures reflect the sinusoidal variation in yaw angle to an even greater degree than they did in the baseline and open-loop-control runs. On both left and right sides of the aperture, the amplitude of the pressure fluctuations increased as the hemisphere approached the maximum yaw angle of $\beta = 10°$. The amplitude of the pressure remained high until as the hemisphere rotated clockwise back to about $\beta = 5°$ where the amplitude of pressure decreased. The centerline pressure signal revealed a similar

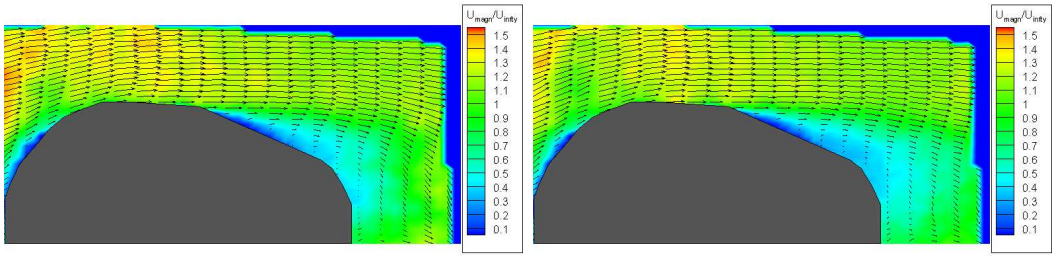

(a) $\beta = 0°$, Start of cycle

(b) $\beta = 5°$ CW

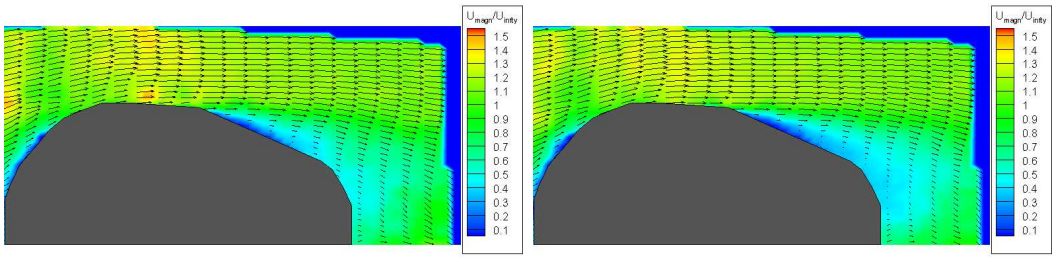

(c) $\beta = 10°$

(d) $\beta = 5°$ CCW

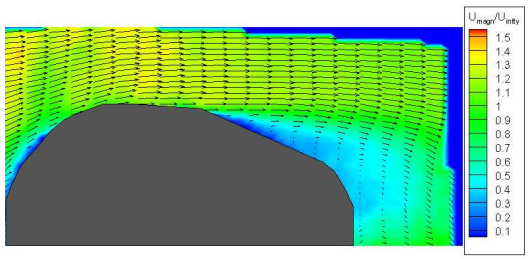

(e) $\beta = 0°$, End of cycle

Figure 4.11: Normalized mean velocity magnitude ($\langle\sqrt{\tilde{u}_1^2 + \tilde{u}_2^2}\rangle/U_\infty$) contours and mean velocity vectors of a yawing turret using closed-loop flow control.

trend. The closed loop control was able to generate a symmetric pressure field over the aperture than the baseline case.

Shown in Figure 4.13(b) is the spectrum for the middle pressure sensors: 20, 21, and 22. Above $20Hz$ the spectra of each sensor collapses upon each other, thus indicating an improved mixing in the flow and a more symmetric flow. Comparison of the close loop case in Figure 4.13(b) to the open loop case in Figure 4.7(b) showed that the closed loop control had greater collapse of the spectra than the open loop control.

Run Description	$\frac{\langle u_{\mathrm{rms}} \rangle}{U_\infty}$	$\langle DC \rangle$ (%)	ξ
No Control	0.195	0	–
Open-loop Control	0.153	50	0.04
Closed-loop Control	0.111	38	0.12

Table 4.2: Control effectiveness and efficiency of the open- and closed-loop systems.

Table 4.2 contains the comparisons between open- and closed-loop control using the normalized spatial u_{rms} as the performance index. Comparison of the efficiency of the actuation system, ξ, defined in Equation 3.6, for each control case is also contained in Table 4.2. Clearly, the closed-loop controller is more effective—reducing turbulence levels by 43% (versus a 21% reduction with open-loop control). Moreover, the average actuation level is lower (38% versus 50%)—resulting in an efficiency three times higher than the open-loop system.

A comparison of the surface pressure spectrum of the middle aperture sensors for each control case is shown in Figure 4.14. Examination of the spectra comparison shows a significant change between the baseline and both open and closed loop control cases. A significant increase in spectra amplitude was achieved with each controller. The peak associated with the control input was shifted from $10Hz$ for the open loop control case to $11Hz$ for the closed loop control case. In the low frequency range

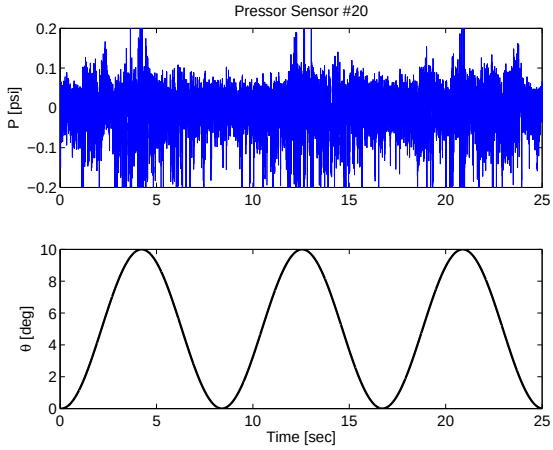

(a) Sensor No. 20

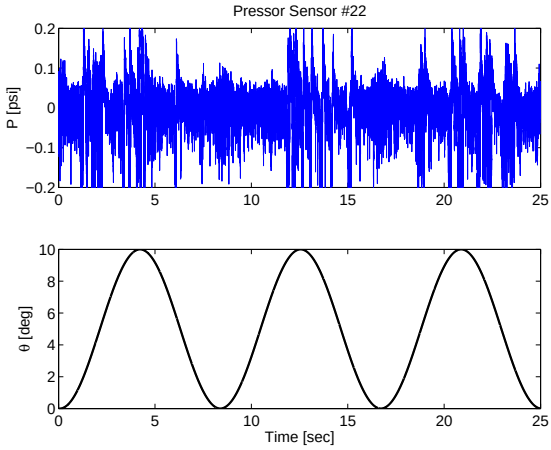

(b) Sensor No. 22

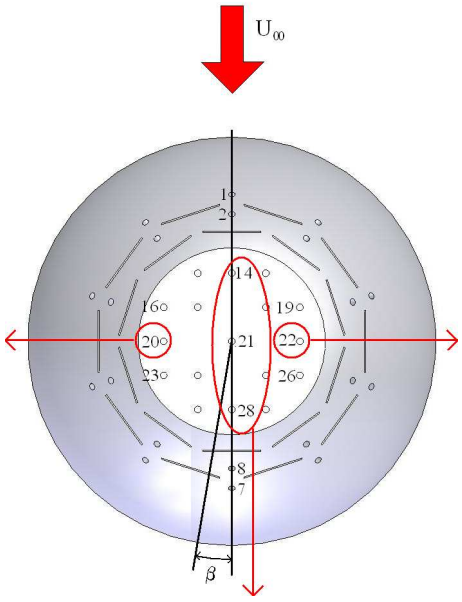

(c) Sensor Locations

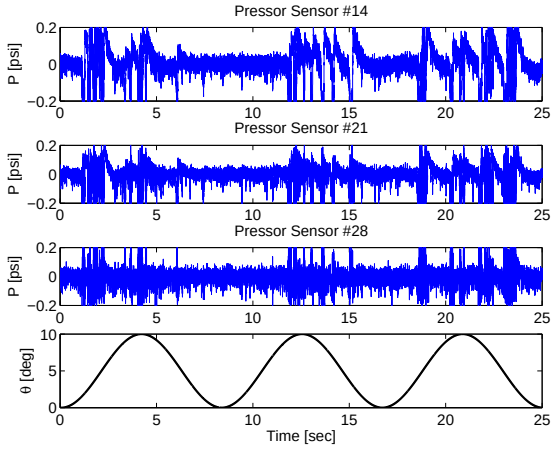

(d) Sensor No. 14, 21, and 28

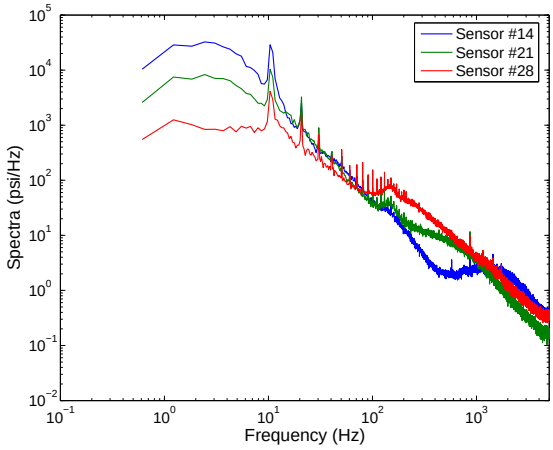

(e) Sensor No. 14, 21, and 28 Spectra

Figure 4.12: Fluctuating surface pressure time series and spectrum at the center on the aperture for the closed-loop control case.

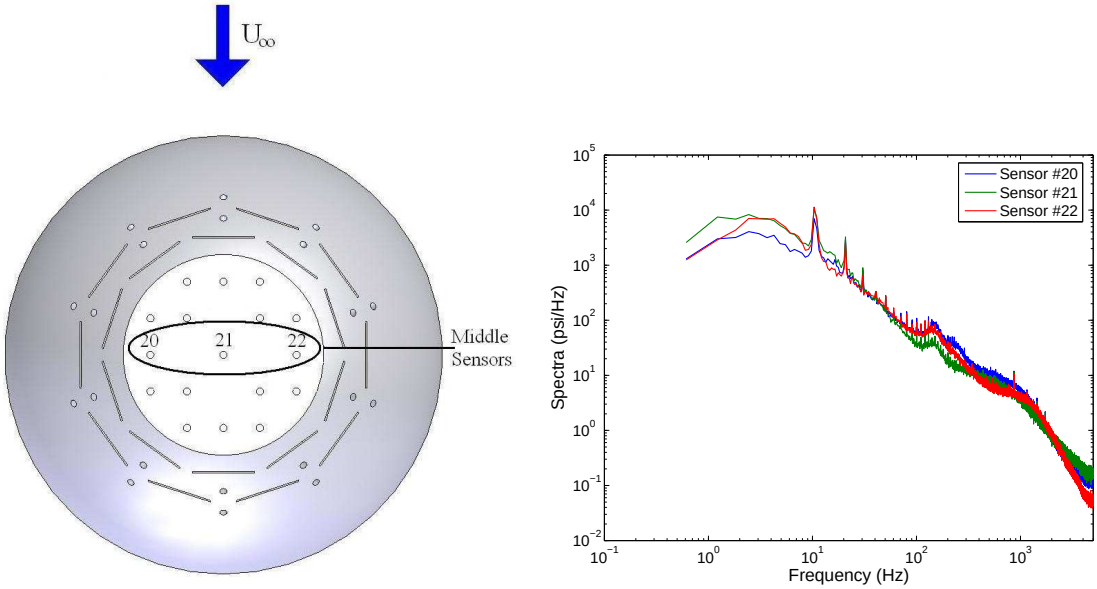

(a) Sensor Location (b) Middle Sensors

Figure 4.13: Spectrum of the off center fluctuating surface pressure with closed loop control. The freestream flow is from top of the page to the bottom.

below $50Hz$ the closed loop control had a broader band frequency response than the open loop control. The sharp peaks in the frequency range from $50Hz$ to $200Hz$ seen in the open loop control were not present in the closed loop control case. On the other hand, the sharp peaks in the higher frequency range did not shift in each control case just in the spanwise location.

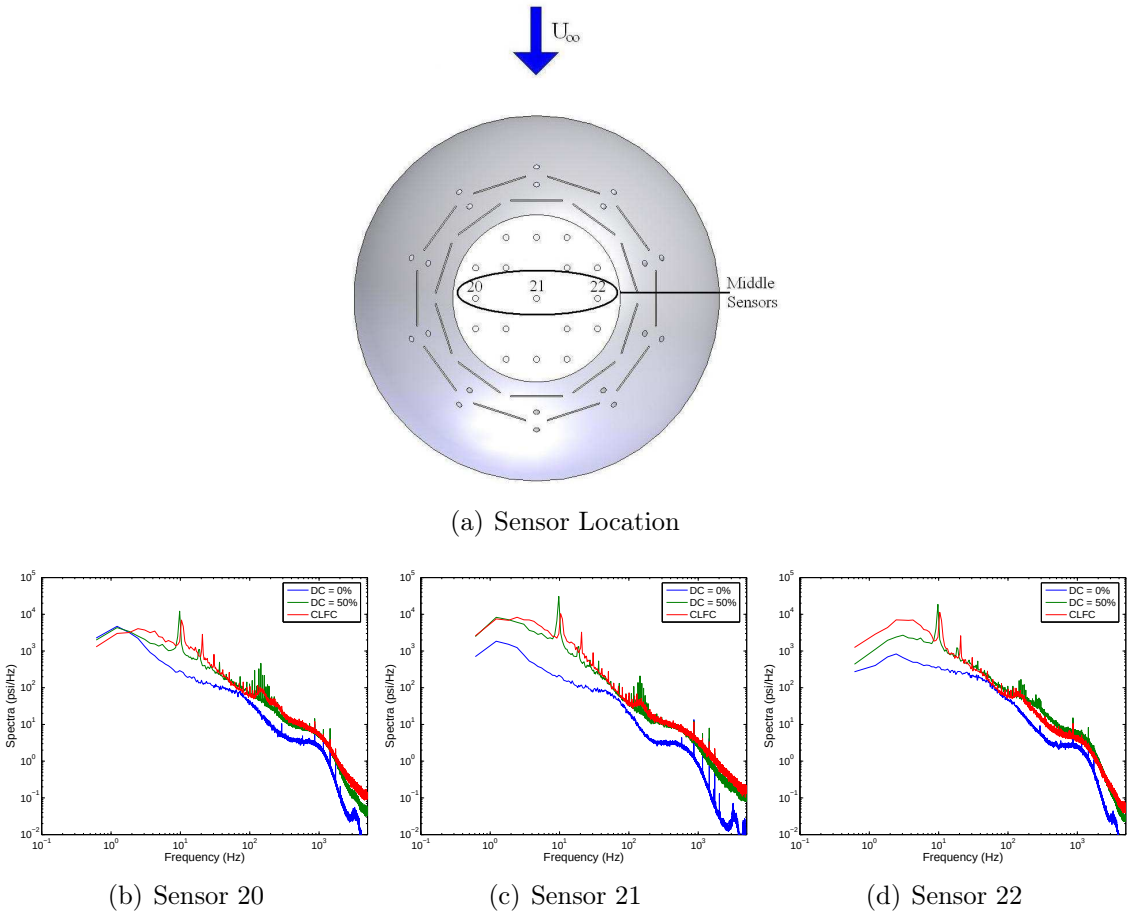

(a) Sensor Location

(b) Sensor 20 (c) Sensor 21 (d) Sensor 22

Figure 4.14: Spectrum at the middle sensors on the aperture for the various control cases.

Although the zones are not linked in this control system, the system was effective at reducing the velocity fluctuations. By linking the zones would add another level of sophistication to the control.

4.5 Summary

The hemisphere of the turret was dynamically yawed to investigate the effects of the flow due to this motion. The flow became highly asymmetric over the top of turret due to the dynamic yawing motion. For open loop control the valves were run in unison at 50% duty cycle. Steady suction was able to moderately reduce the velocity fluctuations over the aperture.

A simple proportional, multiple-input-multiple-output controller was implemented in the actuation system. The controller utilized a measurement estimator to determine the velocity fluctuations and feedback a proportional signal to the valves. In order to compensate for the asymmetry in the flow, the actuation system was setup so that each valve controlled half of the suction slots of the turret. Multiple pressures signals were fed into the control system to modulate the two valves independently of each other. The closed loop flow control system was able to reduce the velocity fluctuation more effectively than the open loop control.

Table 4.3 shows the performance at all the elevation angles.

The next series of experiments examined the flow over a scaled up turret in a compressible flow and at a high Reynolds number.

Run Description	$\frac{\langle u_{\mathrm{rms}} \rangle}{U_\infty}$	$\langle DC \rangle$ (%)	ξ
$\alpha = 110^\circ$			
No Control	0.181	0	–
Open-loop Control	0.127	50	0.06
Closed-loop Control	0.094	34	0.13
$\alpha = 115^\circ$			
No Control	0.195	0	–
Open-loop Control	0.153	50	0.04
Closed-loop Control	0.111	38	0.12
$\alpha = 120^\circ$			
No Control	0.189	0	–
Open-loop Control	0.171	50	0.02
Closed-loop Control	0.159	46	0.05

Table 4.3: Control effectiveness and efficiency of the open- and closed-loop systems for all elevation angles.

Chapter 5

Aero-Optic Measurements at High Reynolds in Compressible Flow

Additional suction flow control experiments were performed in the Subsonic Aerodynamic Research Laboratory (SARL) wind tunnel at Wright-Patterson Air Force base. This afforded an opportunity to collect direct aero-optic effect measurements over a three dimensional turret in a compressible flow and high Reynolds number. The freestream velocity was set at the minimum Malley probe operational speed of Mach 0.3. At this velocity, the Reynolds number is approximately 2,000,000, based on the diameter of the turret, according to Equation 1. Figure 5.1(a) shows the SARL turret model in the wind tunnel.

5.1 Multiple Static Pitch Angles

Before the aero-optic measurements were taken, velocity and fluctuating surface pressure data were obtained without suction control at various elevation angles from 90° to 120° and at an azimuthal angle of 0°. These measurements established a baseline at the each of the static elevation angles. Although the velocity data are not available to present in this paper because of ongoing error reduction processing of the PIV images due to particle seed dropout within the images, the fluctuating surface pres-

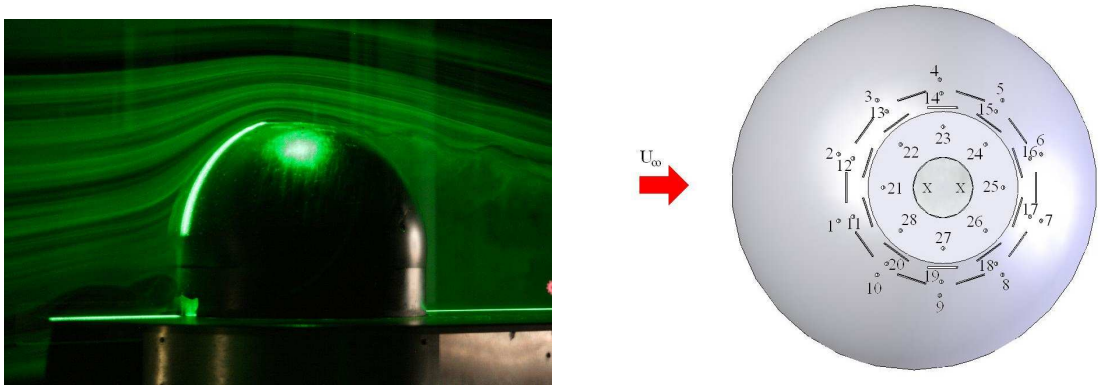

(a) Turret configuration (b) Pressure sensors and Malley probe location

Figure 5.1: SARL test article setup.

sure measurements provide insight to the flow over the turret at the various elevation angles.

The fluctuating surface pressure from the outer ring of pressure sensors on the apertures (Sensors 21 to 28 in Figure 5.1(b)) is quantified with the spatial $\langle p_{rms} \rangle$ at each elevation angle. The spatial fluctuating surface pressure rms ($\langle p_{rms} \rangle$) is defined as the integration of the fluctuating surface pressure rms (p_{rms}) from various pressure sensor locations. The p_{rms} from a sensor signal is defined in Equation 5.1,

$$p_{rms,i} = \sqrt{\frac{\sum p_i(t)^2}{n_{sample} - 1}} \tag{5.1}$$

where p is the fluctuating surface pressure, n_{sample} is the number sample points, and i represented pressure sensor locations from 21 to 28. The p_{rms} for each sensor was taken over 50,000 sample points. Figure 5.2 shows the $\langle p_{rms} \rangle$ at each elevation angle from 90° to 120°. On the aperture, the $\langle p_{rms} \rangle$ increased as the elevation angle was increased until the flow reached $\alpha = 95°$. The drop in $\langle p_{rms} \rangle$ from 95° to 100° indicates that flow transitions from attached to separated within this range of elevation angles.

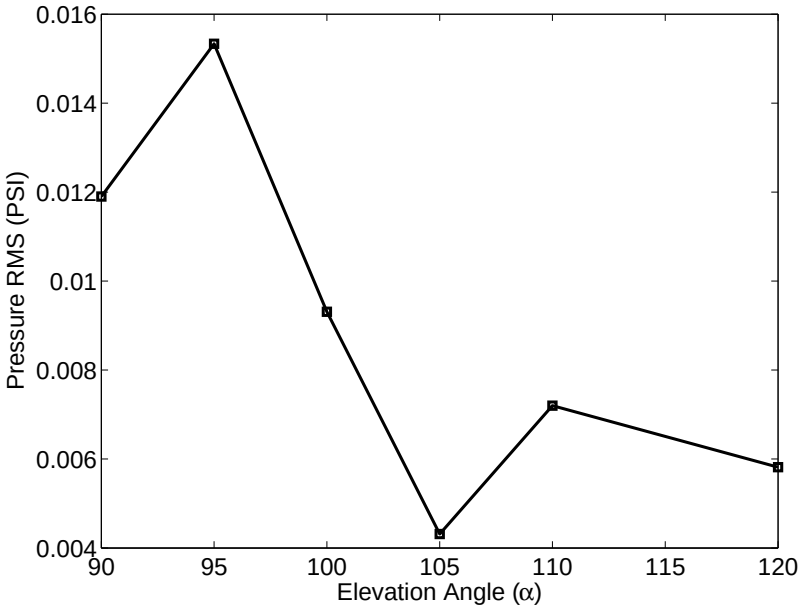

Figure 5.2: Spatial averaged surface $\langle p_{rms} \rangle$ on the aperture.

As the elevation angle is increased to 100° the $\langle p_{rms} \rangle$ decreases even further, implying that the flow becomes massively separated.

A more in depth look at the pressure field over can be achieved by transforming the fluctuating surface pressure from the time domain into the frequency domain. Figure 5.3 shows the pressure spectra for the various elevation angles at four locations on the aperture of the turret: Sensors 21, 23, 25, and 27. For each sensor the spectra were averaged over 500 blocks consisting of 2048 sample points. Figure 5.3(a) shows the spectra for the leading sensor on the aperture (Sensor 21). The elevation angles of 90° and 95° show a gradual decrease in the spectra with sharp peaks at about $200Hz$ and $600Hz$. These peaks occur at all elevation angles indicating that the corresponding structure is present at all elevation angles. The elevation angles of above 95° lay closely upon each other. At 100°, 105°, and 110° additional sharp peaks occur at the frequencies of $400Hz$, $700Hz$, and $1500Hz$ and have a roll off at $2500Hz$. The extreme angle of 120° does show a difference in the frequencies above $400Hz$. The spectra that this angle is increased has a broad band response with a roll off at $2000Hz$. The shift in the spectra as elevation angle is increased clearly showed that the flow over aperture became separated between 95° to 100°. The spectra of Sensors 23 and 27 are seen in Figure 5.3(b) and 5.3(c) respectively. The elevation angles in which the flow is attached have a flat frequency response with broad band peaks at $800Hz$ and 2500. For the separated flow elevation angles the spectra has a roll off at $500Hz$. Slight differences in the spectra of Sensor 23 and 27 implies that there appears to be an asymmetric flow over the aperture.

Comparison of Figures 5.3(a) and 5.3(a) shows evolution of the flow as it convects downstream.

The dramatic difference between the spectra of Sensors 21 and 25 to Sensors 23 and 27 indicates that the flow is highly three dimensional over the aperture.

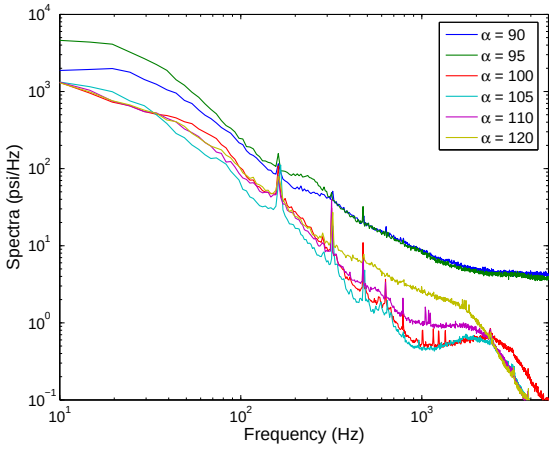

(a) Sensor 23

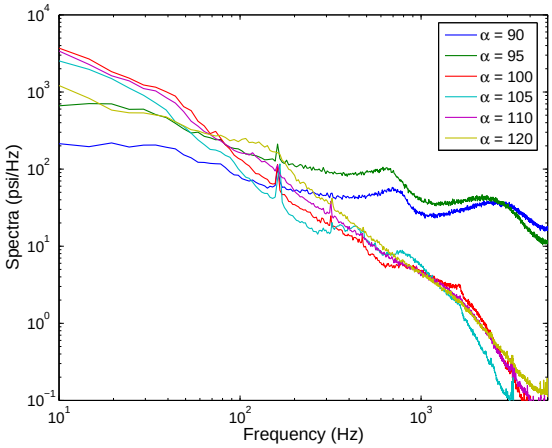

(b) Sensor 21

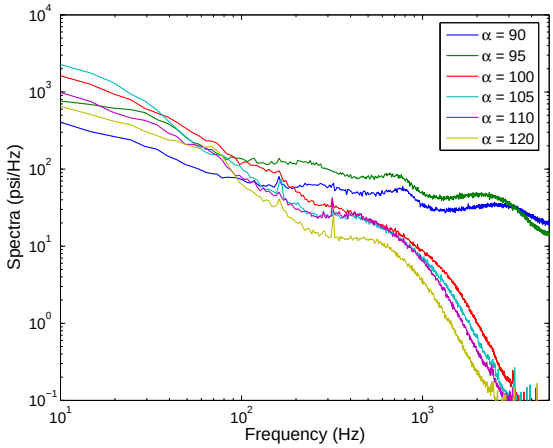

(c) Sensor 25

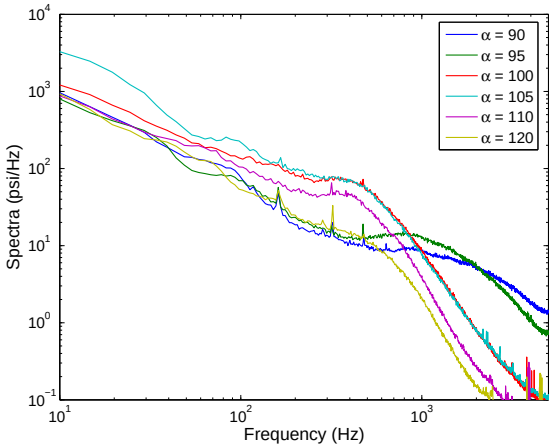

(d) Sensor 27

Figure 5.3: Pressure spectra on the aperture at various elevation angles: 90°, 95°, 100°, 105°, 110°, and 120°. Panels arranged as incoming flow goes from top of the page to bottom.

5.2 Aero-Optic Results with and without Flow Control

Aero-optic measurements obtained using a Malley probe were taken at a fixed elevation angle of $\alpha = 100°$ and an azimuthal angle of $\beta = 0°$. These measurements were taken over the aperture with no suction as well as unsteady suction modulation. Solenoid valves ran at a constant frequency of $25Hz$ provided unsteady suction modulation at multiple duty cycle cases of 50%, 75%, and 100%. Fluctuating, surface pressure at multiple locations was sampled simultaneously with the Malley probe data. The sample locations for the two Malley probe beams are marked as $\times$ and the pressure transducers are numbered and represented as $\circ$ on the turret in Figure 5.1(b). The Malley probe data were sampled at $100,000Hz$ and the surface pressure data were sampled at $10,000Hz$ for 20 seconds.

The power spectral density of $\theta(t)$ of the forward laser probe beam and the fluctuating surface pressure of the Sensor 21 is shown in Figure 5.4 for each of the flow control cases. Shown in Figure 5.4(b), the amplitude of the power spectra density for the frequencies above $1000Hz$ decreases as the duty cycle was increased. Each unsteady suction modulation case witnessed a reduction at the frequencies; the 75% and 100% duty case had similar abatement of the amplitude of the power spectrum density. The surface pressure in the frequencies above $1,000Hz$ showed a decrease in amplitude of the power spectrum density as unsteady suction modulation was applied. Although a reduction in the amplitude of the pressure power spectrum density was seen for each suction control case, no noticeable difference was seen between the control cases. Both Figure 5.4(b) and 5.4(c) show peaks at $200Hz$ and $300Hz$. This agreement indicates that both the Malley probe and surface pressure measurements observed the same structures within the flow.

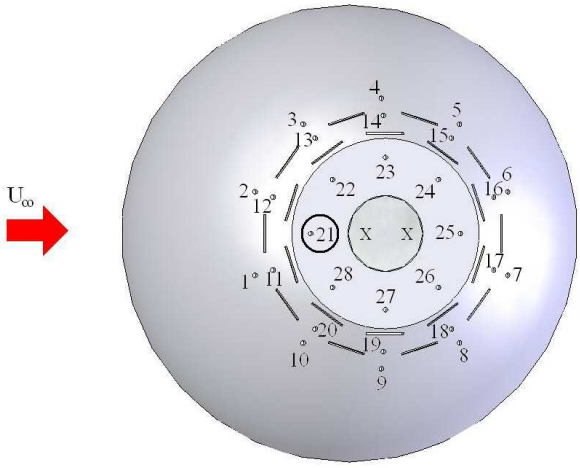

(a) Sensor Location

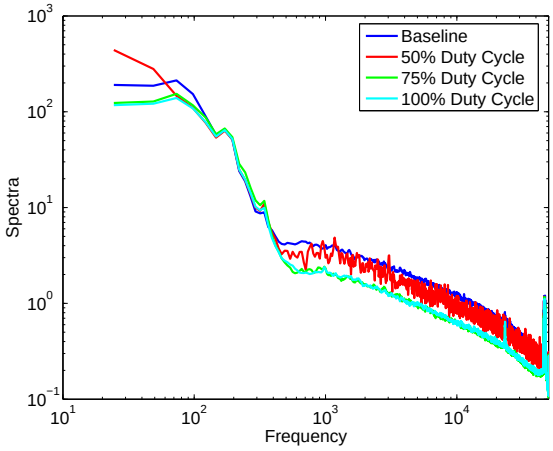

(b) Malley probe

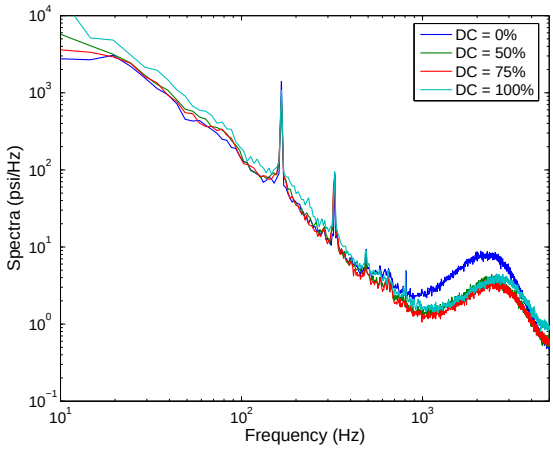

(c) Sensor 21

Figure 5.4: Power Spectrum Density of θ and surface pressure on the aperture at 100° and various duty cycles: 0%, 50%, 75%, and 100%.

To obtain the OPD_{rms}, the abberation wavefront angle $\theta(t)$ is Fourier transformed and Equation 2.8 is rewritten as Equation 5.2,

$$OPD_{rms}^2 = U_C^2 \int_0^t \frac{\langle \hat{\theta}(f)\hat{\theta}^*(f) \rangle}{(2\pi f_{sample})^2} df \tag{5.2}$$

where f_{sample} is the sample frequency, U_C is the convective velocity of the wavefront abberations, $\hat{}$ is the Fourier operator, and $*$ represents the complex conjugate. The analysis is limited to the frequencies associated with the aero-optic effects; therefore the analysis examined frequencies above $1000Hz$. The convection velocity is calculated using a spectral cross-correlation function to find the maximum time delay between the two laser probe beams with the assumption of the Taylor's Hypothesis also known as frozen-turbulence approximation. Taylor's Hypothesis according to Panton [56] states that the characteristics of the structures that convect downstream past a given location remains constant or "frozen". Using the Taylor's Hypothesis the convection of the aberration wavefront angle $\theta(t)$ can be expressed as Equation 5.3,

$$\theta_2(t) = \theta_1(t - \tau_{max}) \tag{5.3}$$

and Fourier transformed into frequency space in Equation 5.4

$$\hat{\theta}_2(\omega) = \hat{\theta}_1(\omega) \exp(-i\omega\tau_{max}) \tag{5.4}$$

where τ_{max} is the maximum time delay and $\hat{}$ is the Fourier operator. The spectral cross-correlation function is defined in Equation 5.5,

$$S(\omega) = \frac{1}{T}\langle \hat{\theta}_1(\omega), [\hat{\theta}_1(\omega) \exp(-i\omega\tau_{max})]^* \rangle \tag{5.5}$$

where T is the time period, θ_1 is the aberrated wavefront angle of the front laser probe beam, $\hat{}$ is the Fourier operator, and * is the complex conjugate. The τ_{max} is solved for by taking the slope of spectral cross-correlation function, as seen in Equation 5.6

$$\tau(f) = \frac{1}{2\pi}\frac{d}{df}\arg[S(f)] \tag{5.6}$$

The τ_{max} associated with the convecting aberration wavefront was determined to be $\tau = 0.371ms$. Knowing τ, the separation distance between the laser probe beams ($\Delta = 4.0cm$), and using Equation 5.7, the convection velocity was found to be $0.83U_\infty$ or 85.49 m/s. A convection velocity range of about $0.80U_\infty$ to $0.85U_\infty$ was found by Gordeyev et al. [34] to contain the majority of the optical distortions.

$$U_C = \frac{\Delta}{\tau_{max}(f)} \tag{5.7}$$

Now that U_C is know the OPD_{rms} can be determined using Equation 5.2. Figure 5.2 shows the OPD_{rms} at the no control case and the unsteady suction modulation cases. At an elevation angle of $\alpha = 100°$, the 50% duty cycle modulation case saw a 34% decrease in the OPD_{rms} as compared to the baseline. Increasing the unsteady suction modulation to 75% duty cycle saw an even greater drop 86% in the OPD_{rms} over the aperture. Although there is a slight increase in the OPD_{rms} the amount of reduction of the OPD_{rms} is significantly lower. The increase in the OPD_{rms} might be due to the change from unsteady suction to steady suction.

Recorded simultaneously with the Malley probe data were fluctuating surface pressure on and around the aperture. For the baseline and each open loop control cases, the spatial fluctuating surface pressure rms ($\langle p_{rms}\rangle$) was calculated for the pressure signals on the aperture and is shown in Figure 5.1(b). The surface $\langle p_{rms}\rangle$ increased as

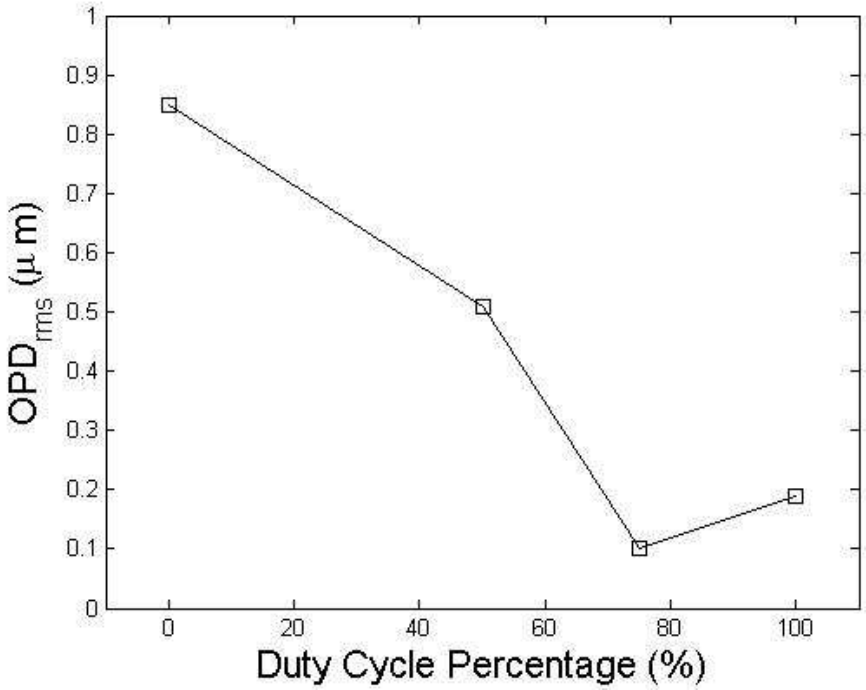

Figure 5.5: Spatial surface pressure rms on the aperture.

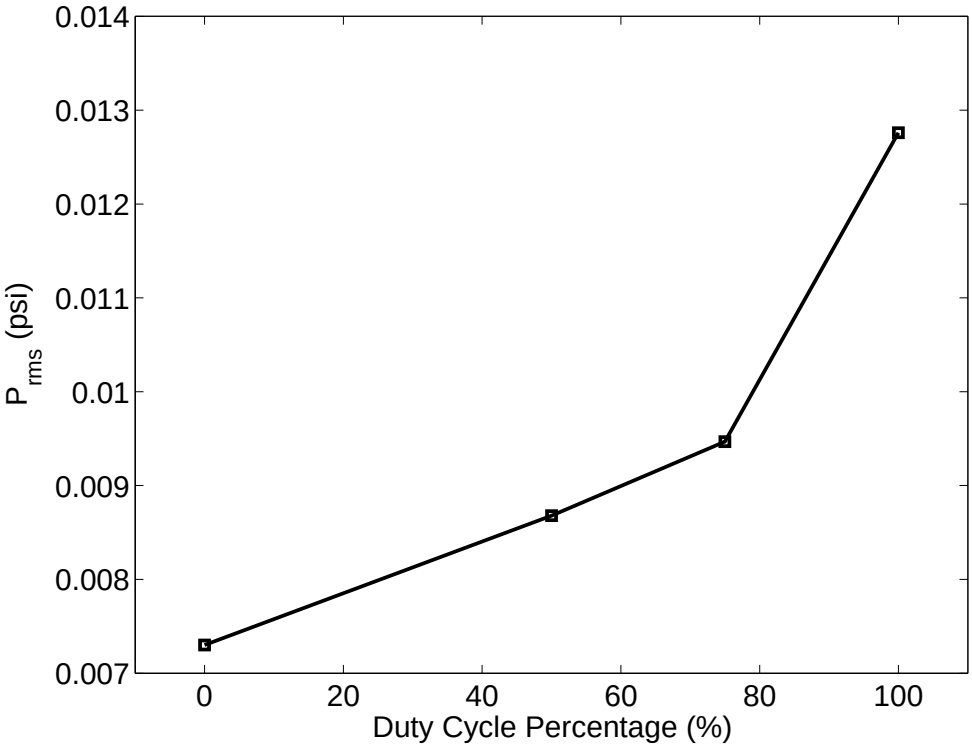

Figure 5.6: Spatial surface pressure rms on the aperture.

the amount of suction was increased. At 100% duty cycle the $\langle p_{rms} \rangle$ is significantly greater than the 75% duty cycle, unsteady suction modulation case. Thus, the $\langle p_{rms} \rangle$ trend is nonlinear and indicates that the steady suction case drastically increases the surface pressure fluctuations.

A relationship between the OPD_{rms} and the p_{rms} can be seen in the comparison of Figure 5.5 and Figure 5.6. The OPD_{rms} is inversely proportional to the p_{rms}.

The simultaneous sampling of aero-optic and surface pressure data allow for the development of a relationship between the two. Thus, pressure measurements can be used as a practical control signal for a closed loop controller.

Chapter 6

Conclusions and Future Work

6.1 Summary and Conclusions

The first part of this work, performed in the Syracuse University wind tunnel at a Mach number of about 0.1 and a Reynolds number of 500,000, looked at the effects of both a static and dynamic pitching hemisphere with and without suction flow control to reduce turbulence levels. At a static pitch angle of $\alpha = 120^\circ$ it was seen that the actuation forward of the aperture was significantly more effective at reducing the size of the wake than the aft actuation alone. Before the hemisphere portion was dynamically pitched, a series of static pitch tests were performed to determine the dynamic pitch range and the performance of the actuation system. It was determined from these tests that the flow state over the aperture reached its incipient angle at $\alpha = 115^\circ$ and was massively separated at higher elevation angles. At each of these angles, when unsteady suction modulation actuation was applied, the flow saw a reduction in separation levels over the aperture.

When the hemisphere was dynamically pitched it was found that motion of the hemisphere was the dominant frequency, thus causing a change of flow state from attached to separated back to attached. Even at a low rotation rate a strong hysteresis developed and caused the separation elevation angle as the turret pitched back to be

different than the reattachment angle as the turret pitch forwards. This trend is similar to dynamic stall over an airfoil. Since the turret produced no lift the turret only exhibits some characteristics of dynamic stall. Another interesting trend emerged while the turret was dynamically pitching. When the elevation angle increased so did the amplitude of the fluctuating surface pressure signal in the sensors forward of the aperture, and when the elevation angle decreased the fluctuating surface pressure amplitude decreased. However, the sensors on the aperture and behind exhibited the opposite trend, the fluctuating surface pressure amplitude sharply dropped when the flow separated and increased when reattached.

For the dynamically pitching turret a very simple proportional controller was constructed by feeding back the fluctuating surface pressure signal from a single pressure sensor forward of the aperture. Observed in the baseline dynamic pitching case, the sensor utilized in the controller exhibited a high correlation between the amplitude of fluctuating surface pressure signal and the elevation angle. Although the closed loop flow control reduced the fluctuating velocity, the controller was not robust. It was highly dependent on a single observer which could fail or give false results, for many reasons such as misalignment with the flow. Thus, a more robust controller would incorporate multiple observers to ensure a true feedback signal at multiple flow conditions.

In the next part of the work, the hemisphere was fixed in the pitch direction and dynamically rotated in the azimuthal direction. Due to the motion of the turret the flow became asymmetric over the hemisphere. In an effort to maximize the efficiency of a closed loop control system, the actuation system was divided into two zones along the centerline of the hemisphere to account for the asymmetric flow over the turret. Multiple signals were fed into a measurement estimator based, simple proportional controller to drive multiple output signals. The closed loop flow control system was

able to significantly reduce the fluctuating velocity, as compared to both baseline and steady suction. Implementing the closed loop control required less suction, which translates to less energy required to improve the flow. Less energy requirements also correspond to smaller equipment size needed to generate that energy. A cleverly designed closed loop control would save both energy and equipment weight.

Performed at the Air Force Research Laborites facility at Wright Patterson Air Force Base, the final part of the study took aero-optic and fluctuating surface pressure measurements over a fully separated, static turret in a high Reynolds number flow. The aero-optic measurements showed a decrease in the OPD_{rms} as the amount of suction was increased. Another important result from this test found a relationship between the OPD_{rms} and spatially averaged surface pressure rms to be inversely proportional to each other. As the suction was increased, the surface $\langle p_{rms} \rangle$ increased while the OPD_{rms} decreased. The fluctuating surface pressure can be used as a control observer for feedback closed loop flow control.

6.2 Future Work

Further analysis and future experimental studies that would give a more enriched view of the flow and its corresponding effects on the aero-optics are provided below:

- Performing a low dimensional, balanced truncation upon both the pressure and velocity measurements using the Split POD developed by Camphouse et al. [13] will provide deeper insight into flow. This analysis would help determine the energy components within the flow due to both the hemisphere articulation and suction actuation. It would also help determine which pressure sensors would be optimum observers by detecting the level of actuation energy within the pressure signal at each location.

- Examination of multiple planes across the turret would broaden the understanding of the highly complex, three dimensional flow that occurs over the turret. Structures not seen at the centerline of the turret would be observed, thus providing a deeper knowledge of the flow.

- Development and incorporation of a Multiple Output Multiple Input closed loop controller in the dynamically pitching turret case may improve the efficiency of the actuation system. The actuation system could be run more efficiently by not running in the suction in unison and employing a MIMO system.

- Development of a reduced order model for control purposes would possibly improve the ability for the controller to track the state of the flow for the dynamically yawing turret as was observed when included in the dynamically pitching case.

- Perform an experimental investigation of the aero optics of a dynamically pitching and yawing turret with and without flow control. This experiment would show directly what effect the rotating hemisphere and actuation have on the aero optics over the aperture.

- Development of a control system which utilizes both adaptive optics and active flow control would possible improve the overall performance of the system. The active flow control would provide a stable, predictable flow over the aperture which the adaptive optic system could morph the laser lens to.

Bibliography

[1] R. Adrian, "On the role of conditional averages in turbulence theory," *Turbulence in Liquids: Proceedings of the 4th Biennial Symposium on Turbulence in Liquids*, pp. 323-332, 1977.

[2] M. Alrefai and M. Acharya, "Controlled Leading-Edge Suction for Management of Unsteady Separation over Pitching Airfoils," *AIAA Journal*, Vol. 34, No. 11, Nov. 1996.

[3] J. Anderson Jr., *Fundamentals of Aerodynhamics*, 3rd Edition, McGraw-Hill, New York, NY, 2002.

[4] M. Andino, J. Pinier, R. Schmit, R. Camphouse, J. Myatt, and M. Glauser, "Flow control over a cylindrical turret using synthetic jets," *46th AIAA Aerospace Sciences Meeting and Exhibit*, AIAA 2008-736, Reno, NV 2008.

[5] M. Andino, R. Wallace, M. Glauser, R. Camphouse, R. Schmit, and J. Myatt, "Boundary feedback flow control: Proportional control with potential application to aero-optics," *AIAA Journal*, Vol. 49, No. 1, 2010.

[6] M. Andino, *Flow control effects on the turbulent flow physics of a three dimensional turret*, Doctoral dissertation, Syracuse University, 2009.

[7] G. Arwatz, I. Fono, and A. Seifert, "Suction and Oscillatory Blowing Actuator Modeling and Validation," *AIAA Journal*, Vol. 46, No.5, pp.1107-1117, 2008.

[8] J. Ausseur, *Application of Low-Dimensional Techniques for Closed-Loop Control of Turbulent Flows*, Doctoral dissertation, Syracuse University, 2007.

[9] G. Batchelor, *An Introduction to Fluid Dynamics*, Cambridge University Press, London, 1967.

[10] G. Berkooz, P. Holmes, and J. Lumley, "The Proper Orthogonal Decomposition in the Analysis of Turbulent Flows," *Annunal Review of Fluid Mechanics*, Vol. 25, pp. 539-575, 1993.

[11] R. Biedron and C. Rumsey, *CFL3D Version 5.0 User's Manual*, NASA Langley Research Center, Aerodynamic and Acoustic Methods Branch, Hampton, VA.

[12] J. Bonnet, D. Cole, J. Delville, M. Glauser, and L. Ukeiley, "Stochastic estimation and proper orthogonal decomposition: Complementary techniques for identifying structure," *Experiments in Fluids*, Vol. 17, pp. 307-314, 1994

[13] R. Camphouse, M. Andino, R. Wallace, M. Glauser, R. Schmit, and J. Myatt, "Boundary feedback flow control: Baseline and actuation mode expansions with application to reducedorder modeling, simulation and aero-optics", AIAA Journal (under review).

[14] H. Carlson and R. Miller, "Reduced-order Modeling and Sensing of Flow Separation on Lifting Surfaces," *40th AIAA Aerospace Sciences Meeting & Exhibit*, AIAA Paper 2002-0975, Reno, NV, January, 2002.

[15] L. Carr, K. McAlister, and W. McCroskey, "Analysis of the the develop of dynamic stall based on oscillating airfoil experiments," NASA Technical Note, NASA TN D-8382, Jan. 1977.

[16] L. Cattafesta and M. Sheplak, "Actuators for Active Flow Control," *Annual Review of Fluid Mechanics*, vol. 43, pp. 247-273, 2011.

[17] D. Cole and M. Glauser, "Applications of stochastic estimation in the axisymmetric sudden expansion," *Physics of Fluids*, Vol. 10, No. 11, pp. 2941-2949, 1998.

[18] J. Craig, "A Study in Flow Control and Screening Methods for Aircraft Laser Turrets," *Air Force Report*, Air Force Weapons Laboratory, ARWL-TR-80-119, 1981.

[19] J. Cress, S. Gordeyev, E. Jumper, T. Ng, A. Cain, "Similarities and differences in aero-optical structure over cylindrical and hemishpherical turrets with a flat window," *45th Aerospace3 Science Meeting and Exhibit*, AIAA 2007-326, Reno, NV, Jan. 2007.

[20] J. Cress, *Optical Aberrations caused by Coherent Structures in a Subsonic, Compressible, Turbulent Boundary Layer*, Doctoral dissertation, Norte Dame, 2010

[21] L. Ericsson and J. Reding, "Unsteady Airfoil Stall Review and Extension," *Journal of Aircraft*, Vol 8, pp. 609-616, Aug. 1971.

[22] L. Ericsson and J. Reding, "Unsteady Flow Concepts for Dynamic Stall Analysis," *Journal of Aircraft*, Vol 21, No. 8, pp.601-606, Aug 1984.

[23] E. Firzgerald and E. Jumper, "The optical distortion mechanism in a nearly incompressible free shear layer," *Journal of Fluid Mechanics*, 512, pp. 153-189, 2004.

[24] M. Gad-el Hak, "Modern developments in flow control," *Applied Mechanics Reviews*, Vol. 49, No. 7, pp. 365-380, 1996.

[25] N. Gregory, "Research on suction surfaces for laminar flow," *Boundary Layer and Flow Control*, Vol. 2, pp.924-960, 1961

[26] K. G. Gilbert, L. J. Otten, editors. *Aero-optical Phenomena*, Progress in astronautics and aeronautics series, vol. 80. New York: American Institute of Aeronautics and Astronautics, 1982.

[27] J. Gladstone and T. Dale, "Researches on the refraction, dispersion, and sensitiveness of liquids," Philosophical Transactions of the Royal Society of London, vol. 153, pp. 317-343, 1863

[28] M. Glauser, H. Higuchi, J. Ausseur, J. Pinier, and H. Carlson, "Feedback Control of Separated Flows (Invited)," *2nd AIAA Flow Control Conference*, AIAA 2004-2521, Portland, OR, 2004.

[29] M. Glauser, S. Leib, and W. George, "Coherent structures in the axisymmetric mixing layer," *Turbulent Shear Flows 5*, Springer-Verlag, pp. 4.21-4.26, 1987.

[30] M. Glauser and W. George, "Orthogonal decomposition of the axisymmetric jet mixing layer including azimuthal dependence," *Advances in Turbulnce*, eds. G. Comte-Bellot and J. Mathieu, Springer, New York, 1987, 357-366.

[31] S. Gordeyev, T. E. Hayden, and E. J. Jumper, "Aero-Optical and Flow Measurements Over a Flat-Windowed Turret," *AIAA Journal*, Vol. 45, No. 2, 2007, pp. 347-357.

[32] S. Gordeyev and E. J. Jumper, "Fluid dynamics and aero-optics of turrets," *Progress in Aerospace Sciences*, vol 46, pp 388-400, July 2010.

[33] S. Gordeyev, E. Jumper, B. Vukasinovic, A. Glezer, and V. Kibens, "Hybrid Flow Control of a Turret Wake, Part II: Aero-Optical Effects," AIAA Paper 2010-438, *48th AIAA Aerospace Sciences Meeting*, Orlando, FL, 2010

[34] S. Gordeyev, D. Duffin, and E. Jumper, "Aero-Optical Measurements Using Malley Probe and High-Bandwidth 2-D Wavefront Sensors," *International Conference on Advanced Otical Diagnostics in Fluids, Solids, and Combustion*, Tokyo, Japan, Dec. 2004

[35] J. Hinze, *Turbulence*, McGraw-Hill, New York, 1959.

[36] P. Holmes, J. Lumley, and G. Berkooz, " *Turbulence, Coherent Structures, Dynamical Systems, and Symmetry*, Cambridge University Press, New York, NY, 1996.

[37] P. Holmes, J. Lumley, G. Berkooz, J. Mattingly, and R. Wittenberg, "Low Dimensional Models of Coherent Structures in Turbulence," *Physics Reports*, Vol. 287, pp. 337-384, 1997.

[38] R. Hugo and E. Jumper, "Applicability of the aero-optic linking equation to a highly coherent, transitional shear layer," Applied Optics, vol. 39, pp 4392-4401, 2000.

[39] E. Jumper, "Recent advances in the measurement and analysis of dynamic aero-optic interactions (review paper)," *AIAA Journal*, 97-2350, June 1997.

[40] E. Jumper and E. Fizgerald, "Recent advances in aero-optics," *Progress in Aerospace Sciences*, Vol. 37, pp. 299-339, 2001.

[41] E. Jumper and R. Hugo, "Quantification of aero-optical phase distortion using the small-aperture beam technique," *AIAA Journal*, Vol 13, No. 11, pp. 2151-2157, 1995.

[42] H. Klein, M. Malley, O. Sapp, D. Shough, G. Sutton, and J. Yu, "Experimental measurements of the optical path difference of a four-meter dual aerocurtain," *Proceedings of the High Power Laser Optical components Conference*, Boulder, CO, October, 1989.

[43] J. Lumley, "The structure of inhomogeneous turbulence," *Atmospheric Turbulence and Wave Propagation*, Eds. A. Yaglom and V. Tatarski, Moscow: Nauka, 1967, pp. 166-178.

[44] F. Lundell, "Pulse-width modulation blowing/suction as a flow control actuator," *Experiments in Fluids*, vol. 35, pp. 502-504, 2003.

[45] M. Malley, G. Sutton, and N. Kincheloe, "Beam-jitter measurements of turbulent aero-optical path differences," Applied Optics, 1992, vol. 31, p. 4440-4443

[46] D. Malacara, *Optical shop testing*, Wiley, New York, 1978.

[47] W. McCroskey, L. Carr, and K. McAlister, "Dynamic Stall Experiments on Oscillating Airfoils," *AIAA Journal*, Vol. 14, No. 1, pp. 57-63, 1976.

[48] A. Melling, "Tracer particles and seeding for particle image velocimetry," *Measurement Science and Technology*, Vol. 8, pp. 1406-1416, 1997.

[49] R. Messing and M. Kloker, "Investion of suction for laminar flow control of three-dimensional boundary layers," *Journal of Fluid Mechanics*, vol. 658, pp.117-147, 2010.

[50] P. E. Morgan and M. R. Visbal, "Numerical Simulations Investigating Contol of Flow Over a Turret," AIAA Paper 2009-574, *47th AIAA Aerospace Sciences Meeting*, Orlando, FL, 2009

[51] P. E. Morgan and M. R. Visbal, "Hybrid RANS/LES Simulations for Flow Around Two Turret Configurations," AIAA Paper 2007-550, *46th AIAA Aerospace Sciences Meeting and Exhibit*, January 7-10, 2007, Reno, Nevada.

[52] B. Munson, D. Young, and T. Okiishi, *Fundamentals of Fluid Mechanics*, 4th Ed., John Wiley & Sons, Inc., 2002

[53] D. Neal, T. O'Hern, J. Torczynski, M. Warren, R. Shul, and T. McKechnie, "Wavefront sensors for optical diagnostics in fluid mechanics: Application to heated flow, turbulence and droplet evaporation," *Optical diagnostics in fluid and thermal flow*, Eds S. Cha and J. Trollinger, vol. 2005, pp 194-203, 1993.

[54] A. Nightinggale, B. Mitchell, B. Goodwine, and E. Jumper, "Feedforward Adaptive-Optic Mitigation of Aero-Optic Disturbances," AIAA Paper 2008-4211, *39th AIAA Plasmadynamics and Lasers Conference*, Seattle, WA, 2008.

[55] B. Noack and H. Eckelmann, "A low-dimensional Galerkin method for the three-dimensional flow around a circular cylinder," *Physics of Fluids*, Vol. 6, pp. 124-143, 1994.

[56] R. Panton, *Incompressible Flow*, 2nd Edition, John Wiley & Sons, Inc., New York, NY, 1996.

[57] A. Perry, *Hot wire anemometry*, Oxford University Press, Oxford, 1982.

[58] J. T. Pinier, J. M. Ausseur, M. N. Glauser, and H. Higuchi, "Proportional Closed-Loop Feedback Control of Flow Separation," *AIAA Journal*, **45**, No. 1, 2007, pp. 181-190.

[59] S. Purohit, J. Shang, and W. Hankey Jr., "Effect of Suction on the Wake Structure of an Three-Dimensional Turret," *AIAA 16th Fluid And Plasma Dynamics Conference*, AIAA-83-1738, Danvers, MA, July, 1983

[60] M. Raffel, C. Willert, S. Wereley, and J. Kompenhans, *Particle Image Velocimetry, A Practical Guide*, Second Edition, Springer, Berlin, 2007.

[61] B. Recktenwald, M. Khan, A. Ahmed, "Influence of Aspect Ratio on End Wall Flows of Surface Mounted Obstacles," *47th AIAA Aerospace Sciences Meeting including The New Horizons Forum and Aerospace Exposition*, AIAA 2009-544, Orlando, Florida, Jan. 5-8, 2009

[62] J. Reid, K. Lynch, B. Thurow, "Further Development of a High-Speed 3-D Density Measurement Technique for Aero-Optics," *40th Fluid Dynamics Conference and Exhibit*, AIAA 2010-4844, Chicago, IL, 2010.

[63] W. Rose, "Measurements of aerodynamic parameters affecting optical poerformance," Final Report AFWL-TR-78-191, Air Force Weapons Laboratory, 1979.

[64] Schlichting and W. Pechau, "Auftriebserhöhung von Tragflüdgeln durch kontinuierlich verteilte Absaugung," *Zeitschrift für Flugwissenschafter*, vol. 7, pp. 113-119, 1959.

[65] S. Siegel, K. Cohen, and T. McLaughlin, "Numerical Simulations of a Feedback-Controlled Circular Cylinder Wake," *AIAA Journal* Vol. 44, No. 6, pp. 1266-1276, 2006.

[66] L. Sirovich, "Turbulence and the dynamics of coherent structures. Parts 1,2, & 3," *Quarterly of Applied Mathematics*, XLV(3), 561-590, 1987.

[67] R. Slunder, L. Gris, and J.Katz, "Optical Turret Aerodynamics – a Preliminary Study," *46th Aerospace Sciences Meeting and Exhibit*, AIAA 2008-429, Reno, NV, Jan. 2008.

[68] A. Smits and J -P. Dussauge, *Turbulent Shear Layers in Supersonic Flow*, 2nd Edition, Springer 2006.

[69] P. Spalart, W. Jou, M. Strelets and S. Allmaras, "Comments on the feasibility of LES for wings and on a hybrid RANS/LES approach," *1st AFOSR International Conference on DNS/LES*, Advances in DNS/LES, C. Liu and Z. Liu Eds., Greyden Press, Columbus, OH, 1997.

[70]

[71] P. Spalart and S. Allmaras, " A one equation turbulence model for aerodynamic flows", *La Recherche Aerospatiale*, Vol. 1, pp.5-21 1994.

[72] K. Squires, "Detached-Eddy Simulation: Current Status and Perspectives," R. Friedrich, B. J. Gurts, O. Metaism, (Eds.), *Direct and Large Eddy Simulation*, Kluwer, Dordrecht, pp.465-480, 2004 .

[73] S. Tavoularis, *Measurement in Fluid Mechanics*, Cambridge university Press, Cambridge, 2005

[74] J. Taylor and M. Glauser, "Towards practical flow sensing and control via POD and LSE based low-dimensional tools," *Journal of Fluids Engineering*, Vol 126, No. 3, pp. 337-345, 2004.

[75] H. Tennekes and J. Lumley, *A First Course in Turbulence*, The MIT Press, Cambridge, MA., 1972.

[76] J. Trolinger, "Aero-optical characterization of aircraft optical turrets by holography, interferometry and shadowgraph," *NASA Ames Research Center Proceedings of the Aero-Optics Symposium on Electromagnetic Wave Propagation from Aircraft*, p. 127-151, 1980.

[77] T. Tung and R. Adrian, "Higher-order estimates of conditional eddies in isotropic turbulence," *Physics Fluids*, Vol. 23, no. 7, pp. 1469-1470, 1980.

[78] R. Tyson, *Principles of Adaptive Optics*, 2nd Ed., Academic Press, Chestnut Hill Massachusetts, 1991.

[79] L. Ukeiley, L. Cordier, R. Manceau, J. Delville, M. Glauser, and J-P. Bonnet, "Examination of the large-scale structures in a turbulent plane mixing layer. Part 2. Dynamical systems model," *Journal of Fluid Mechanics*, Vol. 441, pp. 67-108, 2001.

[80] V. Thirunavukkarasu, H. Carlson, R. Wallace, P. Shea, and M. Glauser, "Measurement and Dynamical Model-Based Feedback Flow Control Development and Simulation for a Pitching Turret. Part 1," *AIAA Journal*, under review

[81] B. Vukasinovic, and A. Glezer, "Control of a Separating Flow over a Turret," *37th AIAA Fluid Dynamics Conference*, AIAA Paper 2007-4506, Miami, Florida, 2007.

[82] B. Vukasinovic, A. Glezer, S. Gordeyev, E. Jumper, and V. Kibens, "Hybrid Flow Control of a Turret Wake, Part I: Aerodynamic Effects," AIAA Paper 2010-86, *48th AIAA Aerospace Sciences Meeting*, Orlando, FL, 2010

[83] R. Wallace, M. Andino, M. Glauser, R. C. Camphouse, R. Schmit, and J. Myatt, "Flow and Aero-Optics Around a Turret Part II: Surface Pressure Based Proportional Closed Loop Flow Control," AIAA Paper 2008-4217, *4th Flow Control Conference*, Seattle, WA, 2008.

[84] R. Wallace, P. Shea, M. Glauser, V. Thirunavukkarasu, and H. Carlson, "CFD-Guided, Measurement and Dynamical Model-Based Feedback Flow Control for a Pitching Turret," *AIAA Journal*, under review

[85] R. Wallace, P. Shea, M. Glauser, V. Thirunavukkarasu, and H. Carlson, "Feedback Flow Control for a Three-Dimensional Turret (Part II)" AIAA Paper 2010-361, 39th AIAA Fluid Dynamics Conference, Orlando, USA, 2010.

[86] R. Wallace, P. Shea, M. Glauser, V. Thirunavukkarasu, and H. Carlson, "Closed-loop Flow Control for an Articulating Turret with Two Degrees of Freedom: Pitch and Yaw" AIAA Paper 2010-4966, 5th AIAA Flow Control Conference, Chicago, Il, USA, 2010.

[87] W. Welford, *Optics*, Third Edition, Oxford University Press, Oxford, 1988

[88] R. Woszidlo, L. Taubert, and I. Wygnanski, "Manipulating the Flow over Spherical Protuberances in a Turbulent Boundary Layer," *AIAA Journal*, Vol. 47, No. 2, pp.437-450, 2009.

Appendix I

Sensor No.	Serial No.	Volts/PSI	Volts/kPa	Output Bias Level
1	3845	1.611	233.6	4.8
2	4485	1.532	222.2	11.5
3	3848	1.423	206.3	4.9
4	4495	1.437	208.4	11.5
5	4510	1.467	212.8	11.5
6	4486	1.652	196	11.4
7	3840	1.463	212.1	5
8	4481	0	0	0
9	4476	1.597	231.6	11.5
10	4469	1.482	215.0	11.4
11	3842	1.487	215.7	4.9
12	4502	1.484	215.3	11.6
13	4482	1.466	212.6	11.4
14	3835	1.506	218.5	5.1
15	4472	1.468	213.0	11.1
16	4477	1.36	197.2	11.6
17	4468	1.48	214.7	11.5
18	4500	1.424	206.5	11.5
19	4512	1.492	216.4	11.5
20	3833	1.477	214.2	5.2
21	3846	1.542	223.6	4.7
22	3843	1.602	232.4	4.9
23	4509	1.385	200.9	11.5
24	4491	1.664	218.2	11.5
25	4473	1.505	218.2	11.5
26	4513	1.413	204.9	11.6
27	4508	1.429	207.2	11.5
28	3837	1.506	218.4	4.7
29	4506	1.386	201.0	11.4
30	4503	1.413	205.0	11.5
31	3847	1.552	255.1	4.9

Table 6.1: SU pressure sensitivity.

Sensor No.	Serial No.	Volts/PSI	Volts/kPa
1	5100	1.499	217.4049167
2	5101	1.584	229.7327472
3	5103	1.433	207.8327189
4	5104	1.54	223.351282
5	5262	1.459	211.6035847
6	5263	1.452	210.5883516
7	5264	1.449	210.1532517
8	5266	1.500	217.54995
9	5267	1.475	213.9241175
10	5268	1.427	206.9625191
11	5269	1.422	206.2373526
12	5270	1.479	214.5042507
13	5271	1.500	217.54995
14	5272	1.56	226.251948
15	5273	1.501	217.6949833
16	5275	1.452	210.5883516
17	5276	1.488	215.8095504
18	5277	1.55	224.801615
19	5278	1.476	214.0691508
20	5279	1.463	212.1837179
21	5280	1.448	210.0082184
22	5281	1.501	217.6949833
23	5282	1.583	229.5877139
24	5043	1.492	216.3896836
25	5044	1.377	199.7108541
26	5283	1.546	224.2214818
27	5284	1.511	219.1453163
28	5285	1.565	226.9771145

Table 6.2: SARL pressure sensitivity.